Small Angle Neutron Scattering Studies of the Flux Line Lattices in the Borocarbide Superconductors

Eskildsen, Morten Ring

Publication date:
1998

Document Version
Publisher's PDF, also known as Version of record

Risø–R–1084(EN)

Small Angle Neutron Scattering Studies of the Flux Line Lattices in the Borocarbide Superconductors

Morten Ring Eskildsen

Risø National Laboratory, Roskilde, Denmark
December 1998

Abstract This thesis describes small angle neutron scattering studies of the flux line lattice (FLL) in the borocarbide superconductors with stoichiometry $R\mathrm{Ni_2B_2C}$, where R is one of Y, Dy, Ho, Er, Tm and Lu. The "pure" compounds $\mathrm{YNi_2B_2C}$, $\mathrm{ErNi_2B_2C}$, $\mathrm{TmNi_2B_2C}$ and $\mathrm{LuNi_2B_2C}$, as well as $\mathrm{Y_{0.75}Lu_{0.25}Ni_2B_2C}$ and Co doped $\mathrm{Lu(Ni_{1-x}Co_x)_2B_2C}$ with $x = 1.5 - 9\%$ was studied. Of the materials studied $\mathrm{ErNi_2B_2C}$ and $\mathrm{TmNi_2B_2C}$ orders magnetically, the coexistence of superconductivity and magnetism being one of the main motivations for these studies. Three main conclusions can be derived from the experiments reported in this thesis.

1. Existence of a low field hexagonal to square symmetry transition of the FLL, ubiquitous to the superconducting borocarbides, magnetic and non-magnetic alike. This symmetry transition is due to a four-fold anisotropy of the Fermi surface in the borocarbides. The superconducting screening currents around each flux line are distorted away from the circular flow pattern of an isotropic system, and towards a square. The square flow patterns manifest themselves by inducing a transition to a square FLL as the field is increased, with a transition onset field determined by the range of the non-local electrodynamics.

2. A static disordering of the FLL in $\mathrm{YNi_2B_2C}$ and $\mathrm{LuNi_2B_2C}$. In these materials one observes a well ordered FLL, with a longitudinal correlation length exceeding 100 flux line spacings. As the applied field is increased the longitudinal correlation length, or equivalent, the "straightness" of the flux lines, increases with field up to $H/H_{c2} \sim 0.2$. Above this field the FLL correlation length slowly starts to fall off, in contradiction to a theoretical model, which predicts a monotonically increasing correlation length up to the onset of the peak effect. The origin of the crossover to a less ordered FLL is not resolved, but it is speculated that this is driven by the shear properties of the FLL.

3. The existence of complex interactions between the magnetic state and the FLL in $\mathrm{TmNi_2B_2C}$. The FLL in this material undergoes two symmetry transitions in addition to the low field hexagonal to square transition present in all the borocarbides, and described above. As the applied field is raised the square FLL first undergoes a rhombic distortion and then a discontinuous transition into a hexagonal symmetry. The FLL symmetry transitions are closely linked to changes in the magnetic structure. In zero field the magnetic structure is a transverse modulated spin density wave. As the field is increased the magnetic structure is modified, signalled by the appearence of additional neutron scattering reflections. In addition, the FLL reflectivity shows distinct peaks as the thulium ions orders magnetically at T_{N} and across the field driven magnetic transition. Furthermore the field induced magnetic structure is dependent on the field- and temperature history in the superconducting phase, giving rise to hysteresis. No explanation for this behaviour exists at the present.

This thesis was submitted in partial fulfilment of the requirements to obtain a Ph. D. in physics at the University of Copenhagen. The work presented here were carried out at the Condensed Matter Physics and Chemistry Department at Risø National Laboratory, Denmark. My supervisors on the project was Niels Hessel Andersen from Risø and Per Hedegaard from the University of Copenhagen.

This final edition of the thesis contains minor changes and additions, made after the thesis defense which took place on September 2, 1998.

ISBN 87–550–2472–6; 87-550-2473-4(internet)
ISSN 0106–2840

Information Service Department · Risø · 1998

Many of the results presented in this thesis are also included in a number of articles. It should be noted that these publications are a result of somtimes large collaborations, and therefore contain additional results besides my own. In the main text I have included these supplementary results where they are essential. I have made an effort to clearly identify results for which I am not responsible. In general I did the small angle neutron scattering and the detailed analysis reported in chapters 4 - 7. The publications are the following (in cronological order):

M. R. Eskildsen, P. L. Gammel, B. P. Barber, U. Yaron, A. P. Ramirez, D. A. Huse, D. J. Bishop, C. A. Bolle, C. M. Lieber, S. Oxx, S. Sridar, N. H. Andersen, K. Mortensen & P. C. Canfield. Observation of a Field-Driven Structural Phase Transition in the Flux Line Lattice in $ErNi_2B_2C$. *Phys. Rev. Lett.* **78**, 1968-1971 (1997).

M. R. Eskildsen, P. L. Gammel, B. P. Barber, A. P. Ramirez, D. J. Bishop, N. H. Andersen, K. Mortensen, C. A. Bolle, C. M. Lieber & P. C. Canfield. Structural Stability of the Square Flux Line Lattice in YNi_2B_2C and $LuNi_2B_2C$ Studied with Small Angle Neutron Scattering. *Phys. Rev. Lett.* **79**, 487-490 (1997).

M. R. Eskildsen, K. Harada, P. L. Gammel, A. B. Abrahamsen, N. H. Andersen, G. Ernst, A. P. Ramirez, D. J. Bishop, K. Mortensen, D. G. Naugle, K. D. D. Rathnayaka & P. C. Canfield. Intertwined symmetry of the magnetic modulation and the flux-line lattice in the superconducting state of $TmNi_2B_2C$. *Nature* **393**, 242-245 (1998).

M. R. Eskildsen, P. L. Gammel, B. P. Barber, A. P. Ramirez, D. J. Bishop, N. H. Andersen, K. Mortensen & P. C. Canfield. Square to hexagonal symmetry transition of the flux line lattice in YNi_2B_2C for different field orientations. *Physica B (ICNS 97 proceedings)* **241-243**, 811-813 (1998).

M. R. Eskildsen, K. Harada, P. L. Gammel, N. H. Andersen, G. Ernst, A. P. Ramirez, D. J. Bishop, K. Mortensen & P. C. Canfield. Hysteresis in the field-induced magnetic structure in $TmNi_2B_2C$. *To appear in Physica B (SCES 98 proceedings).*

P. L. Gammel, D. J. Bishop, M. R. Eskildsen, K. Mortensen, N. H. Andersen, I. R. Fisher, K. O. Cheon, P. C. Canfield & V. G. Kogan. SANS Studies of the Role of Non-Locality on the Flux Line Lattice Square-Hexagonal Symmetry Transition in $Lu(Ni_{1-x}Co_x)_2B_2C$. *Submitted to Phys. Rev. Lett.*

Contents

1 Introduction

The superconducting state is characterized in terms of two lengthscales, the penetration depth, λ, and the coherence length, ξ. The penetration depth describes how far an applied magnetic field will extend into the superconductor, and the coherence length determines the minimum distance over which the density of superconducting electrons can change. The relation between these two lengths, $\kappa = \lambda/\xi$, determines the superconducting response to an external applied field. For $\kappa < 1/\sqrt{2}$ the field is expelled from the bulk of the superconductor, or confined in normal inclusions leading to domain structures of alternating normal and superconducting areas. For $\kappa > 1/\sqrt{2}$ the field is encapsulated in quantized flux lines arranged in a periodic structure, the flux line lattice (FLL).

Ever since I first learned about the magnetic FLL the phenomenon has filled me with fascination. The idea that certain electron flow patterns in the interior of a material, something, which at first thought seem so fragile and abstract, should possess properties closely resembling those of actual massive particles making up solids and liquids, has intrigued me ever since.

This was one of my reasons for choosing to study the FLL for my Ph. D. Moreso I have been so fortunate to get involved with one of the leading groups in the world on this topic, where we also had the luck to strike on a new system which proved to be unexpectedly rich in terms of new and spectacular phenomena.

Studies of the FLL are important for many different reasons. First of all there are still conceptually new phenomena to be observed, as it is well documented by the results presented in this thesis. This makes the understanding of the fundamental properties of the FLL an intellectual challenge. Secondly, the practical use of superconductors depends heavily on the behaviour of the FLL, since this can cause dissipation of energy even in the superconducting state.

The topic of this thesis is the fundamental structural properties of the FLL and the interaction with magnetism in borocarbide superconductors. The thesis is organized in the following manner. This chapter contains an introduction to the superconducting borocarbides and brief overviews of experimental techniques available for FLL imaging and of work done on the FLL in the borocarbides prior to what is reported here. The second chapter contains a short treatment of the Ginzburg-Landau theory for superconductivity, a description of the characteristics of the FLL including distorted lattices, the different flux line phases, and finally an outline of the elastic properties of the FLL and the Larkin-Ovchinnikov theory of collective pinning. Chapter 3 gives a detailed treatment of small angle neutron scattering, especially in relation to the borocarbide FLL. Chapters 4 to 7 contain the experimental results including measurements of the penetration depth and coherence length, FLL symmetry transitions, the FLL longitudinal correlation length and studies of the coupling between superconductivity and magnetism. Finally, chapter 8 summarizes the results, and offer an outlook to future experiments.

1.1 Superconductivity and magnetism

In general, magnetic ordering and superconductivity are mutually exclusive states. When the material favors a ground state with a large moment, superconductivity is usually destroyed, as in $ErRh_4B_4$ [1]. However, if the magnetic ions are well separated from the conduction path, and the magnetic structure is antiferromagneticly modulated yielding a zero net moment on a lengthscale shorter than the superconducting coherence length, coexistence is possible. The interaction between magnetism and superconductivity was historically studied in the rhodium

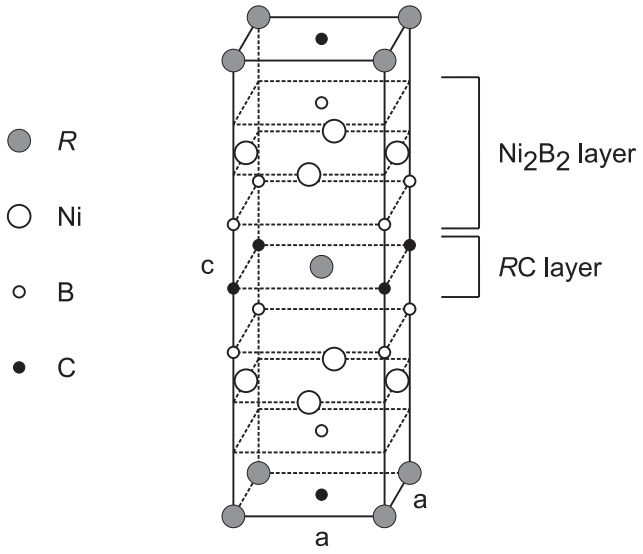

Figure 1. Crystal structure of the borocarbides with stoichiometry RNi_2B_2C. The crystal structure is tetragonal with slightly varying lattice parameters for the different compounds. For $LuNi_2B_2C$ $a = 3.46$ Å and $c = 10.63$ Å [5].

borides [2], but no experiments were ever performed to study the FLL in these compounds.

The borocarbides

The borocarbides are quaternary intermetallics with chemical stoichiometry $R\mathrm{Ni_2B_2C}$, where R = Y, Ce, Pr, Nd, Tb, Dy, Ho, Er, Tm, Yb and Lu. Superconductivity in a number of these materials was first reported in 1994 by R. Nagarajan *et al.* [3] and R. Cava *et al.* [4]. The crystal structure, shown in figure 1, was determined by T. Siegrist *et al.* [5], and is body-centered-tetragonal ($I4/mmm$).

Several of the compounds in the borocarbide series are found to be type-II superconductors with critical temperatures as high as 16 K and κ in the range $6 - 15$, while other orders magnetically and some show coexisting superconductivity and magnetism. It is the coexistence of superconductivity and magnetism that makes the borocarbides especially intersting. In table 1 the superconducting parameters and magnetic transition temperatures are listed for the superconducting borocarbides. One finds a reduction of T_c due to magnetic pairbreaking in the magnetic $\mathrm{DyNi_2B_2C}$, $\mathrm{HoNi_2B_2C}$, $\mathrm{ErNi_2B_2C}$ and $\mathrm{TmNi_2B_2C}$, when compared to the non-magnetic $\mathrm{YNi_2B_2C}$ and $\mathrm{LuNi_2B_2C}$. In the upper critical field one finds different features from compound to compound at the onset of magnetism, making the borocarbides as rich as the rhodium borides. Furthermore the borocarbides are experimentally attractive as the superconductivity exists in a readily accessible field and temperature range, and since large high quality single crystals are available.

The borocarbides are layered materials with alternating $\mathrm{Ni_2B_2}$ and RB-layers, resembling the structure of the high temperature cuprate superconductors. However, the borocarbides are electronically three dimensional, in contrast to the two dimensionality of the cuprates. The rare earth to conduction path separation of the borocarbides falls between that of the rhodium borides and the cuprates, thus yielding an intermediate range of interaction between superconductivity and magnetism. A moderately high density of states at the Fermi level indicates that the borocarbides can be classified as conventional superconductors.

I present results obtained from experiments on the FLL in the "pure com-

	R	T_c (K)	λ (Å)	ξ (Å)	κ	$T_N(H=0)$ (K)
$\star$	Y	15.6	710-1500	60-100	12-15	-
	Dy	6.4	-	220	-	10.6
	Ho	8.0	-	-	-	8.5
$\star$	Er	10.5	1160	131	8.8	6.8
$\star$	Tm	11.0	780	124	6.3	1.5
$\star$	Lu	16.6	710	60	12	-

Table 1. Superconducting transition temperature, T_c, penetration depth, λ, coherence length, ξ, and Ginzburg-Landau parameter, κ, and the zero field magnetic ordering temperature, T_N, for the superconducting borocarbides. The situation in $HoNi_2B_2C$ is more complicated than is evident from the table, as it exhibits 3 different magnetic structures as well as reentrant superconductivity. The compounds which have been investigated for this thesis are marked by asterisks. The listed values are quoted from refs. [4, 6, 7, 8, 9, 10, 11, 12, 13, 14, 15, 16, 17]

pounds" YNi_2B_2C, $ErNi_2B_2C$, $TmNi_2B_2C$ and $LuNi_2B_2C$, as well as the doped materials $Y_{0.75}Lu_{0.25}Ni_2B_2C$ and $Lu(Ni_{1-x}Co_x)_2B_2C$. Despite several attempts we have not been able to observe the FLL in $HoNi_2B_2C$. No experiments have been tried to investigate the FLL in $DyNi_2B_2C$ due to its very high neutron absorption.

1.2 Experimental techniques for FLL imaging

For the investigating the FLL, a number of experimental methods and techniques can be utilized, depending on which kind of information one wants to extract. In general, one can make the distinction between measurements of the dynamic or static properties of the FLL. If the interest is in the dynamic properties such as the depinning critical current and the flux flow resistivity, the supercurrent flow patterns or the FLL melting, the experimental methods would be transport and magnetization (including μ-Hall probe) measurements or Lorentz microscopy. If, on the other hand, the interest is the morphology of the FLL, the choice would be imaging techniques such as small angle neutron scattering (SANS), Bitter decoration, scanning tunneling microscopy (STM), electron holography or magneto optical studies. Finally muon spin rotation (μSR) provides information about the distribution of the magnetic field.

These techniques apply to different experimental conditions. Decoration studies are limited to fields below 1 kOe, where the penetration depth is larger than the flux line spacing. STM probes the electronic structure in the normal flux line core, and is thus applicable at high fields, but depends crucially on the quality of the sample surface. Magneto optics is used for imaging the macroscopic field distribution, but does not have the resolution necessary for resolving individual flux lines. Furthermore, all of these techniques are limited to imaging the FLL at the surface of the superconductor. Lorentz microscopy and electron holography allow a degree of bulk measurements, but are still limited to studies of thin films to faciliate electron transmission through the samples. SANS, on the other hand does not suffer from these limitation, making it the most versatile tool for FLL studies, as described below. Historically the first observation of the FLL, was done by D. Cribier *et al.* in niobium using neutron scattering [18].

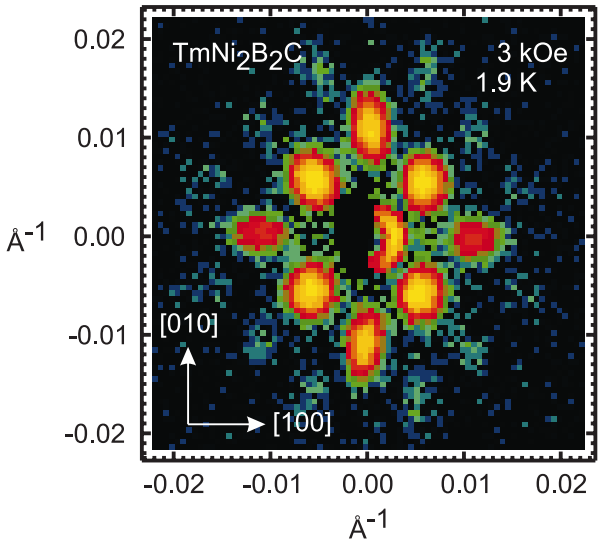

Figure 2. Example of a square FLL diffraction pattern showing several higher order reflections. This diffraction pattern was obtained on $TmNi_2B_2C$ at $T = 1.9$ K and $H = 3$ kOe. The orientation with respect to the crystalline directions is shown by the arrows.

SANS

It is the very fortunate properties of the neutron that makes neutron scattering so useful. The neutron is electrically neutral but still possess a magnetic dipole moment. It interacts with matter in two different ways, namely by the short range nuclear forces, and by dipole interactions with any spatially varying magnetic field distribution. These interactions are weak enough to allow the neutrons to penetrate into the sample, but still strong enough to scatter the neutrons, thereby yielding bulk information. Using neutron scattering we are able to gain information about both the crystal structure, the FLL and the possible magnetic ordering.

SANS allows determination of essentially all the physical properties of the FLL:

- From the diffraction pattern the FLL symmetry can directly be determined.
- Measurements of the scattered intensity allow determination of the superconducting lengthscales λ and ξ, as well as the exact field profile around the flux lines. From this the upper and lower critical fields can be determined.
- The width of the diffraction peaks reveal the FLL correlation lengths, and via models allow the calculation of the critical depinning current density.

1.3 The FLL in the borocarbides

Only one SANS experiment on the FLL in borocarbides was done prior to the work reported in this thesis. This was performed on $ErNi_2B_2C$ in 1995 by U. Yaron *et al.* [19]. They observed a number of novel phenomena. First, the FLL was found to be square in stead of hexagonal, as expected for a relatively high-κ superconductor. An example of a square FLL is shown in figure 2. Secondly, they found a distortion of the FLL and a change in the direction of the flux lines away from the field which was applied along the c-axis. This was attributed to interactions with the magnetic moments on the Er-ions.

In retrospect these discoveries proved a harbinger of the wealth of new phenomena we have since then observed in the borocarbide FLL.

2 Superconductivity, magnetic fields and the flux line lattice

Superconductivity was first observed in 1911 by H. Kamerlingh Onnes as the disappearence of resistivity in the metals mercury, lead and tin at a critical temperature, T_c. Hence the first hallmark of superconductivity, and what gave rise to the name, was perfect conductivity. Later in 1933 Meissner and Ochsenfeld discovered the second hallmark of superconductivity, namely perfect diamagnetism, excluding an applied magnetic field from entering and expelling allready applied fields upon cooling through the superconducting transition at T_c. Finally in 1957 A. A. Abrikosov predicted the existence of a second kind of superconductors named type-II, where the magnetic field would not be expelled, but confined to socalled flux lines arranged in a regular array.

This chapter is not intended as a thorough treatment of the theory of superconductivity, but as an outline introducing superconductivity in general and the FLL in particular. The description is based on the Ginzburg-Landau (GL) theory since it is relatively simple, yet able to provide an understanding of the properties and parameters involved in the desciption of the superconducting state. It is remarkable that this theory was developed in 1950 [20] before the microscopic theory of Bardeen, Cooper and Schrieffer (BCS) [21]. Detailed treatments can for example be found in refs. [22] and [23].

2.1 Ginzburg-Landau theory of superconductivity

The single unifying property of the superconducting state is the existence of a macroscopically coherent wavefunction $\psi(\boldsymbol{r}) = \sqrt{(n_s/2)}e^{i\varphi}$ describing the many-particle condensate with density n_s of superconducting electrons. The strength of the GL theory is its ability to describe systems in which n_s is spatially varying and allowing a non-linear coupling between fields and $|\psi|^2$. As the GL theory is based on a series expansion of $|\psi|^2$ it is limited to regions close to T_c where this quantity is small. If n_s is assumed to be constant in space the results of the GL-theory reduces to the London equations for superconductivity, which are valid at all temperatures below T_c.

The basis of the GL-theory is the expression for the Helmholtz free energy

$$f_s = f_{n0} + \frac{\hbar^2}{4m}\left|\left(\boldsymbol{\nabla} - \frac{2ie}{\hbar c}\boldsymbol{A}\right)\psi\right|^2 + \alpha|\psi|^2 + \frac{\beta}{2}|\psi|^4 + \frac{B^2}{8\pi}, \tag{1}$$

where f_{n0} is the free energy of the normal state in zero field, and the α- and β-terms are the series expansion in $|\psi|^2$. Since ψ describes a condensate of electron pairs (Cooper pairs) the mass and charge are twice the single electrons values.

In the absence of gradients and fields, we find $|\psi|^2 = \psi_\infty^2 \equiv -\alpha/\beta$ by minimizing $f_{s0} - f_{n0}$. This shows that the superconducting transition occurs as α changes sign going from positive to negative, since $\beta > 0$ to ensure a finite ψ and is assumed constant. In the lowest order approximation the temperature dependence of α is linear, $\alpha \propto (T/T_c - 1)$. The fact that the superconducting state is thermodynamically stable, by having a lower energy than the normal state, explains the flux expulsion of the Meissner effect, which cannot be understood by perfect conductivity alone. The energy difference between the superconducting and the normal state in zero field defines the thermodynamic critical field,

$$H_c^2 = 4\pi\frac{\alpha^2}{\beta}. \tag{2}$$

GL equations

The equations used to determine ψ and $\boldsymbol{A}$ are derived from (1) by varying with respect to these quantities. One finds

$$\frac{1}{4m}\left(-i\hbar\boldsymbol{\nabla}-\frac{2e}{c}\boldsymbol{A}\right)^2\psi+\alpha\psi+\beta|\psi|^2\psi=0 \tag{3}$$

and

$$\boldsymbol{\nabla}\times\boldsymbol{B}=\frac{4\pi}{c}\boldsymbol{J}, \tag{4}$$

where $\boldsymbol{J}$ is the superconducting screening current density given by the usual expression

$$\boldsymbol{J}=-\frac{ie\hbar}{2m}(\psi^*\boldsymbol{\nabla}\psi-\psi\boldsymbol{\nabla}\psi^*)-\frac{2e^2}{mc}|\psi|^2\boldsymbol{A}. \tag{5}$$

Equations (3)–(5)are denoted the GL-equations.

Characteristic lengths

From the GL-equations it is possible to extract two characteristic lengths describing the superconducting state.

The first length describe the lengthscale over which the amplitude of ψ can vary without excessive energy cost from the gradient term. Rewriting (3) with $\boldsymbol{A}=0$ and normalizing ψ to the bulk value by changing variable to $\bar{\psi}=\psi/\psi_\infty$, one gets

$$\frac{\hbar^2}{4m\alpha}\nabla^2\bar{\psi}-\bar{\psi}+\bar{\psi}^3=0.$$

From this the coherence length is defined as

$$\xi^2\equiv\frac{\hbar^2}{4m|\alpha|}. \tag{6}$$

The second characteristic length is derived from (4) and (5) assuming a weak magnetic field so that ψ can be assumed everywhere equal to the bulk value, ψ_∞, yielding

$$\nabla^2\boldsymbol{B}=\frac{1}{\lambda^2}\boldsymbol{B}, \tag{7}$$

where

$$\lambda^2=\frac{mc^2\beta}{8\pi e^2|\alpha|}. \tag{8}$$

This length, λ, is the the penetration depth describing how far a magnetic field will extend into the superconducting state before being screened by superconducting currents. The temperature dependence of the penetration depth is $\lambda^2\propto(1-T/T_\mathrm{c})^{-1}$. If $|\alpha|/\beta$ is replaced by $n_\mathrm{s}/2$, which is then assumed spatially constant, λ becomes the London penetration depth given by

$$\lambda_\mathrm{L}^2=\frac{mc^2}{4\pi n_\mathrm{s}e^2}, \tag{9}$$

and (7) becomes one of the London equations.

The GL-parameter is defined as the ratio between the two characteristic lengths,

$$\kappa\equiv\frac{\lambda}{\xi}=\frac{mc\sqrt{\beta}}{(2\pi)^{1/2}e\hbar}, \tag{10}$$

which is seen to be independent of temperature. As shown below the GL-parameter holds great importance to the response of the superconducting state to an applied magnetic field.

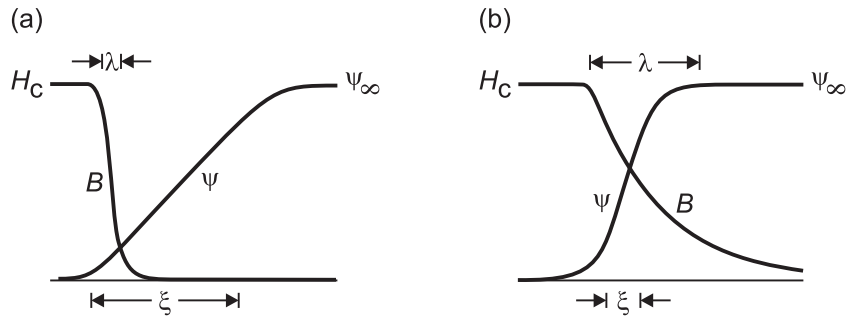

Figure 3. Variation in ψ and B associated with a NS-interface in the case of a type-I ($\kappa < 1/\sqrt{2}$) (a) and a type-II ($\kappa > 1/\sqrt{2}$) (b) superconductor.

Domain wall energy - two types of superconductors

The energy ,γ, associated with a normal-superconduction (NS) interface is a fundamental property determining the reponse to an applied magnetic field equal to H_c. Since $\boldsymbol{H} = \boldsymbol{B} - 4\pi\boldsymbol{M}$ is constant, the correct thermodynamical potential for the calculation is the Gibbs free energy, differing from the Helmholtz free energy by a factor $-\boldsymbol{H}\cdot\boldsymbol{B}/4\pi$:

$$\begin{aligned}\gamma &= \int dV \left(f_{\mathrm{sH_c}} - \frac{H_c B}{4\pi} - f_{\mathrm{nH_c}} + \frac{H_c^2}{4\pi} \right) \\ &= \int dV \left(f_{\mathrm{sH_c}} - f_{\mathrm{n0}} - \frac{H_c B}{4\pi} + \frac{H_c^2}{8\pi} \right). \end{aligned} \tag{11}$$

Considering the simple case of an infinite medium with the NS-interface in the yz-plane and $\boldsymbol{H} \parallel \hat{\boldsymbol{c}}$, it is possible to solve the GL-equations. Introducing dimensionless variables by $\bar{\psi} = \psi/\psi_\infty$ and $\bar{A} = A/H_c\lambda$, and using the gauge $\boldsymbol{A} = (0, A(x), 0)$, the GL-equations become

$$\bar{\psi}'' = \kappa \left(\left(\frac{\bar{A}^2}{2} - 1 \right) \bar{\psi} + \bar{\psi}^3 \right) \tag{12}$$

and

$$\bar{A}'' = \bar{\psi}^2 \bar{A}, \tag{13}$$

where primes denote differentiation with respect to $\bar{x} = x/\lambda$. The expression for the surface energy is then reduced to

$$\gamma = \frac{\lambda H_c^2}{8\pi} \int_{-\infty}^{\infty} d\bar{x} ((\bar{A}' - 1)^2 - \bar{\psi}^4). \tag{14}$$

The sign of γ determines whether the superconducting state will either maximize or minimize the total area of NS-interfaces. Ensuring $\gamma = 0$ by taking $\bar{\psi}^2 = 1 - \bar{A}'$ one finds that the GL-equations are satisfied if $\kappa = 1/\sqrt{2}$. Hence in materials with $\kappa < 1/\sqrt{2}$, which is denoted type-I superconductors, γ is positive so that the energetically most favourable configuration is total expulsion of the magnetic field leading to the Meissner effect. In materials with $\kappa > 1/\sqrt{2}$, the socalled type-II superconductors, γ is negative and the situation is reversed whereby the magnetic field becomes confined to microscopic normal domains with a size determined by ξ.

The domain wall for type-I and type-II superconductors is shown in figure 3.

Flux quantization

The magnetic flux associated with a closed normal region is given by

$$\Phi = \int d\boldsymbol{S}\cdot\boldsymbol{B} = \oint_{\mathrm{C}} d\boldsymbol{l}\cdot\boldsymbol{A}.$$

Taking the contour at distances much greater than λ and ξ, where the superconducting screening current is zero and $\psi = \psi_\infty e^{i\varphi}$, one finds from (5)

$$\boldsymbol{A} = \frac{\hbar c}{2e}\boldsymbol{\nabla}\varphi,$$

which, together with the condition that ψ be single-valued, yields

$$\Phi = \frac{\hbar c}{2e} 2\pi n = n\phi_0.$$

Here ϕ_0 is the flux quantum

$$\phi_0 = \frac{hc}{2e} = 20.7 \times 10^8 \text{ G\AA}^2. \tag{15}$$

Type II superconductivity - upper and lower critical fields

The behaviour of type-II superconductors are determined by two critical fields, denoted the upper critical field, H_{c2}, and the lower critical field, H_{c1}.

Decreasing the field from above the upper critical field i.e. in the normal state, a point is reached where it is energetically favourable to create a superconducting inclusion. Since ψ can be assumed small it is possible to use a linearized GL-equation (3),

$$\frac{1}{4m}\left(-i\hbar\boldsymbol{\nabla} - \frac{2e}{c}\boldsymbol{A}\right) = -\alpha\psi$$

and to take the field uniform and equal to H_{c2}. This equation is equivalent to Schrödingers equation for a free particle with mass $2m$ and charge $2e$ in a magnetic field, with $-\alpha$ taking the place of the energy. The lowest possible energy of a solution to this equation is $E = 1/2\,\hbar\omega_H$ with $\omega_H = eH/mc$ so that

$$-\alpha \geq \frac{e\hbar H}{2mc} \quad \Rightarrow \quad H_{c2} = -\frac{2mc\alpha}{e\hbar}.$$

Using the expressions for H_c, λ, ξ and κ one gets

$$H_{c2} = \sqrt{2}\,\kappa H_c = \frac{\phi_0}{2\pi\xi^2}. \tag{16}$$

Now using the same reasoning as above but increasing the field from zero, it becomes favourable to create a normal inclusion when reaching the lower critical field. Since the domain wall energy is negative the system will tend to create the larges possible fragmentation of the magnetic field, to maximize the NS-interface area. As the magnetic field is quantized this means that each normal inclusion will carry one flux quantum. At H_{c1} the gain in surface energy must exactly match the cost in magnetic energy of the normal region penetrated by the field. Denoting the surface energy per unit length by ε this means

$$\varepsilon L = H_{c1}\int dV \frac{B}{4\pi} = \frac{H_{c1}\phi_0}{4\pi}L \quad \Rightarrow \quad H_{c1} = \frac{4\pi\varepsilon}{\phi_0}.$$

Considering the extreme type-II limit where $\kappa \gg 1$ corresponding to having an infinitely small and thus negligible core region, it is possible to solve the GL-equations yielding the field distribution necessary to calculate ε. Without going through the calculation, but just quoting the result,

$$\varepsilon = \left(\frac{\phi_0}{4\pi\lambda}\right)^2 \ln\kappa$$

the lower critical field is found to be given by

$$H_{c1} = \frac{\phi_0}{4\pi\lambda^2}\ln\kappa. \tag{17}$$

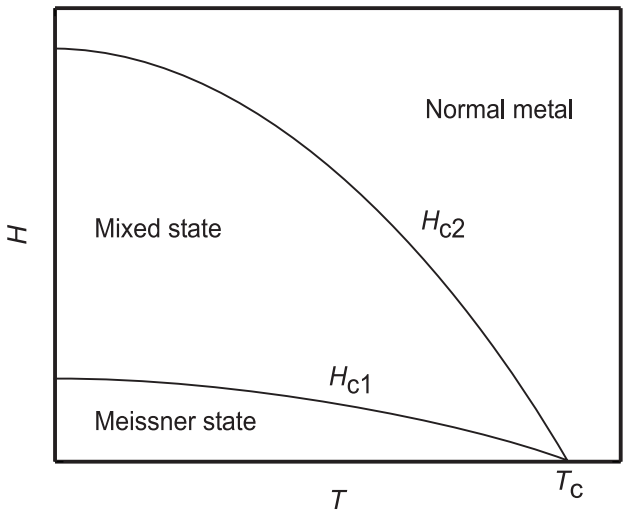

Figure 4. Schematic phase diagram for type-II superconductors showing the Meissner, mixed and normal states, and the boundaries between the different states given by the upper and lower critical fields.

The response of a type-II superconductor to an external magnetic field depends on the magnitude being in one of three ranges. Below H_{c1}, in the Meissner state, the field is expelled similar to the behaviour in a type-I superconductor. Above H_{c1} and below H_{c2}, in the so-called mixed state, the field penetrates in quantized flux lines. Finally above H_{c2} superconductivity is destroyed and the material enters the normal state. In figure 4 the phase diagram for a type-II superconductor is shown.

2.2 The flux line lattice

The existence of a regular array of quantized flux lines, the FLL, was predicted by A. A. Abrikosov in 1957 [24].

Symmetry of the FLL: Square or hexagonal?

Knowing that the magnetic field is confined to filaments or flux lines each carrying one flux quantum and arranged in a lattice, the symmetry of the FLL is found by minimizing $< f_s - f_n >$, where $< \ldots >= \int dV \ldots$ denote a spatial average. Without going into the details, which include numerical calculations, Abrikosov found that at H_{c2}

$$< f_s - f_n >= -\frac{\alpha^2}{\beta}\beta_A^{-1} \quad \text{where} \quad \beta_A \equiv \frac{< \psi^4 >}{< \psi^2 >^2}.$$

In isotropic systems (in the plane parallel to the field) one finds $\beta_A = 1.18$ for the square FLL, monotonically decreasing to $\beta_A = 1.16$ for the hexagonal FLL. Hence the stable symmetry of the FLL is hexagonal, but since the energy difference to a square is only 2% this may be changed by small anisotropies. Historically Abrikosov first got the wrong answer that the FLL in an isotropic system should be square.

Independent of the symmetry the flux line lattice constant is determined by the flux quantization, i.e. that one unit cell must contain one flux quantum, $B = \phi_0/A_0$. Figure 5 shows the square and hexagonal symmetry, including unit cells and flux line spacings. The lattice parameters are

$$a_\square = \sqrt{\frac{\phi_0}{B}} \quad \text{and} \quad a_\triangle = \sqrt{\frac{2}{\sqrt{3}}}\sqrt{\frac{\phi_0}{B}} = 1.075\sqrt{\frac{\phi_0}{B}} \tag{18}$$

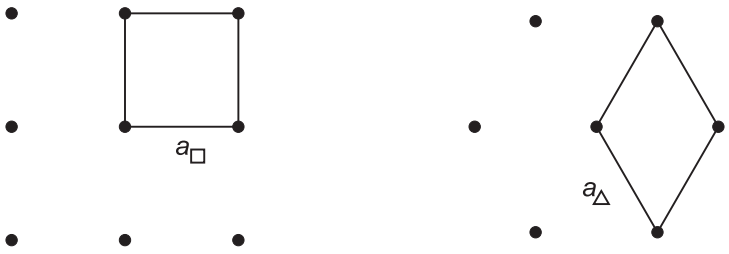

Figure 5. Square (left) and hexagonal (right) FLL symmetries. For each symmetry the unit cell and flux line spacing is shown.

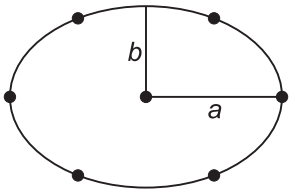

Figure 6. Distorted hexagonal FLL with flux lines positioned on an ellipse with eccentricity, $\Gamma = a/b = 1.5$.

Distorted FLL's

In materials which has a two-fold anisotropy in the plane perpendicular to the applied field a distorted FLL will be observed, an example of which is shown in figure 6 for a hexagonal FLL. The distortion, Γ, yields information on the in-plane effective mass anisotropy by

$$\Gamma = \frac{\lambda_\mathrm{a}}{\lambda_\mathrm{b}} = \frac{\xi_\mathrm{b}}{\xi_\mathrm{a}} = \sqrt{\frac{m_\mathrm{a}}{m_\mathrm{b}}}. \tag{19}$$

Such a two-fold anisotropy can be introduced in the borocarbides by tilting the applied field away from the c-axis. It is also observed in $YBa_2Cu_3O_8$ where the basal plane symmetry is broken by the direction of the Cu-O chains.

However the FLL need not have a high symmetry like square or hexagonal. In the most general case the FLL is spanned by the two vectors

$$\boldsymbol{a} = a_0 \begin{pmatrix} \Gamma \cos\varphi_0 \\ \sin\varphi_0 \end{pmatrix} \tag{20}$$

$$\boldsymbol{b} = a_0 \begin{pmatrix} \Gamma \cos(\varphi_0 + \Delta\varphi) \\ \sin(\varphi_0 + \Delta\varphi) \end{pmatrix}. \tag{21}$$

Here φ_0 gives the orientation with respect to the anisotropy, Γ, and $\Delta\varphi$ is the normalized opening angle, so that $\Delta\varphi = 60^\mathrm{o}$ corresponds to a (distorted) hexagonal lattice and $\Delta\varphi = 90^\mathrm{o}$ to a square lattice. Assuming that the vectors $\boldsymbol{a}$ and $\boldsymbol{b}$ are known, it is possible to derive expressions for φ_0 and $\Delta\varphi$ as follows:

$$\Delta\varphi = \arccos\left(\frac{a_x a_y + b_x b_y}{a_x b_y + a_y b_x}\right) \tag{22}$$

$$\varphi_0 = \arctan\left(\frac{-b_x/a_x + \cos\Delta\varphi}{\sin\Delta\varphi}\right) \tag{23}$$

$$\Gamma = \frac{a_y}{a_x \tan\varphi_0} = \frac{b_y}{b_x \tan(\varphi_0 + \Delta\varphi)}. \tag{24}$$

Depending on the underlying crystal structure and the possible pinning of the FLL to specific crystalline directions, several configurations may be equivalent,

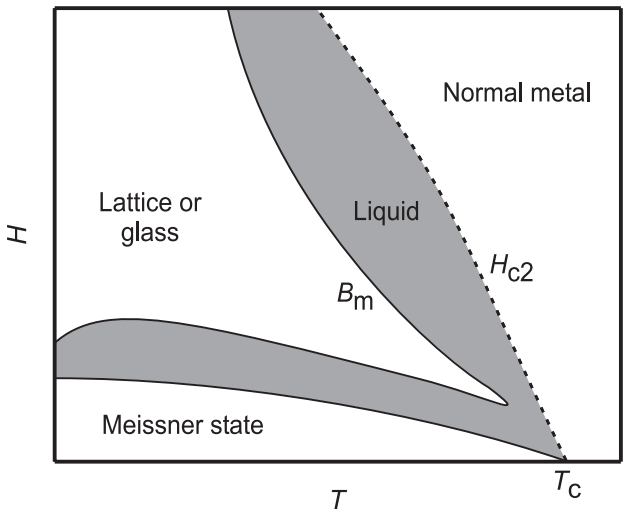

Figure 7. Schematic phase diagram showing the different flux line configurations. Here the melting line is denoted by B_m. The phase diagram resemble that of the high-T_c superconductor $YBa_2Cu_3O_8$, where H_{c2} broadens due to the fluctuations induced by the high temperatures. Even more complicated behaviour, including additional dimensional transitions, is observed in other high-temperature superconductors.

leading to the formation of domains of different orientation. In some cases the anisotropy introduced by tilting the field can be utilized to favour a subset of the equivalent configurations, possibly creating a single domain FLL. Examples of this can be found in refs. [25, 26, 27].

In the borocarbides both different FLL symmetries and transitions between them are observed. This is described in chapters 5 and 7.

2.3 Elastic properties of the FLL

As in ordinary solids small distortions of the FLL can be treated using linear elasticity theory. The amount of literature on the elastic properties of the FLL is legion. For further reading see for example the classical text by R. Huebner [28] or the extensive theoretical reviews by G. Blatter *et al.* [29] and by E. H. Brandt [30].

Flux line lattices, glasses and liquids

The individual flux lines repel. However an additional necessary requirement for the formation of a lattice is the existence of a restoring force opposing small flux line displacements. If such a force is not present, or overcome by thermal fluctuations, other states such as a flux line glass or liquid will be the result. As the temperature or field is changed the flux lines will undergo a transition from a lattice or a glass to a liquid. The existence of different flux line phases and the so-called melting transition was first proposed by D. J. Bishop, P. L. Gammel *et al.* [31, 32] and has been a subject of controversy. It is now broadly accepted after several experimental confirmations. In the borocarbides a FLL melting transition has been reported in refs. [33, 34, 35]. A schematic phase diagram of the flux line states is shown in figure 7.

The behaviour of the FLL is especially important for the transport properties and whether the superconductor is able to carry a current without dissipation. In an ideal, defect-free superconductor the flux lines are unpinned and thus able to move under the influence of a force. The Lorentz force of a transport current

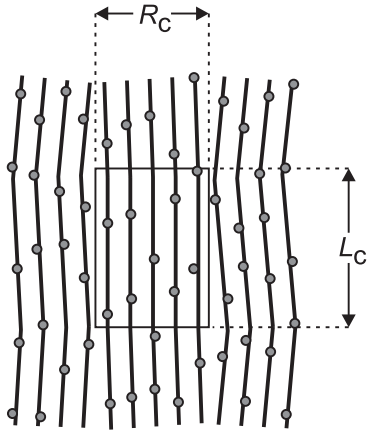

Figure 8. Schematic picture of the concept of correlated volumes. The pinning centres are symbolized by circles. The FLL is undistorted in the volume with longitudinal and radial extension of respectively L_c and R_c.

will accelerate the flux lines leading to dissipation and a voltage drop. This is independent of whether the flux lines are organized in a lattice, a glass or a liquid. If, however, pinning centres for the flux lines are present, a lattice or glass, due to its rigidity, is more effectively pinned than a liquid, leading to a finite critical current. The rigidity is described in terms of the FLL elastic moduli.

Larkin-Ovchinnikov theory of collective pinning

The effect of pinning is most easily described by the Larkin-Ovchinnikov (LO) theory of collective pinning [36]. This assumes a random distribution of pinning centres with density, n, and pinning force, f. The accomodation of the flux lines to the pinning centres are determined by the competition between the pinning energy and the elastic energy from distorting the FLL. In the LO theory the sample volume is divided into correlated volumes, V_c, shown in figure 8, and in which the FLL is essentially undistorted. The size of this volume is determined by the balance betweeen the elastic moduli of the FLL and the pinning force. For point defects the range of the pinning force is determined by ξ, since a reduction in the free energy is only obtained when there is an overlap between the pinning centre and the vortex core. Accordingly the relevant distortion between correlated volumes is given by ξ. As the pinning centres are randomly distributed they add as in a random walk within the correlated volume, and the energy gain is thus $-f\xi\,\sqrt{(n/V_c)}$. The free energy change per unit volume is then

$$\delta F = \frac{1}{2}\,c_{44}\left(\frac{\xi}{L_c}\right)^2 + \frac{1}{2}\,c_{66}\left(\frac{\xi}{R_c}\right)^2 - f\xi\,\sqrt{\frac{n}{V_c}}, \tag{25}$$

where c_{44} and c_{66} are respectively the FLL tilt and shear modulus, and R_c and L_c are the radial and longitudinal dimensions of the correlated volume, $V_c = R_c^2\,L_c$. Minimizing with respect to R_c and L_c one obtains

$$L_c = \frac{2c_{44}\,c_{66}\,\xi^2}{n\,f^2} \tag{26}$$

$$R_c = \frac{\sqrt{2c_{44}}\,c_{66}^{3/2}\,\xi^2}{n\,f^2}. \tag{27}$$

The critical current density, J_c, is estimated by equating the Lorentz force, J_cB, to the pinning force per unit volume $f\,\sqrt{(n/V_c)}$ yielding

$$J_cB = \frac{n^2\,f^4}{2c_{44}\,c_{66}^2\,\xi^3}. \tag{28}$$

Inserting the expression for L_c one finds the following simple relation

$$J_c B = \frac{2c_{44}\,\xi}{L_c^2}. \tag{29}$$

Good agreement to the LO theory was found combining small angle neutron scattering on $NbSe_2$ measuring L_c and transport measurements of J_c [37].

In chapter 6 I compare results obtained on YNi_2B_2C and $LuNi_2B_2C$ to the LO-theory.

Elastic moduli of the FLL

Simple expression for the FLL elastic moduli was derived by E. H. Brandt [30, 38]:

$$c_{44} = \frac{BH}{4\pi}\,\frac{1}{1+(\lambda k)^2} \tag{30}$$

$$c_{66} = \frac{H_c^2}{16\pi}\,b\,(1-0.58b+0.29b^2)\,(1-b)^2, \qquad b=\frac{B}{H_{c2}}. \tag{31}$$

The dispersion in the tilt modulus, c_{44}, depends on the periodicity, $2\pi/k$, of the flux lattice distortion. In the LO theory $k \sim 1/L_c$ or $1/R_c$. The shear modulus, c_{66}, is calculated for a hexagonal FLL, and is valid in the high-κ regime. No expression for the shear modulus of a square FLL exists.

3 Small angle neutron scattering

This chapter describes the theoretical and experimental details related to small angle neutron scattering (SANS) studies of the FLL. First a brief summary of neutron scattering basics is given, followed by the particular case of scattering from the flux line lattice. Then the samples and neutron transmission through the samples are briefly discussed. Finally there is a section describing the experimental setup.

3.1 Elementary neutron scattering

A number of textbooks on neutron scattering exist. For further reading see for example the text by Bacon [39].

The direct and the reciprocal lattice

The concept of the reciprocal lattice proves very useful in dealing with the theory of neutron scattering. The starting point is the direct lattice decribing the position of the atoms, or unit cells if the crystal consists of more than one element, in terms of three basisvectors, $\boldsymbol{a}$, $\boldsymbol{b}$ and $\boldsymbol{c}$, so that the atom positions are given by

$$\boldsymbol{r} = n_1\boldsymbol{a} + n_2\boldsymbol{b} + n_3\boldsymbol{c}.$$

Here $0 \leq n_i \leq N_i - 1$ and $N = N_1N_2N_3$ is the total number of atoms. The basisvectors of the reciprocal lattice, $\boldsymbol{a}^*$, $\boldsymbol{b}^*$ and $\boldsymbol{c}^*$, are then defined by

$$\boldsymbol{a}^* = \frac{2\pi}{V_0}\,\boldsymbol{b}\times\boldsymbol{c} \tag{32}$$

$$\boldsymbol{b}^* = \frac{2\pi}{V_0}\,\boldsymbol{c}\times\boldsymbol{a} \tag{33}$$

$$\boldsymbol{c}^* = \frac{2\pi}{V_0}\,\boldsymbol{a}\times\boldsymbol{b} \tag{34}$$

$$V_0 = \boldsymbol{a}\cdot\boldsymbol{b}\times\boldsymbol{c}, \tag{35}$$

where V_0 is the unit cell volume. The direct and reciprocal lattice vectors have the following properties:

$$\boldsymbol{a}\cdot\boldsymbol{a}^* = \boldsymbol{b}\cdot\boldsymbol{b}^* = \boldsymbol{c}\cdot\boldsymbol{c}^* = 2\pi \tag{36}$$

$$\boldsymbol{a}\cdot\boldsymbol{b}^* = \boldsymbol{a}\cdot\boldsymbol{c}^* = \boldsymbol{b}\cdot\boldsymbol{a}^* = \boldsymbol{b}\cdot\boldsymbol{c}^* = \boldsymbol{c}\cdot\boldsymbol{a}^* = \boldsymbol{c}\cdot\boldsymbol{b}^* = 0. \tag{37}$$

In two dimensions it is an inherent property, that the direct and reciprocal lattice are simply related by a 90° rotation and a rescaling of the axes. The analysis in section 2.2 of the FLL orientation, symmetry and distortion in direct space, can therefore equally well be applied in reciprocal space.

Scattering geometry and Bragg's Law

The initial and final propagation vectors of the incident and scattered neutrons respectively, are denoted by $\boldsymbol{k}_\mathrm{i}$ and $\boldsymbol{k}_\mathrm{f}$. The scattering vector $\boldsymbol{q}$ is then defined by

$$\boldsymbol{k}_\mathrm{f} = \boldsymbol{k}_\mathrm{i} + \boldsymbol{q}, \tag{38}$$

as shown in figure 9. As will become evident in the next section $\boldsymbol{q}$ must be a reciprocal lattice vector before scattering will occur. Defining the scattering angle,

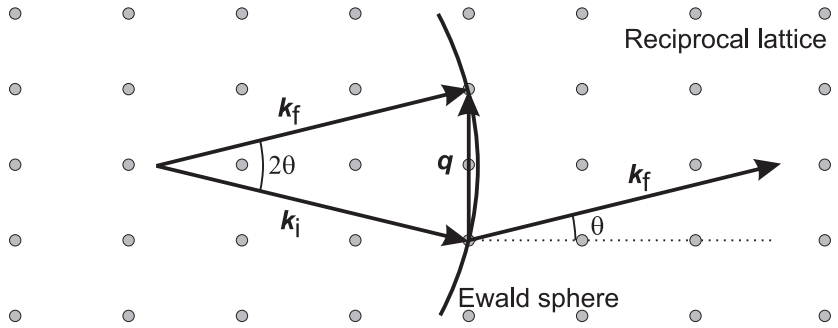

Figure 9. Scattering geometry. The propagation vectors of the ingoing and outcoming neutrons differ by $\boldsymbol{q}$, which must coincide with a reciprocal lattice vector to satisfy the Bragg condition. The Ewald sphere spanned by $\boldsymbol{k}_i$ and $\boldsymbol{k}_f$ is also shown.

θ, as shown in the figure, and considering only elasctic scattering so that $k_\mathrm{i} = k_\mathrm{f}$, one finds Bragg's Law

$$q = 2k \sin\theta. \tag{39}$$

This has a simple interpretation as mirror reflection in planes drawn through direct lattice points, where the angle θ corresponds to a path difference, between reflection in two adjacent planes with a spacing d, which is exactly one neutron wavelength, λ_n. Since $\boldsymbol{q}$ is perpendicular to the mirror planes and has the magnitude $q = 2\pi/d$, Bragg's Law in direct space becomes

$$\lambda_\mathrm{n} = 2d \sin\theta. \tag{40}$$

Unless a quantitative analysis of the scattered intensities is required, Bragg's Law is essentially all that is needed to conduct a neutron scattering experiment. However a detailed analysis of the scattered intensities will allow absolute form factor determination and extraction of physical quantities.

Another way of illustrating the scattering condition is using the Ewald construction, which too is shown in figure 9. The Ewald sphere has a radius k, and origo at the endpoint of $\boldsymbol{k}_\mathrm{i}$. The condition for scattering to occur is that the scattering vector, $\boldsymbol{q}$, connect two reciprocal lattice points lying on the surface of the sphere, as shown in the figure.

The differential scattering cross section

The scattered intensity is found from the differential scattering cross section, which describes the number of neutrons which are scattered into a solid angle $d\Omega$ per second divided by the incident flux. The differential scattering cross section is given by

$$\frac{d\sigma}{d\Omega} = \left| \sum_n b_n \, e^{i\boldsymbol{q}\cdot\boldsymbol{r}_n} \right|^2, \tag{41}$$

where n is a sum over all scatterers (atoms or flux lines) in the crystal and b_n is the scattering length of the n'th scatterer. The difference between nuclear and magnetic scattering is contained in the different expressions for the scattering length.

Nuclear scattering

For nuclear scattering the sum over all atoms can be split into two sums: One over one unit cell and one over all the unit cells of the crystal. Writing the position of

the atoms as $(n_1\boldsymbol{a} + n_2\boldsymbol{b} + n_3\boldsymbol{c}) + \boldsymbol{r}_m$, where $\boldsymbol{r}_m$ is the position within the unit cell, and $\boldsymbol{q} = h\boldsymbol{a}^* + k\boldsymbol{b}^* + l\boldsymbol{c}^*$, and utilizing equations (36) and (37) one gets

$$\frac{d\sigma}{d\Omega} = \left| \sum_{n_{1,2,3}} e^{2\pi i(n_1 h + n_2 k + n_3 l)} \sum_m b_m \, e^{i\boldsymbol{q}\cdot\boldsymbol{r}_m} \right|^2 .$$

Here b_m is the nuclear scattering length which is tabulated for all the elements and their isotopes. The first sum can be expressed as a sum of delta functions positioned at all reciprocal lattice vectors, $\boldsymbol{Q} = h\boldsymbol{a}^* + k\boldsymbol{b}^* + l\boldsymbol{c}^*$, with h, k, l being integers:

$$\left| \sum_{n_{1,2,3}} e^{2\pi i(n_1 h + n_2 k + n_3 l)} \right|^2 = \frac{(2\pi)^3}{V_0} N \sum_{\boldsymbol{Q}} \delta(\boldsymbol{q} - \boldsymbol{Q}).$$

Defining the nuclear structure factor as

$$F(\boldsymbol{q}) = \sum_m b_m \, e^{i\boldsymbol{q}\cdot\boldsymbol{r}_m}, \tag{42}$$

one obtains the following expression for the nuclear differential scattering cross section

$$\frac{d\sigma}{d\Omega} = \frac{(2\pi)^3}{V_0} N \sum_{\boldsymbol{Q}} \delta(\boldsymbol{q} - \boldsymbol{Q}) \, |F(\boldsymbol{q})|^2. \tag{43}$$

Magnetic scattering

As the neutrons posseses a magnetic moment any ordered magnetic structure or magnetic field distribution will also give rise to scattering. The scattering length in equation (41) will then consist of two components: One from the nuclear scattering (N) and one from magnetic scattering (M). As the magnetic moments and fields have a direction as well as a magnitude the scattering length becomes a vector, with the scattering depending on the orientation with respect to the neutron spin, $\frac{1}{2}\hat{\boldsymbol{\sigma}}$, so that

$$b = b_{\mathrm{N}} + b_{\mathrm{M}}, \text{ with } b_{\mathrm{M}} = \hat{\boldsymbol{\sigma}} \cdot \boldsymbol{b}_{\mathrm{M}}. \tag{44}$$

In general this will lead to an interference term between nuclear and magnetic scattering, but for the case of unpolarized neutrons that will average to zero. Polarized neutron scattering of the FLL in niobium utilizing the interference has been reported by K.-U. Neumann *et al.* [40].

The scattering length from a magnetic field distribution (atoms or flux lines) is given by

$$b_{\mathrm{M}} = \frac{V(\boldsymbol{q})}{4\pi \, \hbar^2/2m_{\mathrm{n}}} \tag{45}$$

in the Born approximation, where $V(\boldsymbol{q})$ is the Fourier transform of the interaction potential. This is given in terms of the neutron gyromagnetic ratio $\gamma = 1.91$, the nuclear magneton $\mu_{\mathrm{N}} = e\hbar/2m_{\mathrm{n}}c$ and the magnetic field distribution, by

$$V(\boldsymbol{r}) = \gamma \, \mu_{\mathrm{N}} \, \hat{\boldsymbol{\sigma}} \cdot \boldsymbol{B}(\boldsymbol{r}). \tag{46}$$

In the case where the field is created by the dipolar field of an unpaired electron at an atom site the potential is

$$V(\boldsymbol{q}) = 4\pi \, \gamma \, \mu_{\mathrm{N}} \, \mu_{\mathrm{B}} \, \hat{\boldsymbol{\sigma}} \cdot \hat{\boldsymbol{q}} \times (\hat{\boldsymbol{\mu}} \times \hat{\boldsymbol{q}}), \tag{47}$$

where $\mu_B = e\hbar/2m_e c$ is the Bohr magneton, $\hat{\boldsymbol{q}} = \boldsymbol{q}/q$ and $\hat{\boldsymbol{\mu}} = \boldsymbol{\mu}/\mu_B$. The term $\hat{\boldsymbol{q}} \times (\hat{\boldsymbol{\mu}} \times \hat{\boldsymbol{q}})$ means that only the component of the ordered moment which is perpendicular to the scattering vector will give rise to scattering. The magnetic scattering length to be inserted into equation (41) for the differential scattering cross section then becomes

$$b_M = \frac{\gamma\,\mu_N\,\mu_B}{\hbar^2/2m_n}\, f(\boldsymbol{q})\, \hat{\boldsymbol{\sigma}} \cdot \hat{\boldsymbol{q}} \times (\hat{\boldsymbol{\mu}} \times \hat{\boldsymbol{q}}), \tag{48}$$

where the magnetic form factor $f(\boldsymbol{q})$ is the Fourier transform of the electron density

$$f(\boldsymbol{q}) = \int d\boldsymbol{r}_e\, \rho(\boldsymbol{r}_e)\, e^{i\boldsymbol{q}\cdot\boldsymbol{r}_e}. \tag{49}$$

If the magnetic structure is commensurate, i.e. if the magnetic modulation has a periodicity equal to a rational number times a lattice vector, the sum in equation (41) can be split similar to the nuclear scattering, yielding a magnetic structure factor by summing just the magnetic unit cell. If the magnetic structure is incommensurate the sum cannot be split, but must be evaluated for the entire crystal.

As a simple example consider an incommensurate transverse spin density wave with a sinusoidal modulation and periodicity $2\pi/q_m$. This resembles the zero field magnetic structure found in $TmNi_2B_2C$. The position of the Bragg peaks is determined by the sum

$$\left|\sum_n \sin(\boldsymbol{q}_m \cdot \boldsymbol{r}_n)\, e^{i\boldsymbol{q}\cdot\boldsymbol{r}_n}\right|^2 = \frac{1}{4}\left|\sum_n \left(e^{i(\boldsymbol{q}+\boldsymbol{q}_m)\cdot\boldsymbol{r}_n} - e^{i(\boldsymbol{q}-\boldsymbol{q}_m)\cdot\boldsymbol{r}_n}\right)\right|^2,$$

which gives delta functions at all reciprocal lattice points plus and minus the magnetic scattering vector, i.e. $\sum_{\boldsymbol{Q}} \delta(\boldsymbol{q} - \boldsymbol{Q} \pm \boldsymbol{q}_m)$.

3.2 Neutron scattering of the FLL

Scattering of the FLL is equivalent to scattering from magnetic moments at the atom sites, the only difference being the much larger periodicity.

Magnetic scattering of the FLL

The scattering length is simply

$$b_{FLL} = \frac{\gamma\,\mu_N}{4\pi\,\hbar^2/2m_n}\, \hat{\boldsymbol{\sigma}} \cdot \int d\boldsymbol{r}\, \boldsymbol{B}(\boldsymbol{r})\, e^{i\boldsymbol{q}\cdot\boldsymbol{r}}. \tag{50}$$

Since the FLL is a periodic structure it is convenient to express the field distribution by a two-dimensional Fourier series

$$\boldsymbol{B}(\boldsymbol{r}) = \sum_{\boldsymbol{q}} \boldsymbol{h}(\boldsymbol{q})\, e^{i\boldsymbol{q}\cdot\boldsymbol{r}}, \tag{51}$$

so that $\boldsymbol{B}(\boldsymbol{q}) = A_0 t\, \boldsymbol{h}(\boldsymbol{q})$, where $A_0 = \phi_0/B$ is the FLL unit cell area determined by the applied field, and t is the sample thickness. Inserting the expression for the nuclear magneton one finds $\mu_N/(4\pi\,\hbar^2/2m_n) = 1/4\phi_0$, and the scattering length then becomes

$$b_{FLL} = \frac{\gamma}{4\phi_0}\, A_0 t\, \hat{\boldsymbol{\sigma}} \cdot \boldsymbol{h}(\boldsymbol{q}). \tag{52}$$

Finally the differential scattering cross section is

$$\frac{d\sigma}{d\Omega} = (2\pi)^3 \left(\frac{\gamma}{4\phi_0}\right)^2 A_{sample}\, t \sum_{\boldsymbol{Q}} \delta(\boldsymbol{q} - \boldsymbol{Q})\, |\boldsymbol{h}(\boldsymbol{q})|^2. \tag{53}$$

Measurement of the scattered intensity thus allows determination of the FLL magnetic form factor, $|\boldsymbol{h}(\boldsymbol{q})|^2$.

The magnetic form factor of a flux line

Calculation of the magnetic form factor of a flux line needs the detailed knowledge of the exact field distribution. The simplest approximation is using the London equations, which are obtained from the Ginzburg Landau-equations (3-5) by setting $|\psi|^2$ constant and equal to $n_s/2$:

$$\boldsymbol{\nabla} \times \boldsymbol{\nabla} \times \boldsymbol{B} + \frac{\boldsymbol{B}}{\lambda_L} = 0. \tag{54}$$

This equation in itself does not contain the FLL. Adding by hand flux lines at lattice positions this is modified to

$$\lambda_L \, \boldsymbol{\nabla} \times \boldsymbol{\nabla} \times \boldsymbol{B} + \boldsymbol{B} = \hat{\boldsymbol{z}} \, \phi_0 \sum_i \delta_{2D}(\boldsymbol{r} - \boldsymbol{r}_i). \tag{55}$$

Utilizing the Fourier expansion in equation (51) yields the following result:

$$\boldsymbol{h}(\boldsymbol{q}) = \frac{B}{1 + \lambda_L^2 \, q^2}. \tag{56}$$

This result was obtained with unphysical condition of a point core size. The effect of a finite core size of radius ξ is frequently taken into account by introducing a Gaussian cut-off, $e^{-c\xi^2 q^2}$, where c is a constant ranging from $\frac{1}{4}$ to 2 [41]. Hence form factor measurements can be used to derive values for the superconducting penetration depth and coherence length. In this work the constant value $c = \frac{1}{2}$ is used, which in the litterature [19, 42, 43] has been found to yield results for ξ in reasonable agreement with H_{c2} measurements.

Now since the form factor measurements are performed at relatively high fields, $H > 1kOe$, one have $(\lambda q)^2 \geq 5$ and using $q^2 = (2\pi)^2 \, B/\phi_0$ for the square lattice, the form factor is approximated by

$$\boldsymbol{h}(\boldsymbol{q}) = \frac{\phi_0}{(2\pi \, \lambda)^2} \, e^{-2\pi^2 B \xi^2/\phi_0}. \tag{57}$$

Using the London penetration depth one finds $h(q) \propto n_s$, i.e. in the conventional language of neutron scattering the FLL order parameter is proportional to the density of superconducting electrons. Form factor measurements, using the above expression to extract λ and ξ, are reported in chapter 4.

Among other, more involved models for the flux line form factor one finds the Clem-model [44], which have a more realistic description of the field distribution in the vicinity of the vortex core.

Total scattered intensity

Due to imperfections in the crystal and the finite instrumental resolution the Bragg peaks are not delta functions, but rather they are smeared in reciprocal space. In order to relate the measured intensities to the expressions for the form factor, one therefore measures the integrated intensity by rotating through the reflection. The total number of scattered neutrons from a given reflection is given by

$$N = I_0 \int d\Omega \int dt \, \frac{d\sigma}{d\Omega}, \tag{58}$$

where I_0 is the neutron flux per area and time. Considering the integrations in a coordinate system where the scattered neutrons move parallel to the x-axis, one gets

$$\int d\Omega = \int \frac{dy \, dz}{k^2}.$$

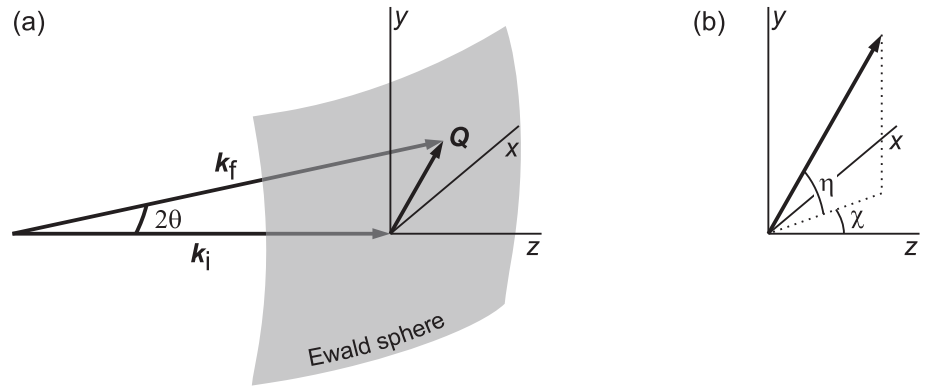

Figure 10. Geometry for calculation of the Lorentz factor in the SANS setup. Left side (a) shows the propagation and scattering vectors, and right side (b) defines the orientation angles.

The integration in time is given by

$$\int d\tau = \int \frac{dx}{v},$$

where v is the phase space-velocity with which the reflection moves through the Ewald sphere. This velocity depends on q, the speed of rotation, ω, and the angle at which the scattering vector cuts the Ewald sphere. This is also called the Lorentz factor.

Lorentz factor for the SANS spectrometer

The geometry used to calculate the Lorentz factor for the SANS spectrometer is shown in figure 10. Note that the coordinate system used here is different from the one used in the previous section. The sample, and hence $\boldsymbol{Q}$, is rotated about the y-axis with an angular speed ω. One then has:

$$\boldsymbol{k}_\mathrm{i} = \begin{pmatrix} 0 \\ 0 \\ k \end{pmatrix}, \qquad \boldsymbol{k}_\mathrm{f} = k \begin{pmatrix} \cos\eta_k \ \sin\chi_k \\ \sin\eta_k \\ \cos\eta_k \ \cos\chi_k \end{pmatrix} \text{ and} \tag{59}$$

$$\boldsymbol{Q} = q \begin{pmatrix} \cos\eta_Q \ \sin(\chi_Q + \omega\tau) \\ \sin\eta_Q \\ \cos\eta_Q \ \cos(\chi_Q + \omega\tau) \end{pmatrix}. \tag{60}$$

Defining $\boldsymbol{q} = \boldsymbol{k}_\mathrm{f} - \boldsymbol{k}_\mathrm{i}$ and using that η_Q is fixed, it is possible to determine η_k, χ_k and χ_Q from the Bragg condition $\delta(\boldsymbol{q} - \boldsymbol{Q})$ at $\tau = 0$.

Utilizing the usual definition of the scattering angle

$$\frac{\boldsymbol{k}_\mathrm{i} \cdot \boldsymbol{k}_\mathrm{f}}{k^2} = \cos\eta_k \ \cos\chi_k = \cos 2\theta, \tag{61}$$

it is possible to calculate the phase space velocity v with which $\boldsymbol{Q}$ cuts through the Ewald sphere:

$$v = \frac{d}{dt} \frac{\boldsymbol{k}_\mathrm{f} \cdot \boldsymbol{Q}}{k} \bigg|_{\tau=0} = q\omega \sqrt{\cos^2\eta_Q - \sin^2\theta}. \tag{62}$$

As all the experiments are performed in the small angle limit this is approximated by

$$v = q\omega \ \cos\eta_Q. \tag{63}$$

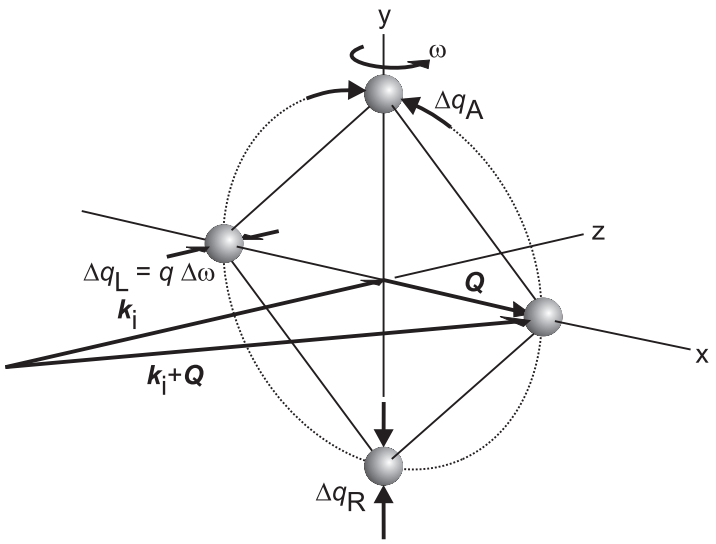

Figure 11. Bragg peak widths in reciprocal space for a square FLL. The widths are generally different in the three different directions: radial, azimuthal and longitudinal.

FLL integrated reflectivity

Combining the results from the previous sections, it is customary to define the integrated intensity by $N\omega/I_0$. This quantity, which is independent of the angular speed of rotation and the incident neutron flux, is

$$\begin{aligned}\frac{N\omega}{I_0} &= (2\pi)^3 \left(\frac{\gamma}{4\phi_0}\right)^2 A_{\text{sample}}\, t \int \frac{dx\, dy\, dz}{k^2 q \cos\eta_Q} \sum_{\boldsymbol{Q}} \delta(\boldsymbol{q}-\boldsymbol{Q})|\boldsymbol{h}(\boldsymbol{q})|^2 \\ &= \frac{2\pi\,\gamma^2\lambda_{\text{n}}^2\, t}{16\phi_0^2\, q\, \cos\eta_Q} A_{\text{sample}}\, |\boldsymbol{h}(\boldsymbol{Q})|^2.\end{aligned}$$

Normalizing this to the sample area we finally obtain the integrated reflectivity

$$R = \frac{N\omega}{I_0\, A_{\text{sample}}} = \frac{2\pi\,\gamma^2\lambda_{\text{n}}^2\, t}{16\phi_0^2\, q\, \cos\eta_Q}\, |\boldsymbol{h}(\boldsymbol{Q})|^2. \tag{64}$$

In practice the integrated intensity is not measured by collecting the scattered neutrons while rotating the sample, but in stead by measuring at a discrete number of angular settings.

FLL correlation lengths

As discussed above the Bragg relections will have finite widths in reciprocal space due to FLL imperfections and the instrumental resolution. As far as it is possible to deconvolute these two contributions, and thereby subtract the instrumental resolution, this will allow determination of the FLL correlation lengths. Figure 11 shows the widths in the radial, azimuthal and longitudinal directions. If the correlation function decay exponentially with distance, the lineshape in reciprocal space will be Lorentzian, and the correlation length, $\xi_{\text{corr.}}$, is given of Δq (FWHM), by

$$\xi_{\text{corr.}} = \frac{2}{\Delta q}. \tag{65}$$

In the SANS geometry the resolution in the three directions is different, as the longitudinal resolution is optimized on expense of the in-plane (radial and azimuthal) resolution. We are therefore better able to study the FLL order along

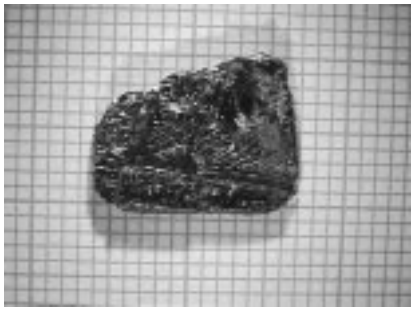

Figure 12. Photograph of a typical sample for a SANS experiment. The crystal shown is Co-doped $LuNi_2B_2C$ with an area of 100 mm^2, a thickness of 0.8 mm and a mass of 530 mg.

the direction of the flux lines. As the longitudinal width is determined from the rocking curve width, the same Lorentz factor that was found for the integrated intensity applies. The experimental resolution will be treated further in the section decribing the SANS spectrometer.

FLL correlation length measurements are reported in chapter 6.

3.3 Samples and neutron transmission

All crystals used for the experiments reported in this thesis was grown by P. C. Canfield from Ames Laboratory using a high temperature flux method [15]. A photograph of a sample, typical for the ones used in the SANS experiments, is shown in figure 12.

To reduce the thermal neutron absorption all crystals were grown using isotopically separated ^{11}B (purity 99.5%). Since the absorption varies dramatically among the rare earths, so does the transmision for the different borocarbides, and substantial reductions are possible using isotopically enriched elements. Using crystal lattice parameters $a = 3.5$Å and $c = 10.6$Å, and the absorption cross sections, $\sigma_{\rm abs}$, listed in table 2, it is possible to calculate the transmission, T, versus sample thickness, t. It is given by

$$T = \exp\left(-\frac{t}{V_{\rm u.c.}}\,\frac{\lambda_{\rm n}}{1.8\text{Å}}\,\sum_{\rm u.c.}\sigma_{\rm abs.}\right), \tag{66}$$

where $V_{\rm u.c.}$ is the unit cell volume and the sum is over the atoms in the unit cell. The transmission of the borocarbides versus sample thickness for a neutron wavelength of $\lambda_{\rm n} = 9$ Å is shown in figure 13. All crystals used for this work were grown using rare earths with the natural composition of isotopes.

3.4 SANS experimental setup

All SANS experiments were performed in the cold neutron guide hall (Neutronhuset) of the DR3 research reactor at Risø National Laboratory.

SANS spectrometer

The SANS spectrometer consists of a number of components shown scematically in figure 14. The components are the following:

Velocity selector Used for neutron wavelength selection, and consists of a drum of absorbing material with propagation channels for the neutrons. By placing the velocity selector at an angle with respect to the neutron beam and rotating

Symbol	Z A	Natural abundance	σ_{abs} (barn)
B	5		767
	11	80.0%	0.0055
C	6		0.00350
Ni	28		4.49
Y	39		1.28
Dy	66		994
	162	25.5%	194
	163	24.9%	124
Ho	67		64.7
Er	68		159
	166	33.3%	19.6
	168	27.1%	2.74
Tm	69		100
Lu	71		74

Table 2. Neutron absorption cross sections at 2200 m/s (λ_n =1.8 Å) for the elements (with atomic number Z) making up the superconducting borocarbides. Both values for the natural occuring composition of isotopes are listed, together with specific isotopes (with mass number A) if they have a high natural abundance ($\geq$ 20%) and a significantly lower absorption cross section. The values in this table are from V. F. Sears [45].

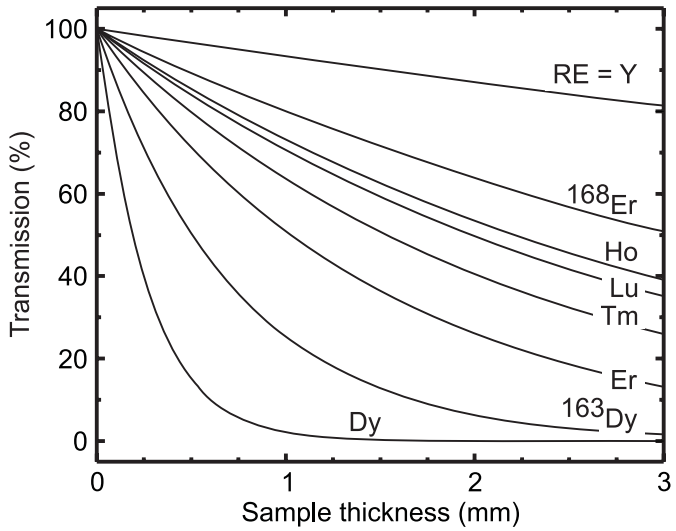

Figure 13. Calculated transmission versus sample thickness of the different borocarbides for 9 Å neutrons assuming 99.5% ^{11}B. *In addition the transmission using 75% pure* ^{163}Dy *and* ^{168}Er *is shown.*

it at a constant speed, both a specific wavelength and bandwidth can be selected.

Collimation section Used to define the beam divergence, and is comprised of two pinholes of varying size and separation. The diameter is typically 16 or 25 mm and the spacing can be varied from 1 to 6 m in one meter increments.

Sample table Here the sample can be placed in a suitable environment, e.g. cryostat, pressure cell, etc.

Position sensitive detector Counts the scattered neutrons and can be positioned at any distance from 1.2 to 6 m from the sample.

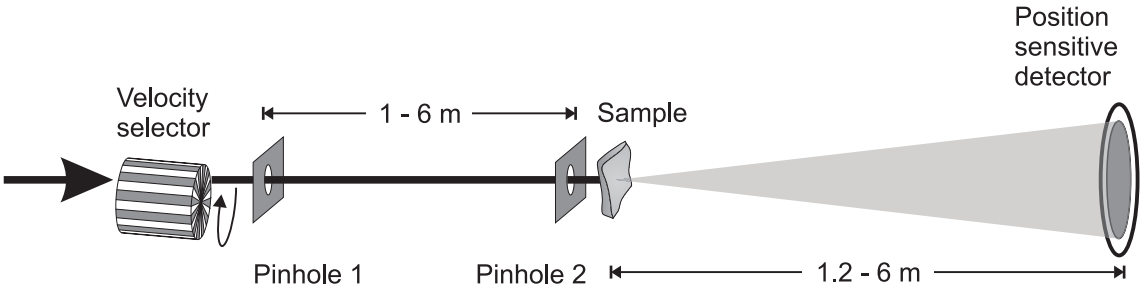

Figure 14. Schematic diagram showing the setup of the SANS beamline.

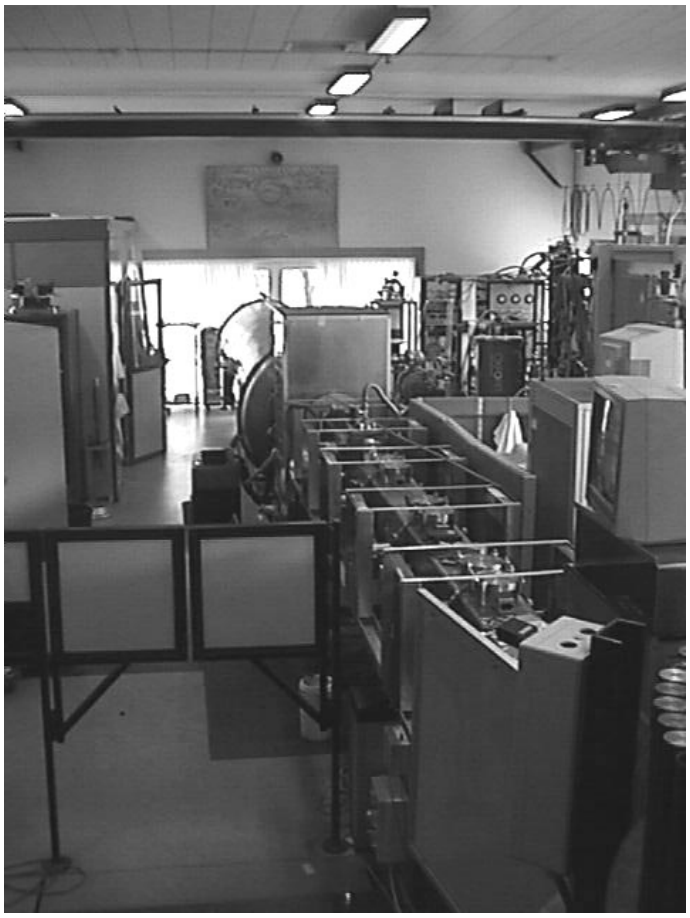

Figure 15. Picture showing the SANS beamline. In the front one sees the collimation section, followed by the sample station. In the back is the evacuated tank holding the detector.

Both the collimation section and the detector are kept in vacuum to reduce air scattering and beam attenuation. All passages between vacuum and atmosphere were through single crystal sapphire windows to reduce the small angle background as much as possible. In figure 15 a picture shows the SANS beamline.

Below, each element in the beamline is decribed in detail with regard to its influence on the accesible range and resolution in reciprocal space.

Instrumental resolution

The instrumental resolution is determined by the velocity selector, the collimation section and the detector. In this work very simple approximations for the experimental resolution have been used, and are briefly described below. All resolution functions are approximated by Gaussians and added in quadrature. For a detailed treatment and more accurate results see the Ph.D. thesis by P. Harris [46] and references therein. This describtion is based on the SANS spectrometer settings used for the FLL studies, i.e. the extreme small angle limit with a collimation section and a sample to detector distance of both 6 m.

The radial and longitudinal resolution has two contributions. One from the angular collimation of the neutron beam and one from the wavelength spread of the neutrons. The azimuthal resolution is only affected by the collimation. From the different components one gets:

Velocity selector This acts both as a horizontal collimator and a wavelength selector. The collimation is however much coarser than what is imposed by the collimation section, and is therefore not considered. The selected wavelength is determined by speed of rotation, ν, and the angle, ϕ, between the channels and the incident neutrons:

$$\lambda_{\mathrm{n}} \propto \frac{\tan\phi}{\nu}. \tag{67}$$

The wavelength spread, $\Delta\lambda_{\mathrm{n}}/\lambda_{\mathrm{n}}$, is determined by ϕ and the length, l, and width, d, of the channels:

$$\frac{\Delta\lambda_{\mathrm{n}}}{\lambda_{\mathrm{n}}} = \frac{d}{l\,\sin\phi}. \tag{68}$$

The spread is thus independent of the specific wavelength. The usual settings are $\Delta\lambda_{\mathrm{n}}/\lambda_{\mathrm{n}} = 9, 18$ and 36%. The wavelength spread translates into an angular spread in the scattering process. From Bragg's Law in the small angle approximation $2\theta = q\lambda_{\mathrm{n}}/2\pi$, one obtains

$$\Delta(2\theta)_{\mathrm{W.S.}} = \frac{q\lambda_{\mathrm{n}}}{4\pi}\sqrt{\frac{4\ln 2}{3}}\,\frac{\Delta\lambda_{\mathrm{n}}}{\lambda_{\mathrm{n}}}. \tag{69}$$

The numerical factor arise in the translation from variation to FWHM, and from approximating the wavelength profile by a Gaussian.

Collimation section The beam divergence from the two pinholes are determined by their size and separation. As the second pinhole effectively is the mask determined by the sample size, the two pinholes will in general be of different size. Denoting the pinhole diameters by w_1 and w_2 and the separation by l the beam divergence is

$$\Delta(2\theta)_{\mathrm{B.D.}} = 2\sqrt{2\ln 2}\,\frac{\sqrt{(w_1/l)^2 + (w_2/l)^2}}{4}. \tag{70}$$

Detector resolution The detected neutrons are binned into 5×5 mm^2 pixels which roughly correspond to the actual spatial resolution of the detector. This resolution is better than the Bragg spot size produced by the collimation, and is therefore not contributing to the in plane resolution.

It is now possible to write the resolution in the three directions:

$$\Delta q_{\mathrm{R}}^2 = (k\,\Delta(2\theta)_{\mathrm{W.S.}})^2 + (k\,\Delta(2\theta)_{\mathrm{B.D.}})^2 \tag{71}$$

$$\Delta q_{\mathrm{A}}^2 = (k\,\Delta(2\theta)_{\mathrm{B.D.}})^2 \tag{72}$$

$$\Delta q_{\mathrm{L}}^2 = (q\,\Delta(2\theta)_{\mathrm{W.S.}})^2 + (q\,\Delta(2\theta)_{\mathrm{B.D.}})^2. \tag{73}$$

$\Delta\lambda_n/\lambda_n$	q_{max} (Å^{-1})	d_{min} (Å)
9%	0.27	23.3
18%	0.55	11.4
36%	1.09	5.8

Table 3. Accessible q-range of the Risø SANS spectrometer and corresponding minimal real space size given by $2\pi/q_{max}$.

Note the large difference between the in plane resolution given by Δq_R and Δq_A, and the rocking curve resolution, Δq_L, due to the ratio k/q. Since $k/q \gg 1$ the SANS spectrometer is optimized with respect to the longitudinal resolution.

An important specification of the SANS spectrometer is the accesible range in reciprocal space, as it puts a lower limit on the size of the structures that can be studied. As it is clear from the discussion of the velocity selector above, this depends on the chosen wavelength spread, and on the maximum number of rpm. Table 3 lists the maximal q which can be reached for the different bandwidth settings using the Risø SANS, together with the corresponding minimum real space periodicity.

Alignment of applied field and crystal orientation

One feature that has proved useful is the possibility of determining the misalignment between the crystal and the FLL, i.e. the applied field direction. This can be accomplished in the magnetically ordered borocarbides, since magnetic Bragg peaks exist at a sufficiently low q to be accessed by the SANS spectrometer. The misalignment was always found to be $\leq 4^o$.

Sample environments: Temperature and field

Two cryostats were used to study the FLL. Both were dedicated to SANS experiments and mounted with single crystal sapphire windows in vacuum and insulation shields, in order to reduce the small angle background, that would otherwise arise from passing the neutron beam through aluminum. The cryostats are shown in figure 16 and 17. Both cryostats hold a superconducting horizontal field magnet.

Figure 16. Picture showing the pumped cryostat including electronics used for FLL studies down to 1.5 K. The cryostat holds a superconducting horizontal field magnet which can produce fields up to 5 Tesla. In the right of the picture one sees the SANS detector tank.

Figure 17. Picture showing the dilution refrigerator including gas handling system and electronics used for FLL studies down to 50 mK. The cryostat holds a superconducting horizontal field magnet which can produce fields up to 2 Tesla.

4 FLL reflectivity measurements

A standard measurement, that was always performed during the experiments, was the determination of the field and temperature dependence of the FLL reflectivity. In $ErNi_2B_2C$ this was done by U. Yaron *et al.* [19]. Here I present measurements on YNi_2B_2C, $TmNi_2B_2C$, $LuNi_2B_2C$ and $Y_{0.75}Lu_{0.25}Ni_2B_2C$. Many of the results in this chapter were reported in refs. [27, 47, 48].

4.1 Experimental details

All measurements reported in this chapter were done with the applied field parallel to the crystalline c-axis, except if explicitly stated otherwise. All measurements of the FLL reflectivity were done following a field cooling. Background measurements were done after a zero field cooling.

4.2 Data analysis

Absolute intensity measurement

Determination of the penetration depth, λ, and the coherence length, ξ, require an absolute measurement of the scattered intensity. To faciliate this, a monitor counting a low fraction of the neutron beam is situated at the collimation section entrance. To relate the monitor count rate to the incident neutron flux on the sample, socalled direct beam measurements were performed. In these measurements the beam stop, which normally absorbs the unscattered beam, is removed, and a beam attenuator is inserted before the monitor to reduce the intensity and avoid damage to the detector. The monitor efficiency is defined by dividing the direct beam intensity by the monitor count. When performing measurements of the scattered intensity, the incident flux can be calculated from the monitor count. By measuring the direct beam intensity as described, the finite sample transmission is implicitly taken into account.

In the experiments on YNi_2B_2C and $LuNi_2B_2C$ reported below, the measured monitor efficiencies for different neutron wavelengths turned out to be inconsistent. Instead a constant attenuation factor was used. The origin of this discrepancy is still not resolved.

Integrated reflectivity

To determine the integrated reflectivity, the scattered intensity is measured at a number of discrete settings while rotating the sample, and hence rocking the (1,0) FLL Bragg peak through the Ewald sphere. The intensities are obtained at each angular position, by summing boxes centered at the peaks as shown in figure 18. An example of a typical rocking curve is shown in figure 19. The rocking curve intensities of the first order Bragg peaks are fitted to Lorentzians, corrected for their respective Lorentz factors as described in section 3.4, and finally averaged and divided by the incident flux to determine the integrated reflectivity, R. In the cases where the rocking curves are not fitted to satisfaction by a Lorentzian, the intensity is integrated numerically. If the scattered intensity is low with respect to the small angle background additional background scans are performed and subtracted.

4.3 Determining λ and ξ

Once the averaged, Lorentz factor corrected, absolute reflectivity for the (1,0) FLL Bragg reflections is found, it is possible to extract the form factor using equation (64)

$$|\boldsymbol{h}_{10}|^2 = R\,\frac{16\phi_0^2\,q}{2\pi\,\gamma^2\lambda_{\rm n}^2\,t}.$$

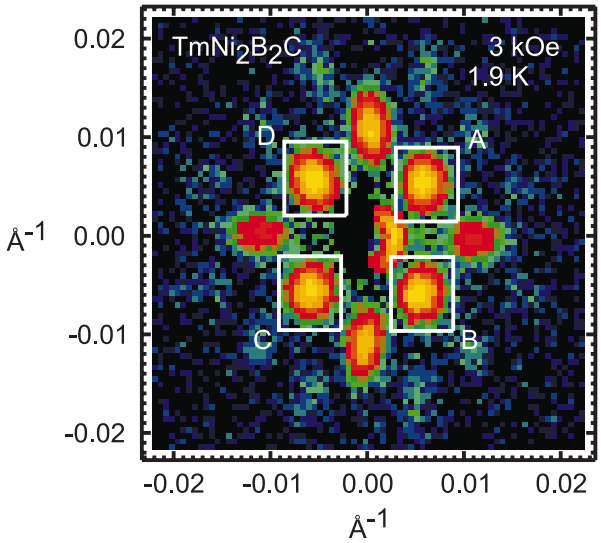

Figure 18. FLL diffraction pattern in $TmNi_2B_2C$ at $T = 1.9$ K and $H = 3$ kOe obtained by summing an entire rocking curve. The sample was rotated around the vertical axis. The intensities of the (1,0) reflections are determined at each angular setting, by summing the counts in the boxes centered at the the Bragg spots labelled A-D. The intensity is plotted on a logarithmic scale, showing several higher order reflections. The large radial smearing arise partly from to the wavelength spread ($\Delta\lambda_n/\lambda_n = 18\%$), and partly from an anisotropic beam divergence.

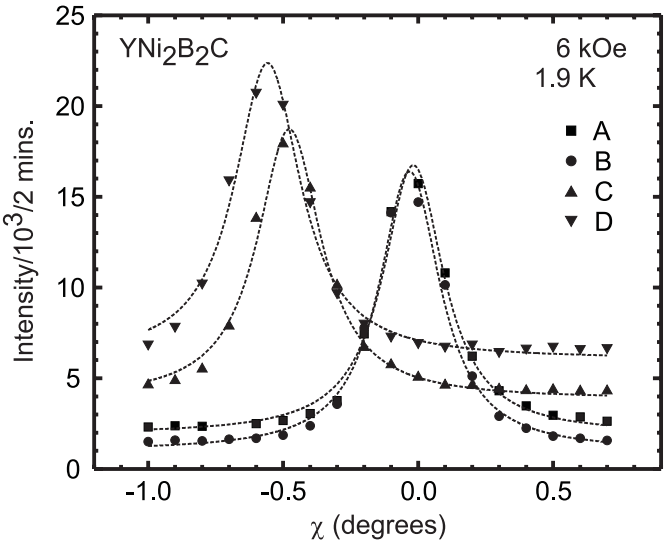

Figure 19. FLL rocking curves of the (1,0) reflections in YNi_2B_2C at $T = 1.9$ K and $H = 6$ kOe. The sample was rotated around the vertical axis, and the intensities are fitted to Lorentzians. No background subtraction was performed in this measurement. The labels A-D refer to the four different Bragg peaks, as shown in figure 18.

Using the model for the field dependence of the FLL form factor, described in section 3.2, equation (57)

$$|\boldsymbol{h}_{10}|^2 = \frac{\phi_0^2}{(2\pi\,\lambda)^4}\, e^{-4\pi^2 B\xi^2/\phi_0},$$

it is possible to extract λ and ξ. In this model a semi-log plot of the form factor versus field yields a straight line: $\ln|\boldsymbol{h}_{10}|^2 = \alpha B + \beta$. Plots of the form factor for YNi_2B_2C, $LuNi_2B_2C$ and $TmNi_2B_2C$ are shown in figure 20, together with linear fits to the data. In the case of YNi_2B_2C and $LuNi_2B_2C$ the data are well fitted by the model. For $TmNi_2B_2C$ on the other hand, the fit is very poor. This may be due to the susceptibility of the Tm ions and hence a large sublattice magnetization at temperatures above T_N [16]. The effect of susceptibility will discussed further in chapter 7.

From the fits of the form factor the penetration depth and coherence length are given by

$$\lambda = \frac{\sqrt{\phi_0}}{2\pi}\, e^{-\beta/4} \tag{74}$$

and

$$\xi = \frac{\sqrt{\phi_0}}{2\pi}\, \sqrt{-\alpha}. \tag{75}$$

The results for λ and ξ are listed in table 4, together with the results on $ErNi_2B_2C$ obtained by U. Yaron *et al.* [19]. The results are in fair agreement with the litterature as listed in chapter 1, table 1. Transport measurements on either pieces of the samples used for the SANS experiment or from the same growth yielded $H_{c2}(2.2\text{ K}) = 65$ kOe ($\xi = 71$ Å) for $LuNi_2B_2C$ and $H_{c2}(1.9\text{ K}) = 7.8$ kOe ($\xi = 206$ Å) for $TmNi_2B_2C$. The uncertainties listed in table 4 are based on the errors given by the fitting routine. However the true errors from thickness variations and flux inclusions in the samples, systematic errors, etc. are probably larger than this.

Doping studies

In addition to the "pure" compounds we also performed form factor measurements on $Y_{0.75}Lu_{0.25}Ni_2B_2C$. This is shown in figure 21. The results for λ and ξ are listed in table 4, and are consistent with the values for pure YNi_2B_2C and $LuNi_2B_2C$.

$\boldsymbol{B}$ vs. $\boldsymbol{H}$

In the determination of λ and ξ it was implicitly assumed that $B = H$. Using $B = (q/2\pi)^2\phi_0$, it is possible to deduce B from the magnitude of the scattering

Material	λ (Å)	ξ (Å)	κ	H_{c1} (G)	H_{c2} (kG)
YNi_2B_2C	1018 ± 21	91 ± 2	11.2 ± 0.2	384	40
$ErNi_2B_2C$	500	135	3.7	862	18
$TmNi_2B_2C$	613 ± 58	132 ± 21	4.6 ± 0.7	1006	19
$LuNi_2B_2C$	1061 ± 30	82 ± 2	12.9 ± 0.4	374	49
$Y_{0.75}Lu_{0.25}Ni_2B_2C$	1070 ± 19	90 ± 1	11.9 ± 0.2	356	41

Table 4. Penetration depth and coherence length determined from FLL form factor measurements. Using the GL expressions (10), (16) and (17) the GL-parameter, and the upper and lower critical fields are calculated. The results for $ErNi_2B_2C$ were obtained by U. Yaron et al. [19].

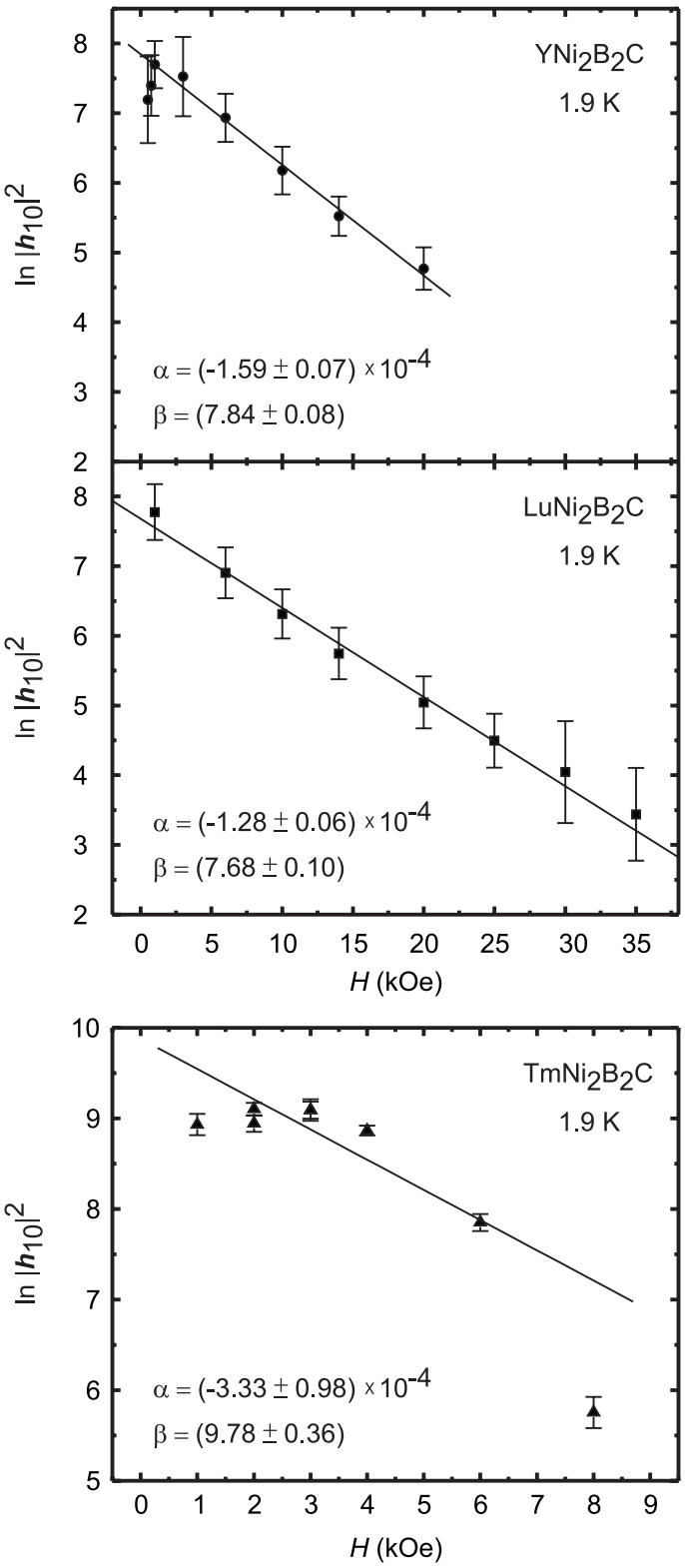

Figure 20. Semi-log plot of the field dependence of the FLL form factor in YNi_2B_2C (top), $LuNi_2B_2C$ (middle) and $TmNi_2B_2C$ (bottom) at $T = 1.9$ K. The fits are to a straight line with slope α, and zero field intercept β.

vectors. A comparison between B and the applied field H is shown in figure 22 for both non-magnetic YNi_2B_2C and magnetic $TmNi_2B_2C$. In the case of YNi_2B_2C the ration B/H is close to one, whereas for $TmNi_2B_2C$ one finds $B/H \approx 1.12$.

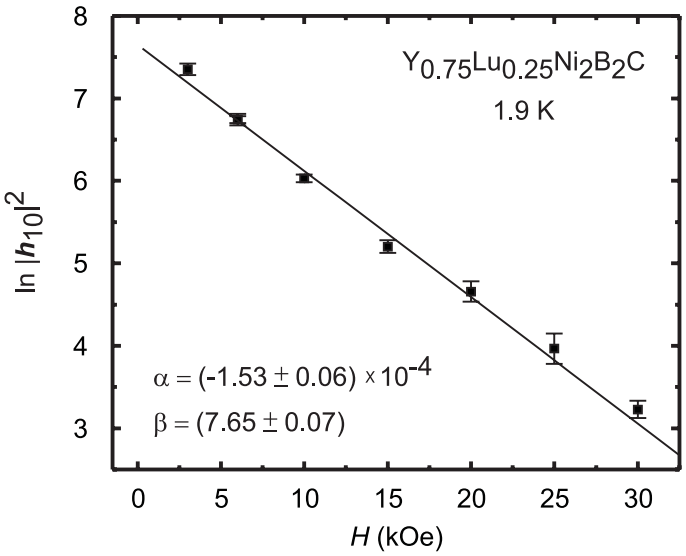

Figure 21. Semi-log plot of the field dependence of the FLL form factor in $Y_{0.75}Lu_{0.25}Ni_2B_2C$ at $T = 1.9$ K.

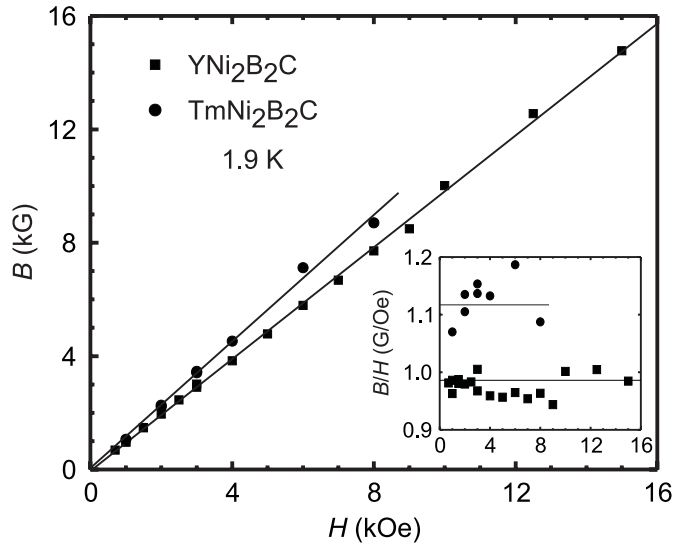

Figure 22. B versus H in YNi_2B_2C and $TmNi_2B_2C$. In both cases the temperature was 1.9 K. The measurement on YNi_2B_2C was obtained with the field rotated 30° around the [110] direction away from the c-axis. The slight difference in slope is either due to the susceptibility of $TmNi_2B_2C$ or to a small misalignment of the velocity selector. Inset shows the ratio B/H versus H.

The increased ratio for $TmNi_2B_2C$ may be due to the magnetization of the Tm ions as discussed above, or it may arise from a slight misalignment of the velocity selector. The reason that B/H is close to unity close to (and below) the nominal H_{c1}, is due to the platelike sample geometry giving rise to a large demagnitization factor.

4.4 Temperature dependence of the reflectivity

The field dependence of the integrated reflectivity is determined by the field dependence of the penetration depth, $R \propto 1/(\lambda(T))^4$, using the London limit of the form factor. In the GL-theory the field dependence is given by $\lambda^2 \propto (1 - T/T_c)^{-1}$. This means that the square root of the integrated reflectivity should be linear

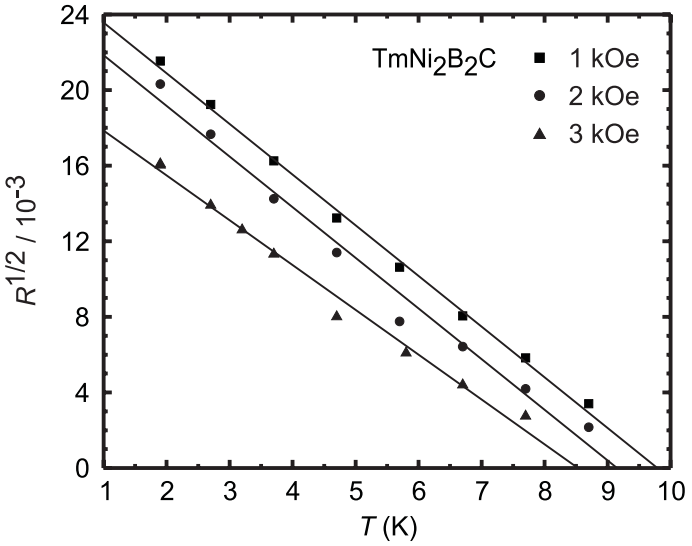

Figure 23. Temperature dependence of the square root of the integrated FLL reflectivity for $TmNi_2B_2C$. This follows the linear mean field temperature dependence. The transition temperatures found from the linear fits are $T_c = 9.8$ K (1 kOe), 9.1 K (2 kOe) and 8.5 K (3 kOe).

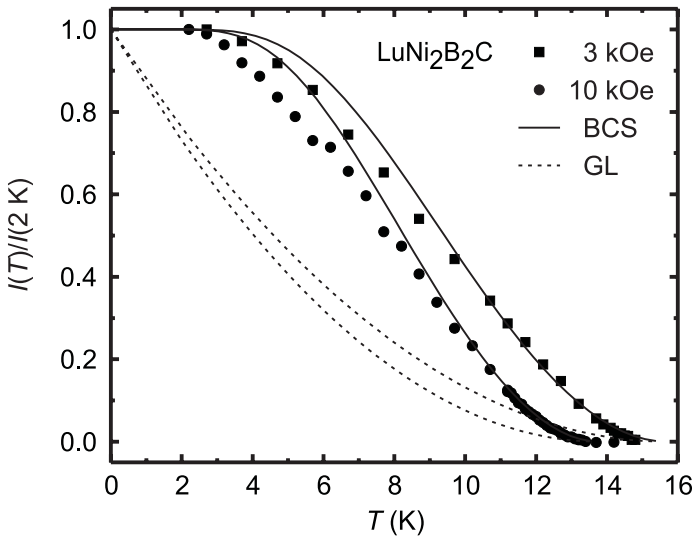

Figure 24. Temperature dependence of the peak intensity of the (1,0) FLL reflection for $LuNi_2B_2C$. The solid lines are calculated from the BCS theory [49], corresponding to $T_c = 15.7$ K (3 kOe) and 13.8 K (10 kOe). The dashed lines are using the GL temperature dependence.

close to T_c for low values of B/H_{c2}. In figure 23 the temperature dependence of $\sqrt{R}$ for $TmNi_2B_2C$ is shown for three different fields. This is linear down to 2 K, well below T_c. Similar results were found for $ErNi_2B_2C$ by U. Yaron *et al.* [19]. Below 2 K the reflectivity in $TmNi_2B_2C$ is strongly influenced by the magnetic ordering, which is the subject of chapter 7.

The temperature dependence of the scattered intensity was also measured in $LuNi_2B_2C$. However only the peak intensities, and not the integrated intensities, were measured. In figure 24 the peak intensity normalized to $I(2K)$ is shown for two different fields. The measured temperature dependence in this compound follows the predictions of the BCS calculated by B. Mühlschlegel [49] rather than the GL theory.

5 Low field FLL symmetry transition

One of the principal findings in the first SANS study of $ErNi_2B_2C$ was a square FLL [19]. The square FLL was seen in the entire measured field and temperature range (2 kOe $< H <$ 12 kOe, 1.6 K $< T <$ 8.0 K). Low field ($H = 100$ Oe) decoration experiments on the other hand revealed a hexagonal FLL. It was therefore clear that a hexagonal to square symmetry transition had to occur in the field range 100 Oe - 2 kOe in $ErNi_2B_2C$. Several experiments were performed to study this low field symmetry transition, and the results are reported in this chapter. The hexagonal to square FLL symmetry transition has until now been observed in YNi_2B_2C, $ErNi_2B_2C$, $TmNi_2B_2C$ and $LuNi_2B_2C$. Most of the results in this chapter are published in refs. [27, 47, 48, 50, 51].

Previous observations of FLL symmetry transformations were limited to the marginal type II superconductor niobium in the intermediate mixed state, where a field independent transformation from a distorted hexagonal to a square lattice was seen by lowering the temperature [52, 53], and to the heavy fermion superconductor UPt_3 where small distortions of the FLL were seen as a function of field [54].

5.1 Experimental details

All measurements reported in this chapter were done on $ErNi_2B_2C$ with the applied field parallel to the crystalline c-axis, except if explicitly stated otherwise. All measurements of the FLL were done following a field cooling. Background measurements were done after a zero field cooling.

5.2 Data analysis

In the ideal experimental setup the FLL symmetry is directly observed from the diffraction pattern imaged by the SANS position sensitive detector. The position of the Bragg peaks determines the scattering vectors, allowing the FLL orientation, symmetry and possible distortion to be calculated, using the analysis from section 2.2. However, for $\boldsymbol{H} \parallel \hat{\boldsymbol{c}}$ the FLL symmetry transition occur at relatively low fields ($H < 1$ kOe), and hence at short scattering vectors, and it is therefore obscured by the coarse in-plane resolution of the SANS spectrometer. A more elaborate analysis was therefore necessary to study the details of the symmetry transition.

Radial analysis

The objective of this analysis was to determine the magnitude of the scattering vector, defined as the maximun scattered intensity, for different directions within the scattering plane. Since the FLL rocking curve widths in $ErNi_2B_2C$ are broad in comparison with the beam divergence and the small scattering angles (see chapter 6), both the (1,0) and the (1,1) peaks essentially satisfy the Bragg condition, if the sample is centered relative to all four first order reflections. In this way it is possible to measure an entire diffraction pattern using a single angular setting. The radial intensity distribution was sampled at evenly spaced points on the detector, along the square FLL high symmetry directions, as shown in figure 25. The distance between the sampling positions was approximately one pixel, and linear interpolation to the four nearest neighbours was used. Since, for $\boldsymbol{H} \parallel \hat{\boldsymbol{c}}$, the FLL diffraction pattern is always four fold symmetric, the radial intensity was averaged

over the four equivalent directions shown in figure 25. An example of the radial intensity distribution is shown in figure 26.

Simulated $\theta - 2\theta$ scans

A more time consuming approach to determine the scattering vector is by simulating a $\theta - 2\theta$ scan, corresponding to a longitudinal scan on a standard two axis spectrometer. For this a full rocking curve has to be measured, as described in chapter 4. The diffraction patterns for the different angular settings are kept as individual frames, and the two-dimensional interpolation used in the simple radial analysis is extended into the third dimension spanned by the sequence of frames.

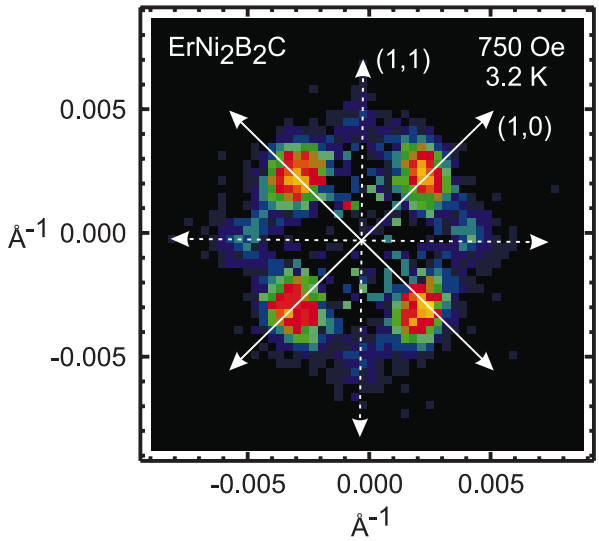

Figure 25. Example of FLL diffraction pattern for $ErNi_2B_2C$ at $T = 3.2$ K and $H = 750$ Oe. The arrows show the directions for radial intensity sampling, labelled by the FLL Bragg reflections that they cut.

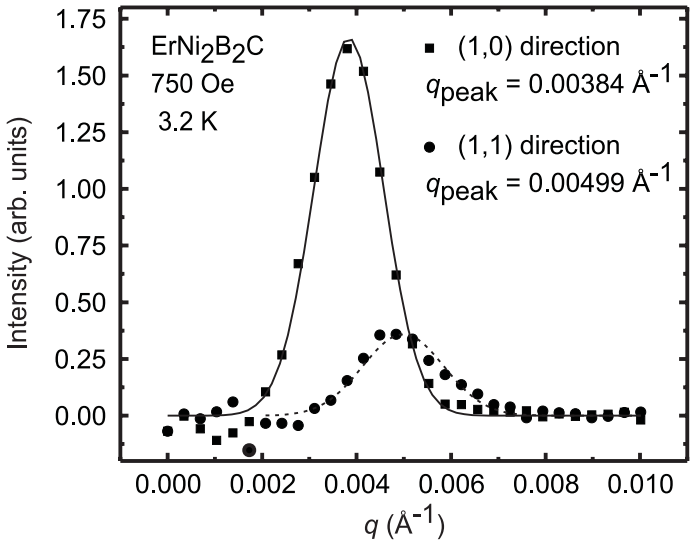

Figure 26. FLL radial intensity distribution in $ErNi_2B_2C$ in the directions of the (1,0) and (1,1) Bragg reflections, for the diffraction pattern shown in figure 25. The intensities for both the (1,0) and the (1,1) peaks are averaged over the four equivalent directions. The intensities are fitted to Gaussians shown by the lines and with maxima listed in the plot.

In this way the intensity is sampled in the interpolated frame with angular setting θ, corresponding to the scattering angle $2\theta = q\lambda_n/2\pi$. This analysis provided results consistent with the simple radial analysis.

Azimuthal analysis

Equivalent to the radial intensity analysis, an azimuthal intensity analysis for a fixed magnitude of the scattering vector was performed on a small part of the data set. The azimuthal analysis is described in detail in chapter 7.

5.3 Results

Figure 27 shows three FLL diffraction patterns, obtained with an applied field of respectively 1000 Oe, 750 Oe and 500 Oe. In the top panel (1000 Oe) the FLL is clearly square and aligned with the [110] crystalline direction. In addition to the (1,0) peaks the well ordered FLL shows strong (1,1) reflections. As the field is reduced, two effects are obvious. The first is the reduction in scattering vector due to the field dependence of the flux line density. The second effect is the azimuthal broadening of the (1,0) peaks, most pronounced in the bottom panel. In contrast to the azimuthal width, the radial width remains roughly constant and resolution limited as the field is reduced. The azimuthal broadening cannot be explained by a simple disordering of the FLL, which would lead to an isotropic broadening in the plane of the detector, but is the harbinger of the hexagonal to square symmetry transition.

To verify that the low field FLL is indeed hexagonal, magnetic decoration experiments, wherein iron particles are evaporated onto the sample surface at low temperatures [55], were performed. The particles preferentially decorate regions where the flux lines exit the sample, and a SEM is used to image the particles, and hence the flux line, locations. Figure 28 shows real space and Fourier transform images of a magnetic decoration pattern on YNi_2B_2C for an applied field of 40 Oe. The single domain hexagonal lattice is aligned with either the [100] or the [010] directions. In general the FLL is divided into domains pinned to one of the two equivalent crystallographic directions.

Figures 29 and 30 show the results of the detailed analysis of the SANS data. In figure 29 the field dependence of the radial position of both the square (1,0) and (1,1) FLL peaks are shown. The magnitudes of the scattering vectors for the Bragg peaks are normalized by $q_0 = 2\pi(B/\phi_0)^{1/2}$. Using this normalization the (1,0) square lattice peaks are at $q/q_0 = 1$ and the (1,1) peaks are at $\sqrt{2}$. For a hexagonal lattice, the (1,0) peaks are at $(2/\sqrt{3})^{1/2} = 1.07$. The data approaches the square lattice values above 1 kOe. As the field is reduced the square lattice (1,1) peaks move in and (1,0) peaks move out, forming the (1,0) peaks for the hexagonal lattice.

Figure 30 shows the azimuthal width of the (1,0) peaks of the square lattice. As the field is reduced below 600 Oe, the peaks broaden substantially above the calculated experimental resolution. The limited resolution of the SANS experiment obscures the twelve peaks of the two hexagonal domains at low fields, leaving only a modulated ring of scattering as the azimuthal width increases.

The results in figures 29 and 30 suggest that the distortion from a hexagonal to a square FLL occurs smoothly over the range from 350 to 1500 Oe. Since the monodomain square lattice is aligned with the [110] direction of the host crystal, while the hexagonal lattice has domains aligned along [100] and [010], the transformation must proceed via a rhombohedral distortion along the [100] axis. In addition the transformation must be area preserving due to flux quantization. The progression of the hexagonal to square FLL transition is sketched in figure

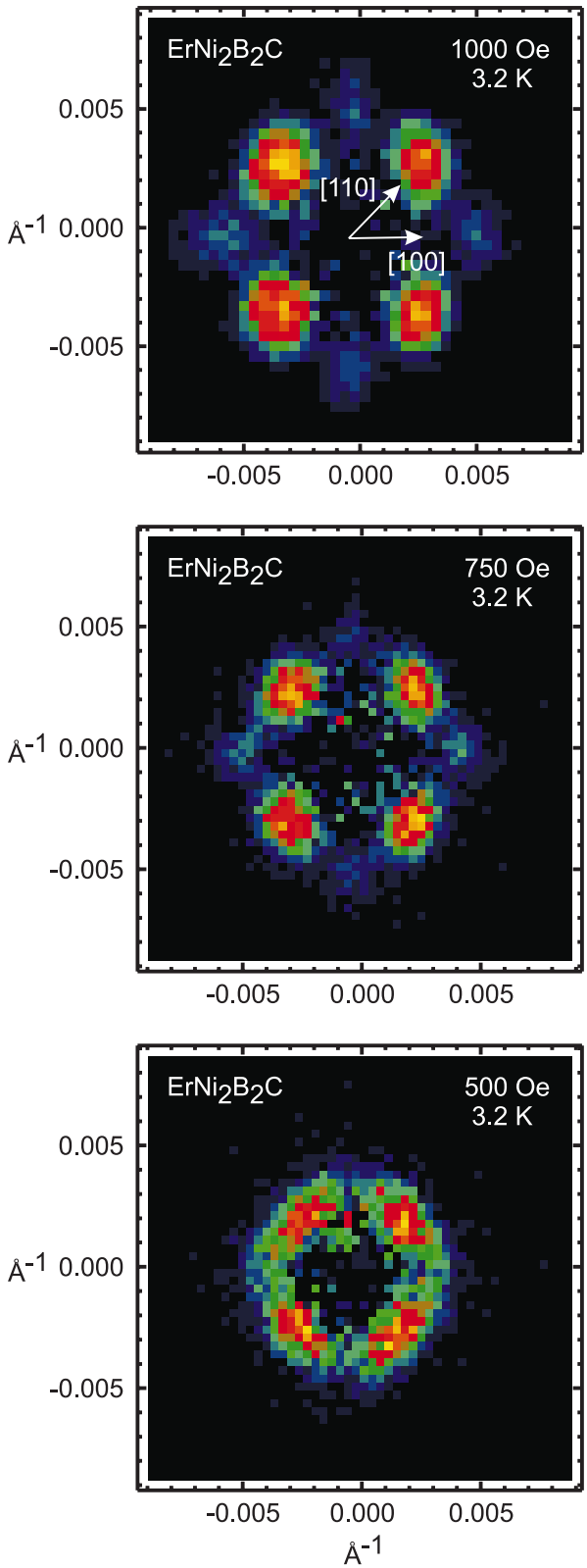

Figure 27. FLL diffraction patterns for $ErNi_2B_2C$ at 1000 Oe (top), 750 Oe (middle) and 500 Oe (bottom) and $T = 3.2$ K. The orientation with respect to the crystalline axis is shown in the top and is identical for all three fields. The diffraction patterns were obtained using a single crystal orientation, centered with respect to the first order FLL reflections.

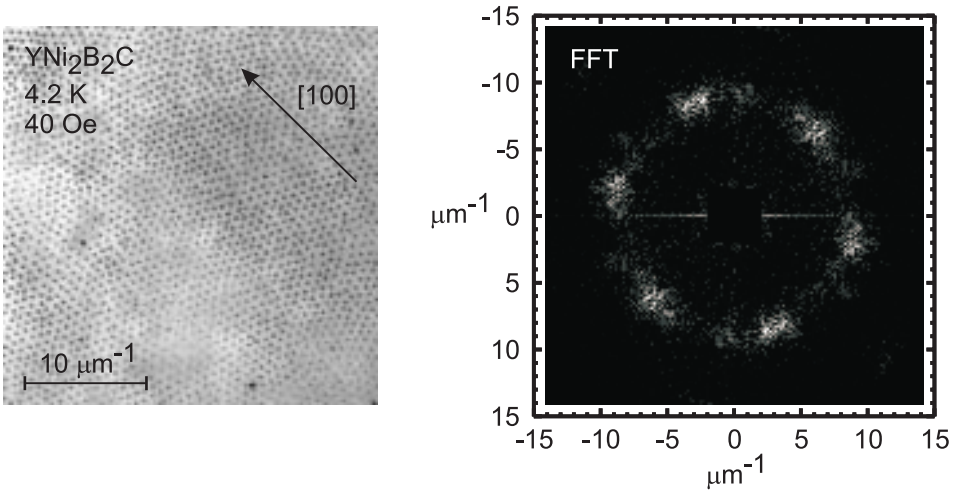

Figure 28. FLL decoration pattern in YNi_2B_2C at 4.2 K and 40 Oe (left) and it's Fourier transform (right). The decoration shows a monodomain hexagonal FLL pinned to the crystalline [100] direction.

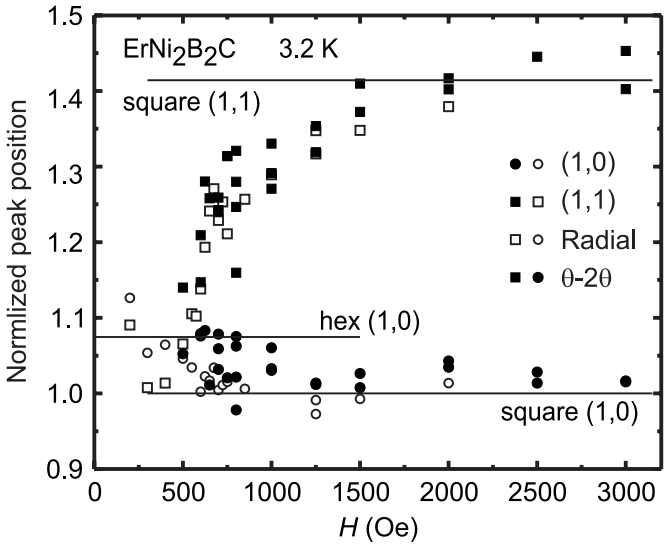

Figure 29. Hexagonal to square symmetry transition in $ErNi_2B_2C$ at $T = 3.2$ K. The normalized peak position, q/q_0, is shown versus field. Open symbols are from the simple radial analysis and solid symbols are from the $\theta - 2\theta$ analysis. Circles and squares represent positions of the square (1,0) and (1,1) peaks respectively.

31. The reciprocal space pattern is shown for an equal distribution of domains aligned along respectively [100] and [010]. The two domains of the hexagonal lattice produce twelve equally spaced peaks. The square lattice produce the four (1,0) peaks and the four (1,1) peaks found at high fields. The arrows show how the position of the peaks changes as the field is lowered. Each of the four square lattice (1,0) peaks split azimuthally, moving out slightly to form eight of the twelve peaks for the hexagonal lattice. This splitting is what is seen as the azimuthal broadening in figure 30. The square lattice (1,1) peaks also split but in the radial direction. Four peaks move in to make a total of twelve hexagonal lattice peaks, and four peaks move out to form higher order peaks for the hexagonal lattice. However, due to the rapidly decreasing scattering intensity as a function of q, the higher order peaks are not observed. This decrease in intensity also gives rise to the reduced intensity in the diffraction pattern at 500 Oe in figure 27, in the direction of the square lattice (1,1) peaks.

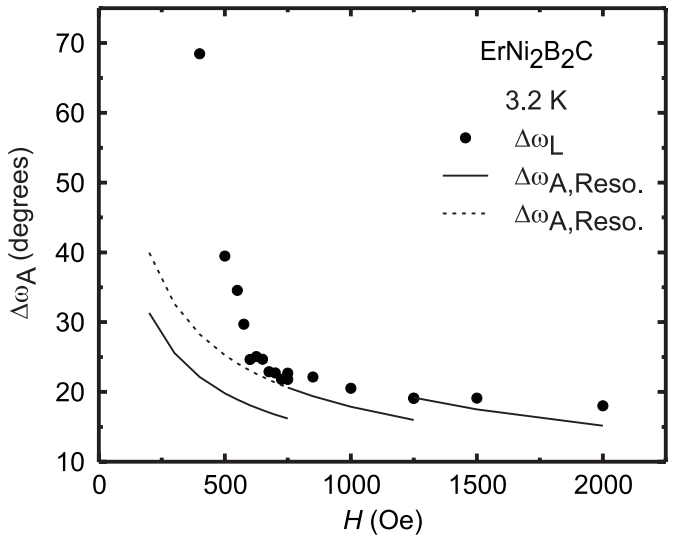

Figure 30. Azimuthal widths of the square FLL (1,0) peaks versus field for $ErNi_2B_2C$ at $T = 3.2$ K. The solid line is the calculated experimental resolution, where the jumps are due changes of the neutron wavelength, λ_n. The dashed line is an extension of the middle wavelength resolution.

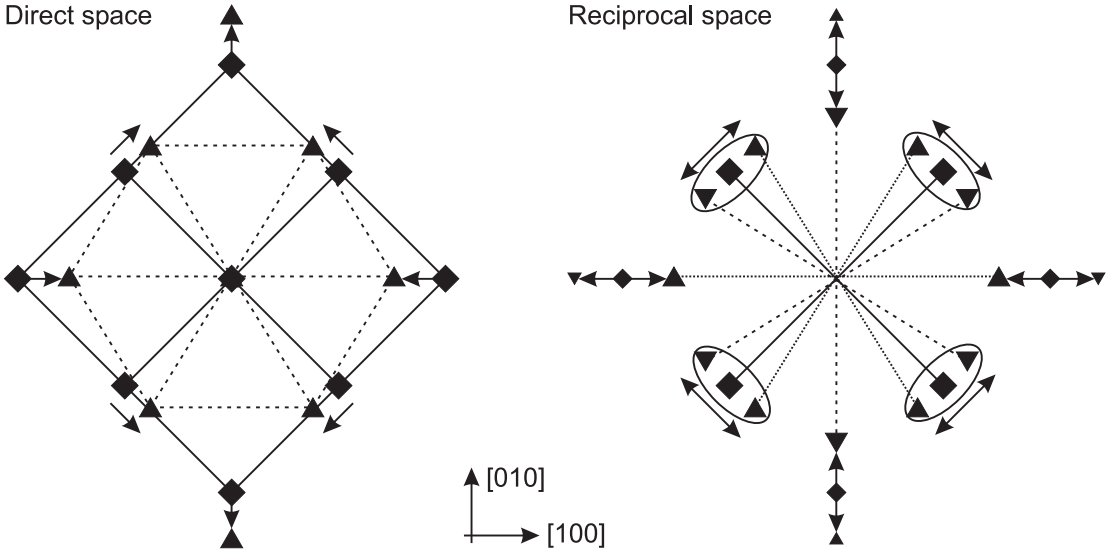

Figure 31. Schematic diagrams showing the rhombohedral FLL symmetry transition in real space (left) and in reciprocal space (right). Hexagonal lattice points are indicated by the triangles and square lattice points by the squares. The azimuthally broadened SANS peaks result from overlap of the circled peaks, shown on the right. Only one of the two equivalent hexagonal domains are shown is the real space picture.

5.4 Discussion

In strong type-II superconductors the FLL is typically found to be hexagonal. The principal question that arise is thus what drives the FLL to be square in the majority of the phase diagram in the borocarbides. A model explaining both the square FLL and the low field transition to a hexagonal symmetry was presented by V. G. Kogan *et al.* [56] and is described below.

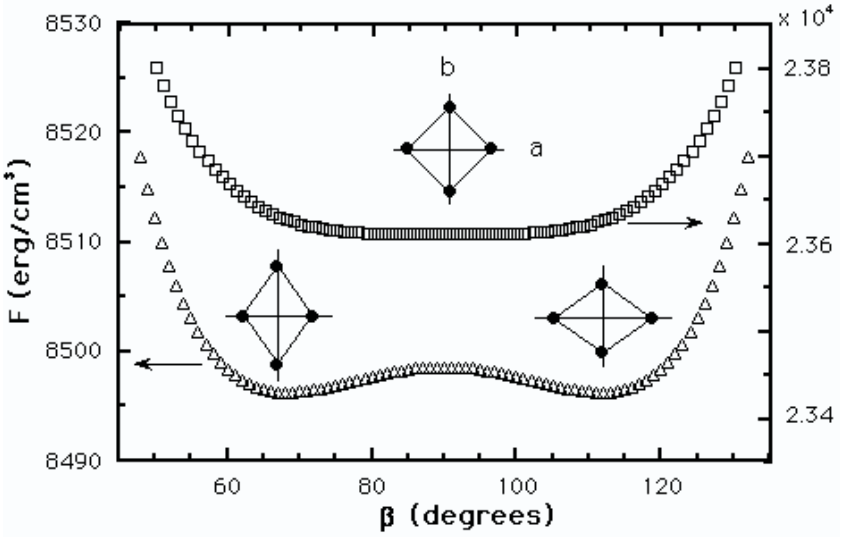

Figure 32. Free energy of the FLL versus apex angle β for 200 G (lower curve) and 500 G (upper curve). Figure is from V. G. Kogan et al. *[56]. Used with permission.*

Model of square to hexagonal FLL symmetry transition

The square FLL and the low field transition to hexagonal symmetry can be explained by a model using non-local corrections to the London model, and taking into account the basal plane four fold anistropy of the Fermi surface of the borocarbides [56]. Within this model the square FLL is stabilized when the screening currents around one flux line extends so far into the field distribution of the neighbours, that the four fold anisotropy is significant within the range of the non-local electrodynamics given by the superconducting coherence length, ξ [57]. The onset of the square to hexagonal symmetry transition occur when the field is reduced, and the overlap of neighbouring flux lines is reduced. The symmetry transition is continous and a hexagonal FLL is only approached in the zero field limit. The Fermi surface anisotropy is also responsible for locking the FLL with repect to the crystalline axes with the square FLL is oriented along the [110] direction and the hexagonal FLL along [100].

The results of the calculations by V. G. Kogan *et al.* is shown in figures 32 to 34. The results are based on band structure calculations for $LuNi_2B_2C$. Figure 32 shows the free energy as a function of apex angle for two different fields. It shows a minimum at 90° i.e. a stable square FLL at the higher field (500 G), and two minima corresponding to equivalent rhombic configurations at the lower field (200 G). Hexagonal symmetry is reached when the minima occurs at apex angles equal to respectively 60° and 120°.

Shown in figure 33 is the apex angle as a function of field for two different field orientations. Looking first at $\boldsymbol{H} \parallel \hat{\boldsymbol{c}}$ and starting from the high field side, one finds that the square FLL is stable for fields $H > H_2$ where $H_2 \approx 480$ G. Reducing the field below H_2 the square FLL undergoes a rhombohedral distortion along [100] shown by the diamonds. At fields below $H_1 \approx 200$ G this FLL orientation becomes unstable (shown by crosses) and the FLL undergoes a 45° reorientation shown by the down triangles (and plusses above H_1). The reorientation is a first order transition. One notes that the FLL only approach the true hexagonal symmetry in the limit of zero field. Turning to $\boldsymbol{H} \parallel \hat{\boldsymbol{a}}$ shown by up triangles one finds that the onset of the square to hexagonal transition is shifted to higer fields, and there is no reorientation transition. Furthermore the FLL is distorted by the penetration depth anisotropy in the plane perpendicular to the flux lines.

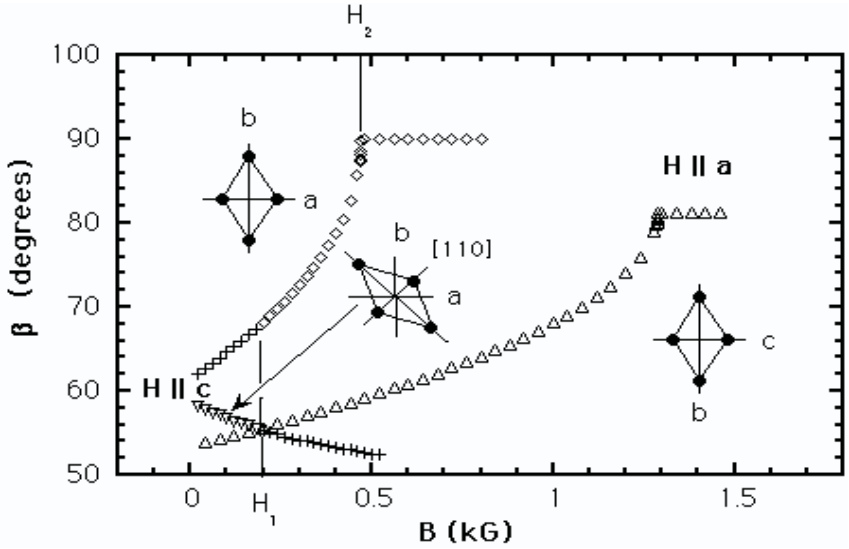

Figure 33. Apex angle β versus field for two different field orientations. The two curves on the left are for $\boldsymbol{H} \parallel \hat{\boldsymbol{c}}$, and the curve on the right is for $\boldsymbol{H} \parallel \hat{\boldsymbol{a}}$. Figure is from V. G. Kogan et al. *[56]. Used with permission.*

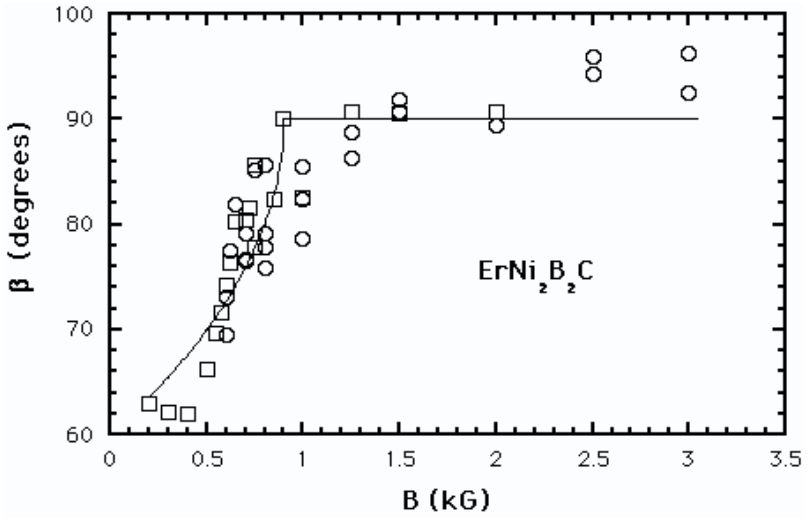

Figure 34. Comparison between calculated square to hexagonal FLL symmetry transition assuming $H_2 = 900$ G and $ErNi_2B_2C$ experimental data from figure 29. Figure is from V. G. Kogan et al. *[56]. Used with permission.*

Ignoring the fact that the the above results were obtained using band structure calculations for $LuNi_2B_2C$, it is possible to superpose the calculated square to hexagonal symmetry transition for $\boldsymbol{H} \parallel \hat{\boldsymbol{c}}$ onto the experimental data for $ErNi_2B_2C$ assuming a transition field $H_2 = 900$ G. This is shown in figure 34. One finds a reasonable agreement between the calculation and the data.

Experimental observation for the reorientation in YNi_2B_2C using SANS was recently reported by D. McK. Paul *et al.* [26]. They found a transition field $H_1 = 1.25$ kG. This is much higher than predicted and in disagreement with the results presented in this thesis, where the FLL is found the be square down to 1 kG. The reason for this discrepancy is not known, but may be related to sample purity which can shift H_2 as will be shown in the following.

Additional evidence for the low field reorientation transition was found by Bitter decorations on $TmNi_2B_2C$ by A. B. Abrahamsen *et al.* [58].

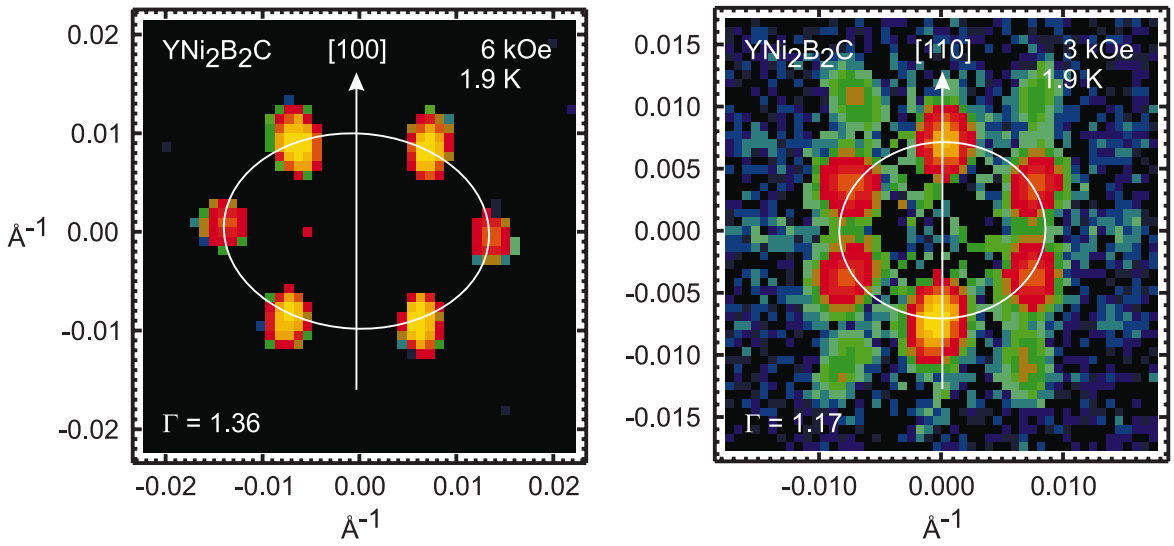

Figure 35. FLL diffraction patterns for YNi_2B_2C at $T = 1.9$ K. The diffraction patterns were obtained with the field rotated 30° around the vertical axis, which were along [100] (left) and [110] (right). The applied field was respectively 6 kOe and 3 kOe. The diffraction patterns were obtained by summing an entire rocking curve. The FLL distortions, Γ, are listed in the plots and indicated by the ellipses.

Additional theory

Using GL theory and adding terms to break the circular symmetry, Y. De Wilde *et al.* and K. Park and D. A. Huse was also able to demonstrate the stability of the square FLL close to H_{c2} [59, 60]. The results are related to an in-plane anisotropy of H_{c2}, with the FLL orientation depending on the sign of the anisotropy term. In-plane magnetization measurements of H_{c2} in $LuNi_2B_2C$ by V. Metlushko *et al.* found a 10% anisotropy at low temperatures, vanishing at T_c [61]. Transport measurements of the H_{c2} anisotropy in $ErNi_2B_2C$ reported by P. L. Gammel *et al.* also show a strong temperature dependence, including a sign change at the magnetic transition, $T_N = 6.8$ K [62]. This suggests a possible destabilization and reorientation of the square FLL in $ErNi_2B_2C$ at T_N for fields close to H_{c2}.

5.5 Supplementary results

In order to gain further insight and to test the proposed model describing the FLL symmetry transition, additional studies were carried out using different field orientations and doped materials.

Rotated field

To study the penetration depth anisotropy both within the *ab*-plane and between the *ab*-plane and the *c*-axis, experiments were performed on the FLL in YNi_2B_2C, with the applied field rotated 30° away from the *c*-axis. The effects of rotating the field around both [100] and [110] were studied.

Figure 35 shows FLL diffraction patterns for the two different axes of rotation. In both cases the FLL is distorted hexagonal, due to the penetration depth anisotropy in the plane perpendicular to the flux lines, cf. section 2.2. The distortion for the two axes of rotation are $\Gamma_{100} = 1.36$ and $\Gamma_{100} = 1.17$. The difference in the FLL distortion is due to the difference in the penetration depth along respectively [100] and [110]. Likewise the FLL orientations differ, since it is in both cases aligned

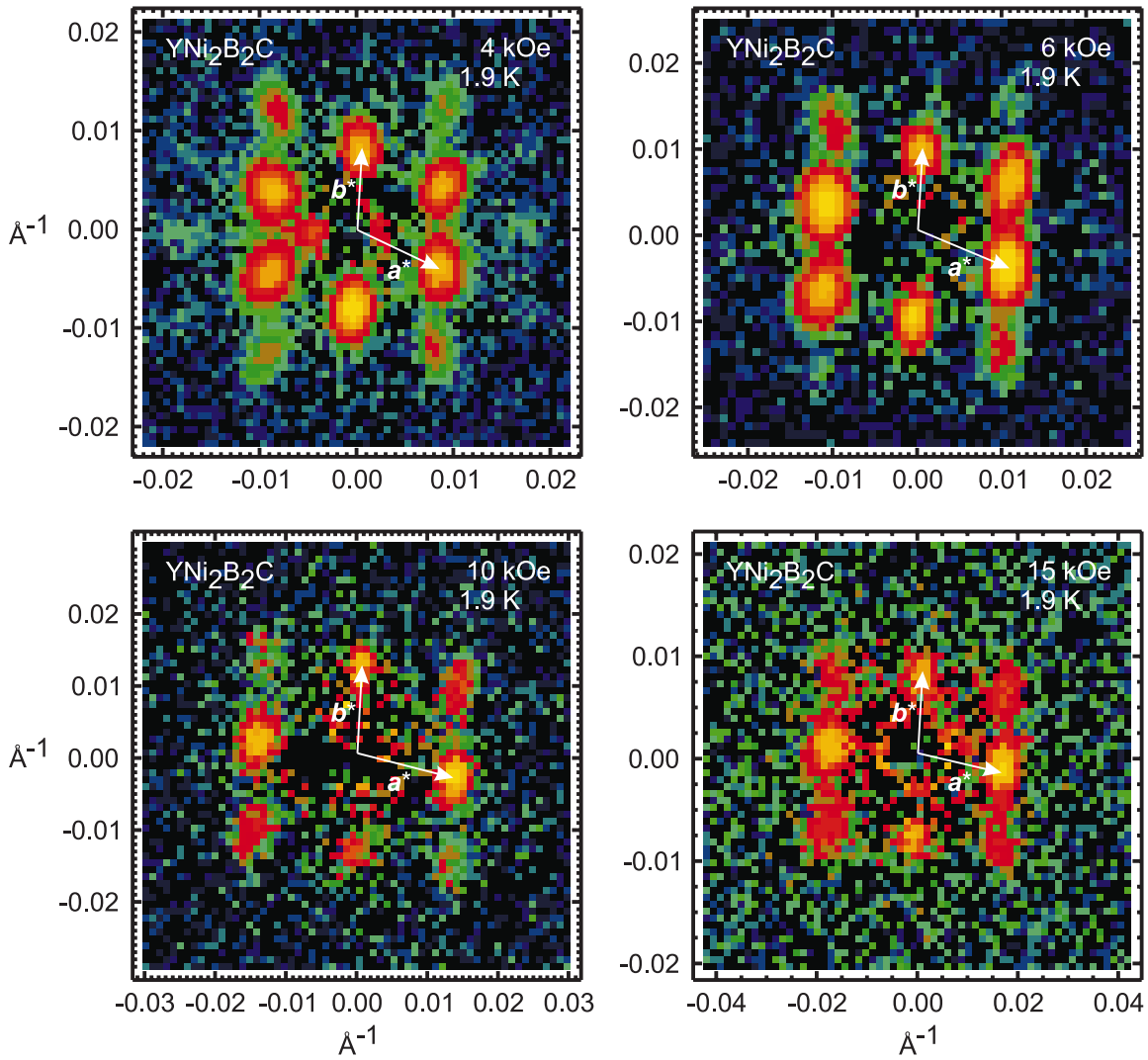

Figure 36. FLL diffraction patterns for YNi_2B_2C at T= 1.9 K with the applied field rotated 30º around the [110] axis, showing the progression of the hexagonal to square symmetry transition. Also shown is the FLL scattering vectors $\boldsymbol{a}^*$ and $\boldsymbol{b}^*$. The diffraction patterns were obtained by summing an entire rocking curve.

by the axis of rotation. This FLL alignment breaks the two-fold degeneracy, and leads to a single hexagonal domain.

The difference between the two axes of rotation is also reflected in the hexagonal to square symmetry transition. Rotating the field around [100] stabilize a hexagonal FLL up to the highest measured field of 30 kOe.

Rotating around [110] shifts the onset of the symmetry transition up to $\sim$ 4 kOe, in comparison to $\sim$ 500 Oe with $\boldsymbol{H} \parallel \hat{\boldsymbol{c}}$ in $ErNi_2B_2C$. The progression of the FLL transition from a distorted hexagon to a distorted square is shown in figure 36. Since the square FLL, like the hexagonal, is aligned with the [110] direction, the transition must proceed through a shear distortion, in stead of the rhombic distortion seen with $\boldsymbol{H} \parallel \hat{\boldsymbol{c}}$. The FLL scattering vectors are easily determined from the positions of the Bragg spots in the diffraction patterns, as shown in figure 36. Applying the analysis described in section 2.2, allows determination of the FLL orientation, symmetry and distortion. The results of this analysis are shown in figure 37. Values of the normalized opening angle, $\Delta\varphi$, equal to 90º and 120º correspond to a square and a hexagonal FLL, respectively. The FLL stays hexagonal up to $\sim$ 4 kOe, where a slow transtion towards a square starts. The

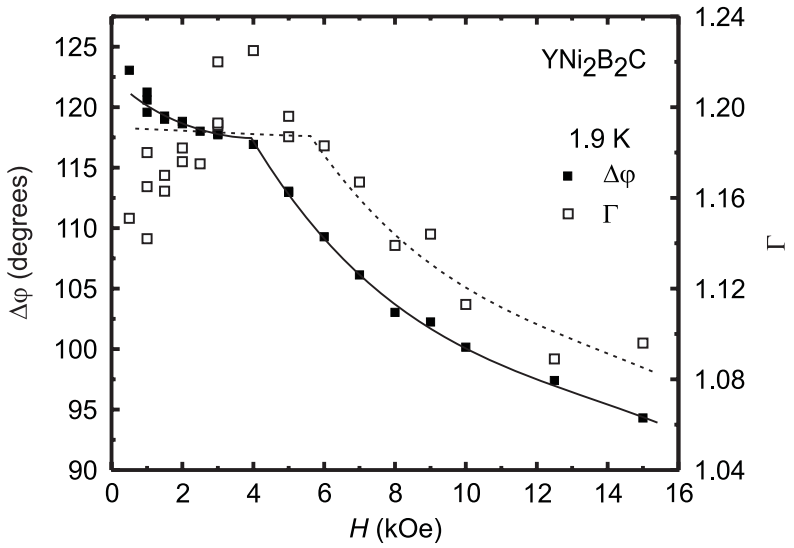

Figure 37. Normalized opening angle, $\Delta\varphi$, and FLL anisotropy, Γ, versus field for YNi_2B_2C at $T = 1.9$ K, with the applied field rotated 30° around the [110] axis. The lines are guides to the eye.

transition spans a wide field range, continuing above the maximum measured field of 15 kOe. The FLL distortion shows roughly the same field dependence as $\Delta\varphi$.

The upwards shift of the FLL symmetry transition, induced by rotating the field away from the *c*-axis is in qualitative agreement with the theoretical predictions by V. G. Kogan *et al.* [56].

The results for rotated fields elucidate the fourfold *ab*-plane anisotropy responsible for the high field square FLL.

Co-doped $LuNi_2B_2C$

As described in section 5.4 the square FLL is stabilized by the "square" flux lines and non-local electrodynamics [56]. The range of the non-locality is given by the effective coherence length, ξ, depending on the BCS zero temperature coherence length, ξ_0, and the electronic mean free path, l [57]. These quantities are related by the well known expression

$$\frac{1}{\xi} = \frac{1}{\xi_0} + \frac{1}{l}.$$

Adding impurities has the potential to decrease the mean free path and thereby ξ, without changing the details of the band structure significantly. Such a reduction of the range of the non-local interactions would shift the onset of the square to hexagonal symmetry transition to higher field more accesible to a SANS experiment.

This idea was pursued in studies of the FLL in $Lu(Ni_{1-x}Co_x)_2B_2C$ at a number of different cobalt dopings in the range $x = 1.5 - 9\%$. Using transport and magnetization measurements to extract values for ξ_0 and l, K. O. Cheon *et al.* confirmed that the ratio ξ_0/l was reduced with increased doping [63]. Inserting their results into the Kogan model they could calculate the expected onset field for the square to hexagonal symmetry transition. For doping levels $x = 1.5, 4.5, 6.0$ and 9.0% the predicted transition fields were respectively $H_2 = 3.4, 10.5, 15.3$ and 25.4 kOe.

The results of SANS experiments on the same samples are shown in figure 38. The data in the figure results from a combination of two different measurement schemes. When the azimuthal split was clearly resolved, the measurements were performed at a constant neutron wavelength. When the split could not be resolved,

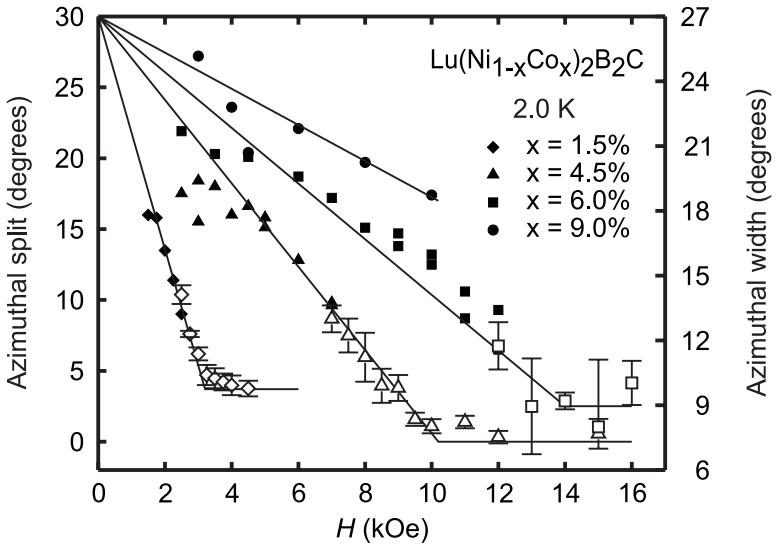

Figure 38. Azimuthal split between the two domains of rhombic FLLs in $Lu(Ni_{1-x}Co_x)_2B_2C$ versus field at $T = 2.0$ K. Data for four different doping levels are shown. The left hand ordinate shows the split (filled symbols) and the right hand ordinate shows the azimuthal broadening (open symbols). The two ordinates are calibrated using the regime of overlap. The lines are linear fits to the data.

measurements of the azimuthal width were performed keeping the scattering angle and hence the experimental resolution function constant. This was done by changing the wavelenth and the applied field in concert to keep $2\theta = q\lambda_n/2\pi$ constant. In this way the widths at different fields can be compared directly, and the onset of the transition is equivalent to the onset of azimuthal broadening. Examining the results in figure 38 a number of points can be concluded. First the onset of the transition clearly moves to higher fields with increased doping. Second the data extrapolates to a hexagonal symmetry only in the zero field limit. This is in qualitative agreement with the model. Finally, extracting the transition onset fields from the linear fits to the data one gets $H_2 = 3.2, 10.2, 14.0$ and 22.4 kOe, in excellent quantitative agreement with the predictions listed above.

5.6 Summary

In summary, the FLL undergoes a field driven hexagonal to square symmetry transition. We find that the high field, square flux lattice is monodomain and aligned with the [110] direction of the crystal. Below roughly 500 Oe this gives way to a hexagonal lattice with two domains which are aligned with the [100] and [010] directions. Rotating the field away from the c-axis shifts the transition to higher fields, as does doping. This is in agreement with a theoretical model based on Fermi surface anisotropy and non-local corrections to the London model.

6 Structural stability of the FLL

The structural order of the FLL can be deduced from the reciprocal space widths of the Bragg peaks, as described in section 3.2. In this chapter I report on measurements of the FLL longitudinal correlation length. In the non-magnetic borocarbides YNi_2B_2C and $LuNi_2B_2C$, this is found to be very long, exceeding 100 flux line latice spacings. Furthermore a maximum in the correlation length is observed at $H/H_{c2} \sim 0.2$. This behaviour is in contrast to the theoretical predictions of a monotonically increasing correlation length up to the regime of the peak effect. In contrast, the correlation length in $ErNi_2B_2C$ and $TmNi_2B_2C$ stays below 25 lattice spacings in the entire measured field range. A number of the results in this chapter are published in refs. [47, 48].

6.1 Experimental details

All measurements reported in the following were done with the applied field parallel to the crystalline c-axis, except if explicitly stated otherwise. All experiments were done following a field cooling. Background measurements were done after a zero field cooling.

Experimental resolution

The absolute values of the FLL Bragg peak widths are needed to determine the FLL correlation lengths. Therefore the experimental resolution has to be subtracted off the measured rocking curve widths. The experimental resolution is calculated as described in section 3.4.

Two different pinhole sizes were used in the collimation section: Ø 16 mm and Ø 25 mm. The cadmium masks, on which the samples were mounted, were of irregular shape fitted to the individual crystals. The average diameter of the cadmium masks lies in the range Ø $6.3-7.1$ mm. Using equation (70) the beam divergence is given by

$$\begin{aligned} \Delta(2\theta)_{\text{B.D.}} &= 2\sqrt{2\ln 2}\,\frac{\sqrt{(w_1/l)^2+(w_2/l)^2}}{4} \\ &= 0.10^{\text{o}} - 0.15^{\text{o}} \text{ FWHM.} \end{aligned}$$

In all experiments the velocity selector was set to a wavelength spread $\Delta\lambda_{\text{n}}/\lambda_{\text{n}} = 18\%$. The contribution to the experimental resolution from the neutron wavelength spread depends on both the chosen wavelength and on the magnitude of the scattering vector, i.e. on the applied magnetic field. When performing the experiment the wavelength is usually decreased as the field is increased, to maintain a roughly constant scattering angle and to increase the neutron flux. With the used settings $q\lambda_{\text{n}}$ lies in the range $0.03^{\text{o}} - 0.11^{\text{o}}$, and using equation (69) the contribution to the angular resolution from the wavelength spread is

$$\begin{aligned} \Delta(2\theta)_{\text{W.S.}} &= \frac{q\lambda_{\text{n}}}{4\pi}\sqrt{\frac{4\ln 2}{3}}\,\frac{\Delta\lambda_{\text{n}}}{\lambda_{\text{n}}} \\ &= 0.03^{\text{o}} - 0.09^{\text{o}} \text{ FWHM.} \end{aligned}$$

Combining the contributions from the beam divergence and from the wavelength spread, the total angular resolution is

$$\begin{aligned} \Delta(2\theta)_{\text{Res.}} &= \sqrt{\Delta(2\theta)^2_{\text{W.S.}} + \Delta(2\theta)^2_{\text{B.D.}}} \\ &= 0.10^{\text{o}} - 0.17^{\text{o}} \text{ FWHM.} \end{aligned}$$

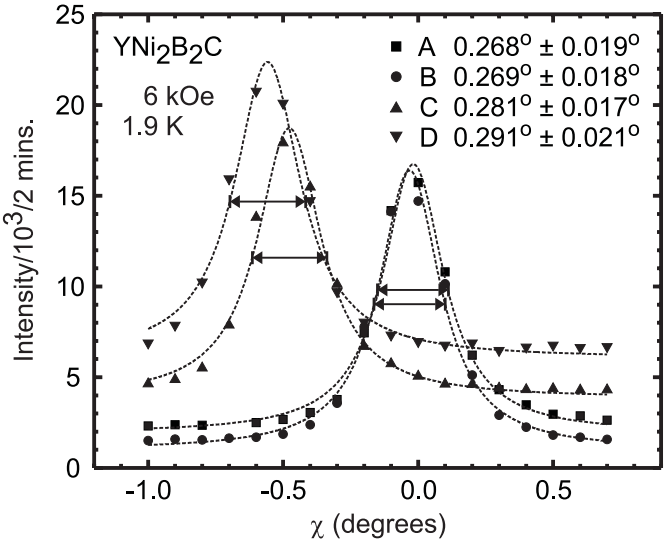

Figure 39. FLL rocking curve for YNi_2B_2C at $T = 1.9$ K and $H = 6$ kOe. The rotation is performed around the vertical axis. The data are fitted to Lorentzians with FWHM listed in the plot. The intensity of each Bragg peak, labeled A-D, is obtained by summing the counts in a small part of the detector centered at the peak positions, as shown in chapter 4, figure 18.

All the resolution subtractions are of course performed by calculating the resolution for the exact setting under which the individual measurements were performed.

6.2 Data analysis

The raw data consist of the FLL rocking curves. A typical example of such a rocking curve is shown in figure 39. To obtain the FLL longitudinal correlation length the data are fitted to Lorentzians, the calculated resolution is subtracted, and finally the Lorentz factor correction described in section 3.4 is applied:

$$\Delta\omega_{\mathrm{L}} = \frac{\sqrt{\Delta(2\theta)^2_{\mathrm{Rock}} - \Delta(2\theta)^2_{\mathrm{Res.}}}}{\eta_Q}. \tag{76}$$

After this analysis all the measured peaks are averaged to yield one value for $\Delta\omega$ for each field.

This analysis is an approximation as the measured width and the resolution are subtracted in quadrature, ignoring that the rocking curves are fitted to Lorentzians and the resolution functions are approximated by Gaussians. Figure 40 shows the measured rocking curve widths in $LuNi_2B_2C$, and the results of resolution subtraction.

The in-plane width of the FLL Bragg peaks stayed constant, and resolution limited for all fields above 2 kOe. Below 2 kOe an azimuthal broadening was observed, related to the hexagonal to square symmetry transition described in chapter 5.

6.3 Results

The width, $\Delta\omega_{\mathrm{L}}$, measures how correlated the flux lines are along their length, parallel to the applied field. From figure 40 one finds that the FLL in $LuNi_2B_2C$ orders in the longitudinal direction, signalled by a decrease in $\Delta\omega_{\mathrm{L}}$, as the field increases, up to a critical value of roughly 10 kOe. Above 10 kOe the rocking

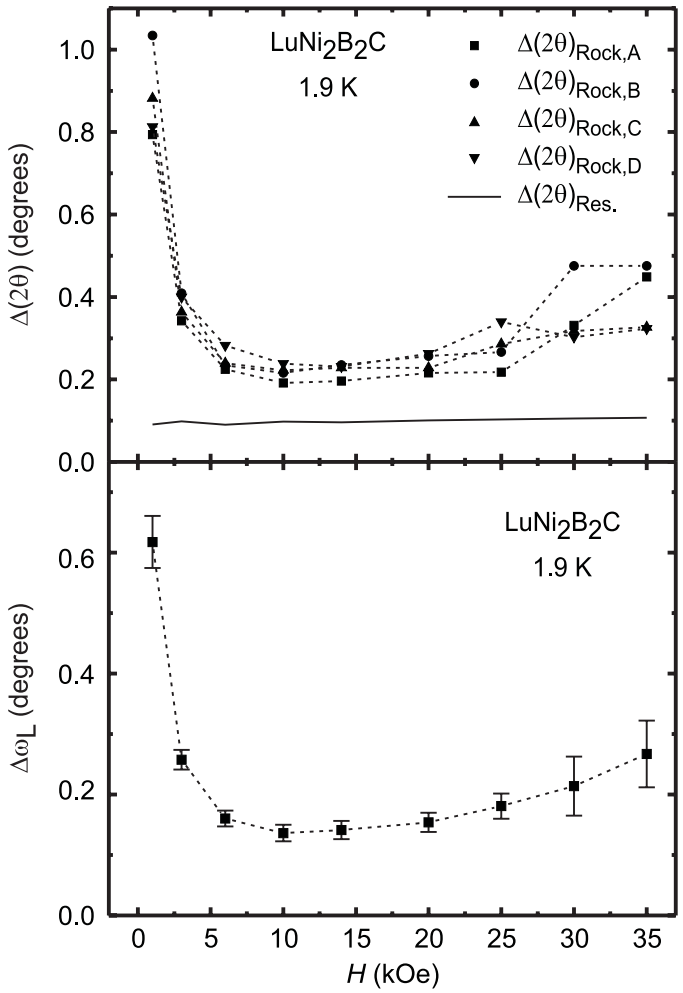

Figure 40. Measured FLL rocking curve widths and the intrinsic longitudinal FLL width versus field for $LuNi_2B_2C$ at $T = 1.9$ K. Top: FWHM of Lorentzians fitted to the measured rocking curves for the four (1,0) FLL Bragg reflections labelled A-D. The solid line is the calculated experimental resolution. Bottom: The intrinsic FLL widths obtained by averaging, and resolution- and Lorentz factor corrections.

curves gradually broadens. Measurements of the rocking curve width in YNi_2B_2C yields similar results shown in figure 41.

The longitudinal correlation length, $\xi_{\rm L}$ is defined from equation (65) by

$$\xi_{\rm L} = \frac{2}{\Delta q_{\rm L}}, \text{ with } \Delta q_{\rm L} = q\,\Delta\omega_{\rm L}.$$

This is normalized to the flux line spacing $a_0 = 2\pi/q$, yielding

$$\frac{\xi_{\rm L}}{a_0} = \frac{2q}{2\pi\,\Delta q_{\rm L}} = \frac{1}{\pi\,\Delta\omega_{\rm L}}. \tag{77}$$

The normalized longitudinal correlation length is thus given by the reciprocal of $\Delta\omega_{\rm L}$, shown in figure 42 for YNi_2B_2C and $LuNi_2B_2C$.

6.4 Discussion

The broad maximum in the longitudinal correlation length at $H/H_{\rm c2} \sim 0.2$ for YNi_2B_2C and $LuNi_2B_2C$ is a quite unexpected behaviour. In all previous studies of the FLL in $NbSe_2$ [37] and niobium [64], and within the collective pinning

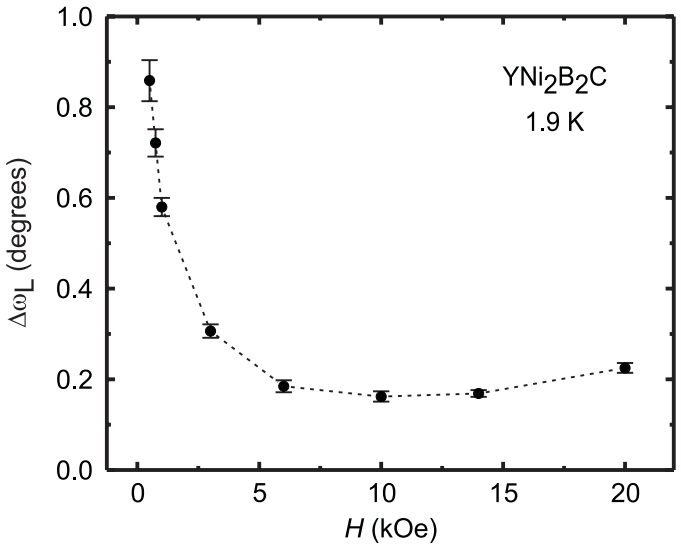

Figure 41. Intrinsic longitudinal FLL widths versus field for YNi_2B_2C at $T = 1.9$ K.

theory, the longitudinal correlation length increases monotonically with field, up to the onset of the peak effect.

It is important to stress that the maximum in ξ_L/a_0 is not in direct relation to either the hexagonal to square FLL symmetry transition reported in the previous chapter and which occur below 1 kOe, or to the peak effect at $H/H_{c2} \sim 0.9$ seen in the critical current and shown in figure 43 for $LuNi_2B_2C$.

Comparison to the Larkin-Ovchinnikov theory of collective pinning

The LO 3D collective pinning model was described in section 2.3. Within this model the longitudinal extension of a correlated volume is given by equations (26) and (29):

$$L_c = \frac{2c_{44}\, c_{66}\, \xi^2}{n\, f^2} = \sqrt{\frac{2c_{44}\, \xi}{J_c B}}.$$

It should be noted that this only depends on the FLL tilt modulus. However, as it was pointed out by Giamarchi and Le Doussal [65, 66] the correlation length, ξ_L, measured by SANS is in general not the same as L_c. The results of the LO model are obtained assuming flux line displacements of the order of the coherence length, ξ, to determine the magnitude of L_c. The SANS measurements, on the other hand, are sensitive to displacements of the order one flux line spacing, a_0. The simplest way of relating the two different quantities, is by adding the longitudinal extent of the correlated volumes as in a random walk, $\sqrt{a}\,\xi = a_0$, thereby finding

$$\xi_L \propto a\, L_c = A \left(\frac{a_0}{\xi}\right)^2 L_c,$$

with A being a constant.

Transport measurements

To explicitly demonstrate the discrepancy between our results and the LO theory, transport measurements were performed on $LuNi_2B_2C$ by B. P. Barber at Bell Laboratories, Lucent Technologies. For these measurements bars of dimensions $3 \times 1 \times 0.3$ mm^3 were cut from the large crystals, and etched in HF and aqua regia to reduce surface pinning. Results of critical current measurements, determined

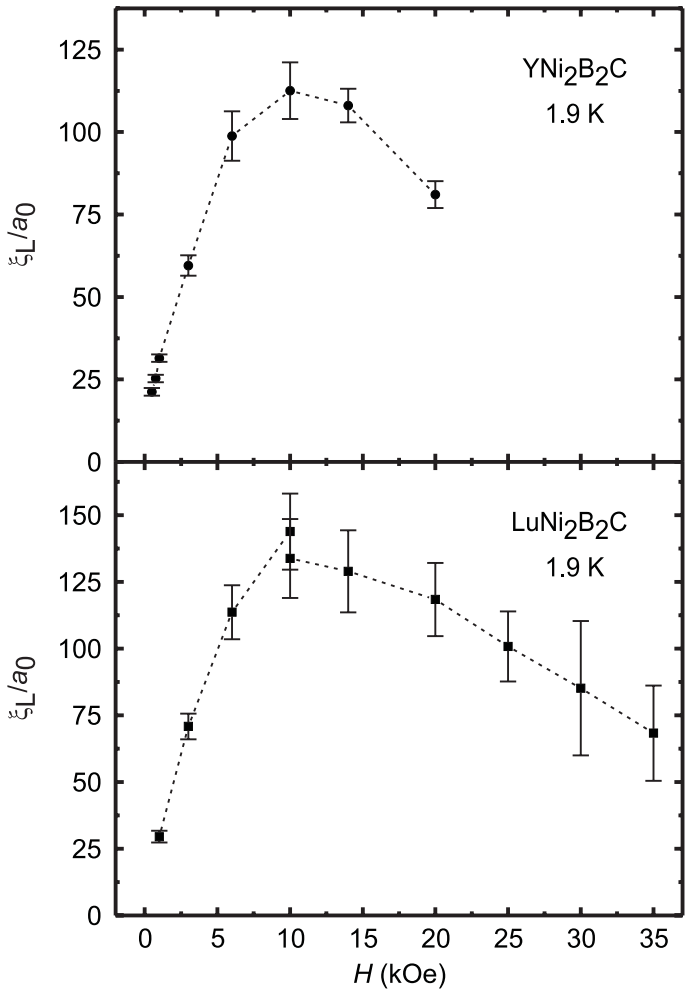

Figure 42. Longitudinal FLL correlation lengths versus field for YNi_2B_2C (top) and $LuNi_2B_2C$ (bottom) at $T = 1.9$ K. The correlation lengths are normalized to the flux line spacing.

by the onset of flux flow resistivity, are shown in figure 43. The figure shows the pinning force density J_cB together with L_c inferred by using the LO theory with $c_{44} = BH/4\pi$ and $\xi = 82$ Å. The value for ξ was determined in chapter 4. The expression for the tilt modulus differs from equation (31) since it ignores dispersion. This is justified since $\lambda/L_c \ll 1$. A large peak effect is observed near $H = 60$ kOe and a weak maximum at 10 kOe. The field dependence of L_c is seen to follow $B^{3/2}$, equivalent to a constant pinning force density, up to the onset of the peak effect. Clearly, the weak maximum in J_cB at 10 kOe does not have a signature in L_c, and even if it had, it would produce a local minimum, rather than the maximum observed in ξ_L. The finite critical current in $LuNi_2B_2C$ up to H_{c2} suggests that the high field reduction of the longitudinal correlation length is a static disordering, rather than a dynamic effect such as melting of the FLL.

A direct comparison for $LuNi_2B_2C$ between ξ_L measured by SANS, and L_c from transport is shown in figure 44. Both L_c and $A(a_0/\xi)^2 L_c$ are shown. Clearly the data agree within the framework of the collective pinning model for fields below 10 kOe, but sharply disagree for fields greater than this.

It is remarkable that ξ_L and L_c agree without any rescaling of the amplitudes. This is in contrast to the discussion above, of the difference between the two quantities. For $A(a_0/\xi)^2\, L_c$, the constant must be set to $A = 1/70$ to provide a decent fit to ξ_L. This is in disagreement with our expectations that A be close to

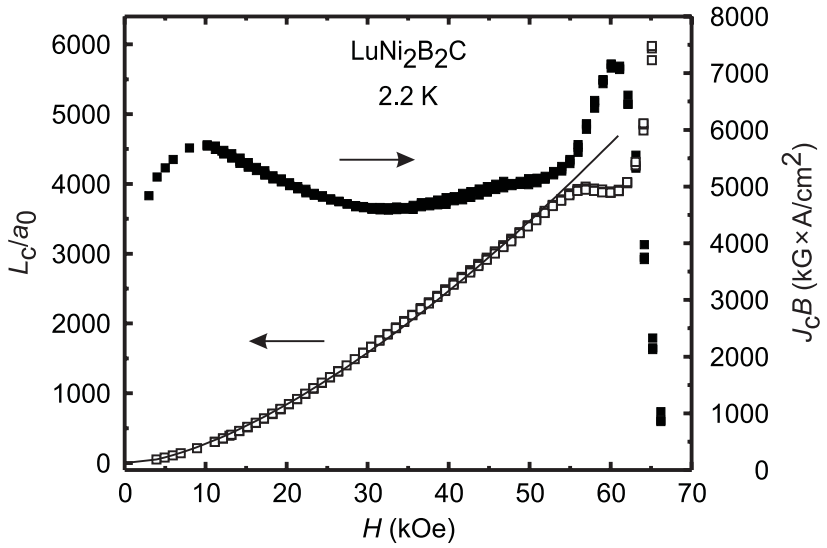

Figure 43. Transport measurements of the pinning force density, J_cB, and inferred FLL correlation lengths, L_c/a_0 for $LuNi_2B_2C$ at $T = 2.2$ K. The line is a fit to $B^{3/2}$, equivalent to a constant pinning force. The measurements were performed by B. P. Barber at Bell Laboratories, Lucent Technologies.

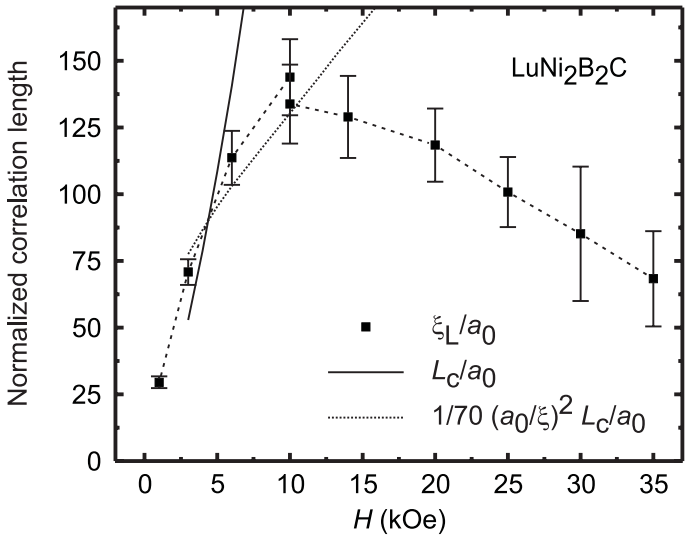

Figure 44. Comparison between the longitudinal correlation length determined from SANS measurements (ξ_L), and from transport (L_c). Both L_c and $A(a_0/\xi)^2 L_c$ with $A = 1/70$ are shown.

one. This descrepancy, however, does not alter the qualitative conclusion, that the LO theory fails to describe the FLL longitudinal correlation length above 10 kOe in YNi_2B_2C and $LuNi_2B_2C$.

A shear modulus driven correlation length?

A possible explanation of the breakdown of the collective pinning model is related to the shear properties of the FLL in the borocarbides. Anomalous shear properties at low fields are documented by the hexagonal to square symmetry transition, treated in the previous chapter. The speculation that ξ_{L} is driven by the shear properties is further justified by the observation that the shear modulus, c_{66}, given in equation (31) has a peak at $H/H_{\mathrm{c2}} = 0.3$, and provides an excellent fit to the correlation length as shown in figure 45. The fitted value for H_{c2} is however found

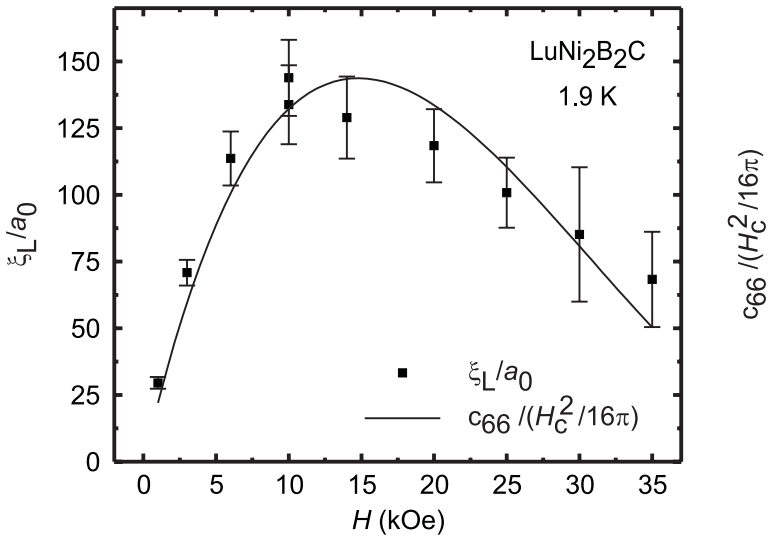

Figure 45. The shear modulus, c_{66}, fitted to ξ_L for $LuNi_2B_2C$. In the fit $H_{c2} = 49$ kOe.

to be 25% low. It should be noted that the expression for c_{66} was calculated for a hexagonal FLL. It has not been calculated for a square FLL.

There are two routes which may lead to the shear modulus controlling the behaviour of ξ_{L}. First, since the square FLL is stabilized by non-local correction to the London model cf. section 5.4, the statistical summations which lead to the cancellation of c_{66} in the expression for the longitudinal correlation length may need to be modified. Second, the assumption of an isotropic continuum elasticity may be too gross an oversimplification.

6.5 Supplementary results

In order to compare to the results for YNi_2B_2C and $LuNi_2B_2C$, measurements were performed on other borocarbides and for different field configurations.

Rotated field

Rotating the field in the *ac*-plane 30° away from the *c*-axis produces a distorted hexagonal FLL as described in chapter 5. However, the longitudinal correlation length in YNi_2B_2C for this field orientation, shows the same behaviour as with $\boldsymbol{H} \parallel \hat{\boldsymbol{c}}$. This is shown in figure 46. The only difference is that the low field ξ_{L} is reduced for the rotated field, compared to the situation with the field parallel to the *c*-axis. This indicates that high field static disorder is unrelated to the FLL symmetry, which again supports the use of c_{66} for a hexagonal FLL in the previous section.

Doping studies

Looking at $Y_{0.75}Lu_{0.25}Ni_2B_2C$ one again find the same qualitative field dependence as for pure YNi_2B_2C and $LuNi_2B_2C$. This is shown in figure 47. In this case the measured rocking curves were very close to the instrumental resolution, which explain the higher values of ξ_{L}/a_0 and the large error bars.

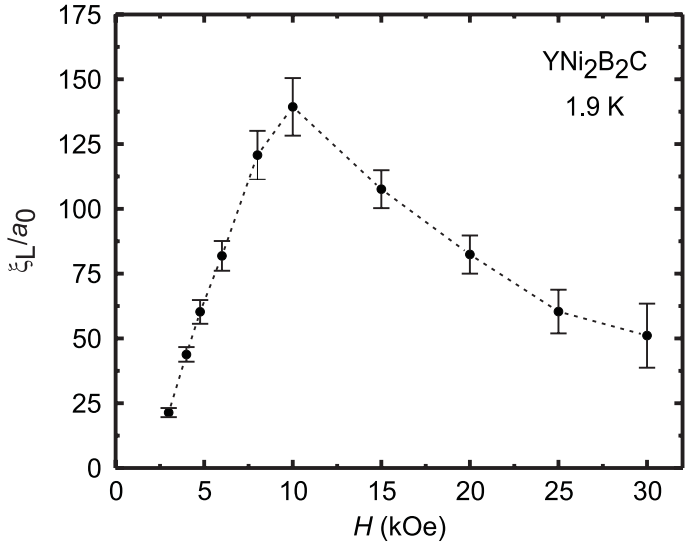

Figure 46. Longitudinal correlation length for YNi_2B_2C at $T = 1.9$ K, with the field rotated 30° away from c-axis. The field was rotated around the crystalline a-axis, keeping it in the ac-plane.

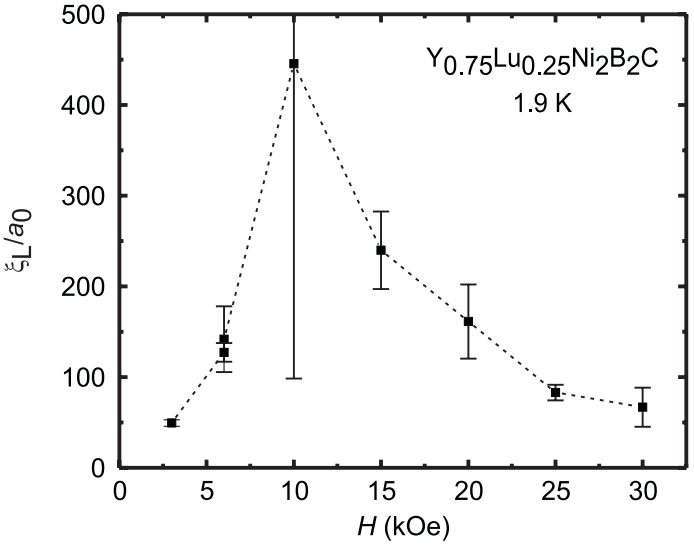

Figure 47. Longitudinal correlation length for $Y_{0.75}Lu_{0.25}Ni_2B_2C$ at $T = 1.9$ K.

$ErNi_2B_2C$ and $TmNi_2B_2C$

Turning to the magnetically ordered borocarbides $ErNi_2B_2C$ and $TmNi_2B_2C$, measurements reveal a disordered FLL compared to YNi_2B_2C and $LuNi_2B_2C$,with longitudinal correlation lengths that never exceeds 25 flux line spacings. Figure 48 and 49 shows ξ_L for $ErNi_2B_2C$ and $TmNi_2B_2C$. In $ErNi_2B_2C$ there is first an increase with field up to 3 kOe, after which ξ_L stays constant equal to $15a_0$. For $TmNi_2B_2C$, ξ_L is roughly constant equal to $10a_0$ in the measured field range above 2 kOe. In $ErNi_2B_2C$ it is believed that ξ_L is dominated by pinning to the magnetic domain walls, since the measurements were done in the magnetically ordered state, $T < T_N = 6.8$ K. The measurements on $TmNi_2B_2C$ were performed above the magnetic transition at $T_N = 1.5$ K. However it is possible that magnetic fluctuation exists above T_N affecting ξ_L. The interaction between the FLL and the magnetic structure in $TmNi_2B_2C$ is treated in detail in chapter 7.

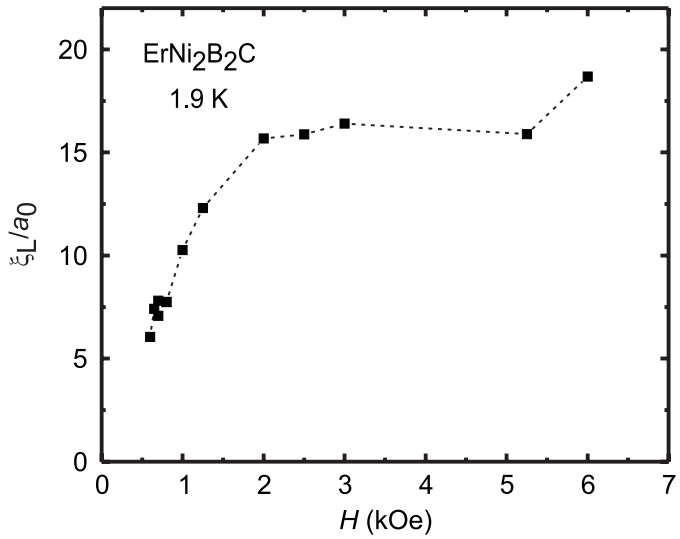

Figure 48. Longitudinal correlation length for $ErNi_2B_2C$ at $T = 1.9$ K.

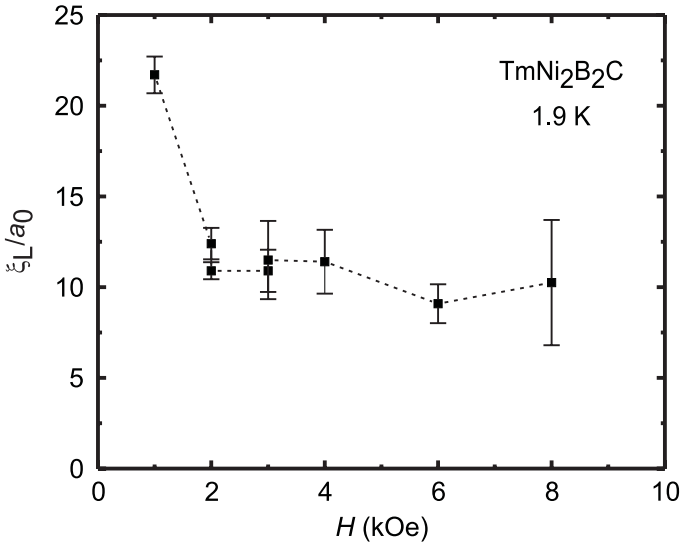

Figure 49. Longitudinal correlation length for $TmNi_2B_2C$ at $T = 1.9$ K.

6.6 Summary

In conclusion, a static disordering of the square FLL with an onset at $H/H_{c2} \sim 0.2$ was observed in YNi_2B_2C and $LuNi_2B_2C$. At this field the collective pinning model breaks down. The static disordering is also observed in the (distorted) hexagonal FLL in YNi_2B_2C with the field rotated away from the c-axis. An explanation is offered, which attributes the disorder to the anomalous shear properties of the FLL in the borocarbides.

7 Magnetism and the FLL in $TmNi_2B_2C$

A main motivation for studying the FLL in the borocarbides was the coexistence of magnetism and superconductivity, and the possibility of observing interactions between the two states. Previous studies of the FLL in $ErNi_2B_2C$ showed a distortion and rotation of the FLL below 2.3 K [19], and a weak suppression in λ and a peak in ξ when entering the magnetically ordered state at $T_N = 6.8$ K [62]. This chapter reports on studies of the FLL in $TmNi_2B_2C$, which shows a dramatic interaction between the FLL and the magnetic structure. The results in this chapter are published in refs. [48, 67].

Materials, which would exhibit both superconductivity and ferromagnetism, are caught in a dilemma, as these mutually exclusive phenomena both represent long wavelength order. For superconductivity to persist, the magnetic structure must assume an antiferromagnetic modulation, short enough to obtain a small net moment $< H_c$ on the lengthscale of the superconducting coherence length.

An overview of the phase diagram for the superconducting and magnetic states for $TmNi_2B_2C$ is shown in figure 50. The material is superconducting for temperatures below $T_c = 11$ K. For fields applied parallel to the c-axis, the upper critical field peaks near $T = 5$ K and $H_{c2} = 10$ kOe due to the Tm sublattice magnetization [16]. As the Tm moment saturates below 4 K, the normal state resistance drops 25% due to reduced spin scattering. Below $T_N = 1.5$ K there is a magnetic transition into an antiferromagnetically ordered state which coexists with the superconductivity [17, 68]. Initially this transition seems to have only a modest effect on the superconductivity, as H_{c2} shows only a gradual rise below T_N due to the tradeoff between the changes in the Tm susceptibility and the normal state mean free path. The zero field magnetic structure is a long period transverse, antiferromagnetic modulated spin density wave, schematically shown in figure 51. The Tm ordered moments are parallel to the c-axis and the propagation vector is $\boldsymbol{q}_{mI} = 0.094(\boldsymbol{a}^* + \boldsymbol{b}^*)$. The magnitude of the moments is believed to be "squared up" signaled by the large number of higher order reflections seen by neutron diffraction [17].

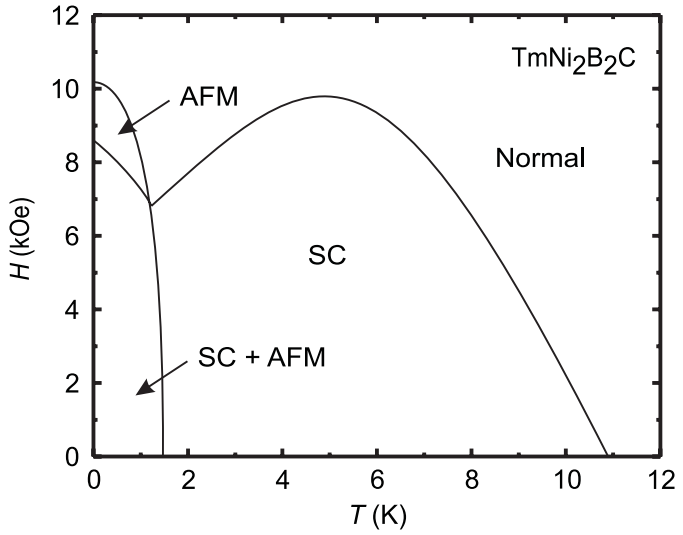

Figure 50. General phase diagram for $TmNi_2B_2C$ showing the magnetic (AFM) and superconducting (SC) states. The magnetic phase was determined from the SANS measurements and H_{c2} was determined by K. Harada and P. L. Gammel from a resistance onset criterion.

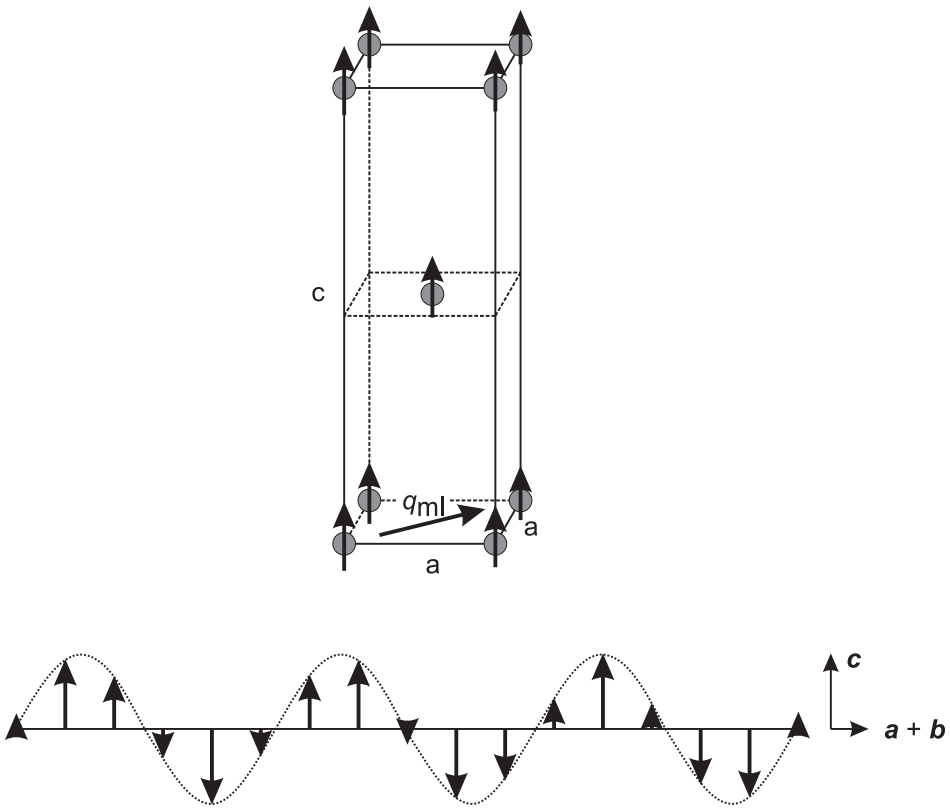

Figure 51. Schematic picture of the direction and modulation of the Tm moments in the $TmNi_2B_2C$ zero field magnetic structure. Top shows one unit cell and bottom shows the modulation of the moments along the magnetic ordering vector, $\boldsymbol{q}_{mI}$. The magnetic structure is a transverse spin density wave, with the Tm ordered moments parallel to the c-axis, and a period of $\sim$ 7.5 lattice spacings (26 Å) [17, 68].

7.1 Experimental details

All measurements reported in this chapter were done with the applied field parallel to the crystalline *c*-axis. All FLL measurements were done following a field cooling. Background measurements were done after a zero field cooling. The magnetic structure was studied using a variety of field and temperature histories, specified individually in the following.

Two configurations of the SANS spectrometer were used in this experiment. One setting which optimized the resolution at the shortest possible scattering vectors, was used for FLL studies. This was accomplished by going to high neutron wavelengths (5-11 Å), and moving the detector as far away as possible (6 m) from the sample. The other setting was the opposite extreme, covering as much of reciprocal space as possible. Here the neutron wavelength was reduced to 3 Å, and the detector was moved as close as possible (1.2 m) to the sample. This setting was used for studies of the magnetic structure.

7.2 Data analysis

The data analysis techniques used in this chapter are similar to the previous chapters. For both the magnetic and the FLL Bragg reflections the integrated intensity was determined as described in chapter 4.

The symmetry of the the FLL and the magnetic modulation, was determined from the azimuthal intensity distribution in the diffraction patterns. Figure 52 shows an example of a FLL diffraction pattern and the points on which the in-

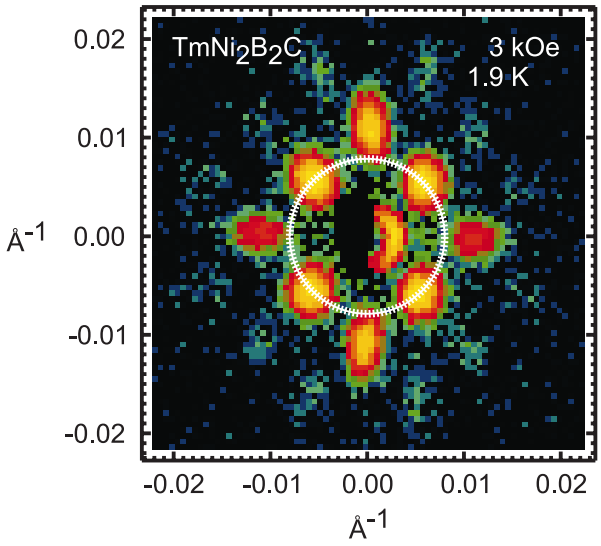

Figure 52. FLL diffraction pattern in $TmNi_2B_2C$ at $T = 1.9$ K and $H = 3$ kOe. The circle shows the sampling positions for the azimuthal intensity analysis.

tensity is sampled. The sample positions are equally spaced azimuthally, and are in general not coincident with one particular detector pixel position. Instead the intensity is found by linear interpolation from the four nearest neighbours. The density of points is adjusted to the detector resolution, and hence spaced by approximately one pixel size ~ 5 mm. Results from this analysis are shown in figure 61. As the diffraction patterns for both the magnetic structure as well as for the FLL always are four fold symmetric, the azimuthal intensity is folded into one quadrant.

Finally, an analysis of the rocking curve width, as described in chapter 6, was performed on a small part of the data.

7.3 Results

A precursor of the fascinating results to be discovered in $TmNi_2B_2C$ in the coexistence phase below 1.5 K, was found in the FLL rocking curve widths shown in figure 53. Below 6 K the rocking curves start to broaden for fields above 1 kOe. This occurs simultaneously with the suppression of H_{c2} driven by the magnetization of the Tm ions, showing a coupling between the magnetic properties and the FLL. The remainder of the chapter deals with the coexistence of superconductivity and magnetism below 1.5 K.

Magnetism

Applying a magnetic field above 2 kOe induces new magnetic reflections, in addition to the ones from the zero field magnetic structure. Figure 54 shows examples of magnetic diffraction patterns obtained above and below 2 kOe. The new modulation, which coexists with the low field state, is split $15^o \pm 0.5^o$ about the [100] direction with a magnitude $q_{\mathrm{mII}} = 0.21$ Å^{-1}, 22% below q_{mI}. The splitting is not the result of a simple magneto-elastic distortion, as the $\boldsymbol{q}_{\mathrm{mI}}$ peaks remain unsplit. Scattering studies of the magnetic order on the SANS beamline, probe only a small part of reciprocal space, precluding detailed determination of magnetic spin configurations. Preliminary data on field induced magnetic structure in $TmNi_2B_2C$ suggest that it arises from components of the Tm parallel to the c-axis, organized in two orthogonal domains.

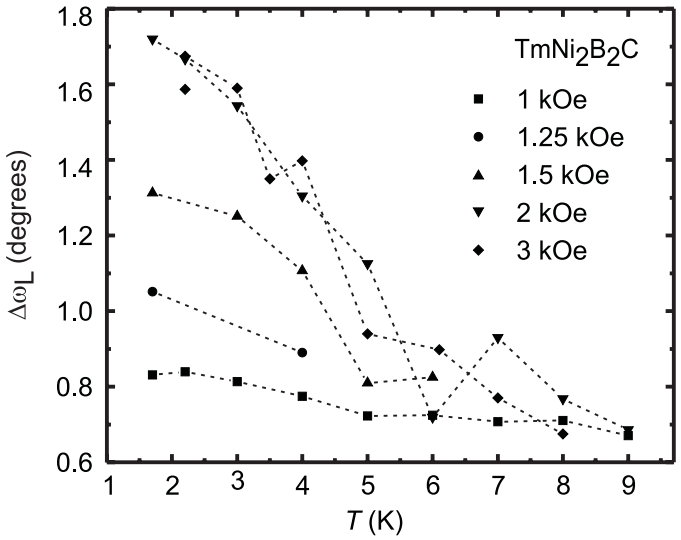

Figure 53. Intrinsic FLL rocking curve widths in $TmNi_2B_2C$ versus temperature. A marked increase below 6 K and for fields above 1 kOe is observed. Intermediate broadenings are seen in the interval from 1.25 kOe to 2 kOe.

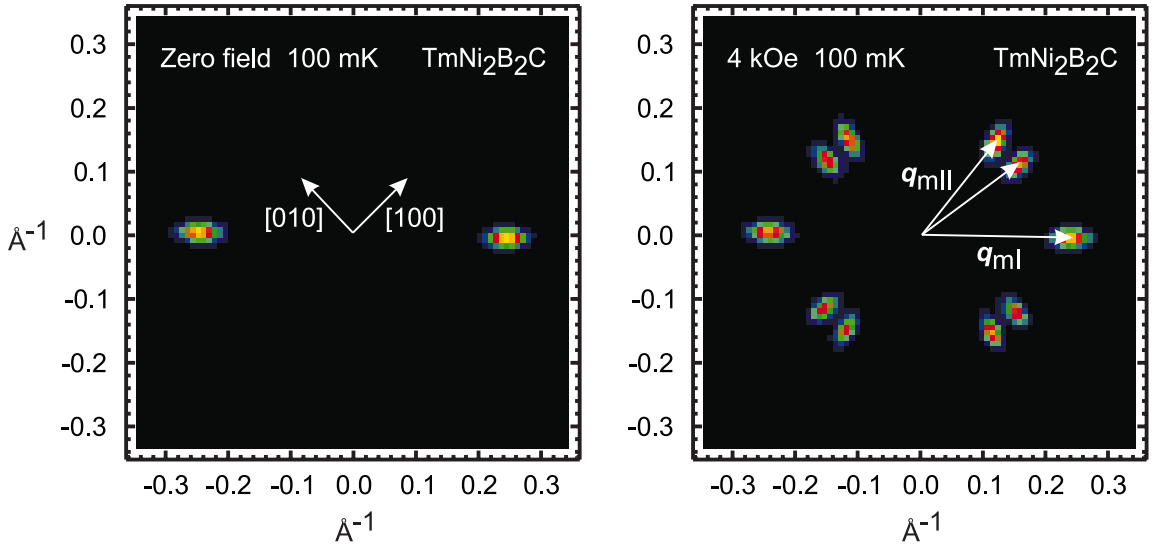

Figure 54. Diffraction pattern of the magnetic structure in $TmNi_2B_2C$. On the left this is shown following a zero field cooling, and on the right following a field cooling in $H = 4$ kOe. Both diffraction patterns were obtained at $T = 100$ mK. The orientation with respect to the host crystal is shown on the left, and the magnetic scattering vectors are shown on the right. The images are produced by summing a rocking curve around the vertical axis. This does not satisfy the Bragg condition for reflections lying on the vertical axis, thus explaining their absence. The radial smearing of the peaks are an artifact of the coarse energy resolution ($\Delta\lambda_n/\lambda_n = 18\%$).

Examples of the temperature and field dependence of the reflectivity of the magnetic peaks are shown in figure 55 and 56. The reflectivity is monotonically decreasing with temperature, with sharp transitions at 1.4 K for $\boldsymbol{q}_{\mathrm{mI}}$ and 1.3 K for $\boldsymbol{q}_{\mathrm{mII}}$. The field dependence is more complex. Between 2 kOe and 4 kOe the reflectivity of the $\boldsymbol{q}_{\mathrm{mII}}$ peaks grows rapidly, while the reflectivity of the $\boldsymbol{q}_{\mathrm{mI}}$ peaks drops correspondingly. Between 4 kOe and 10 kOe all magnetic reflections have roughly equal, and falling intensity. Finally, at $H \sim 10$ kOe and $T = 100$ mK,

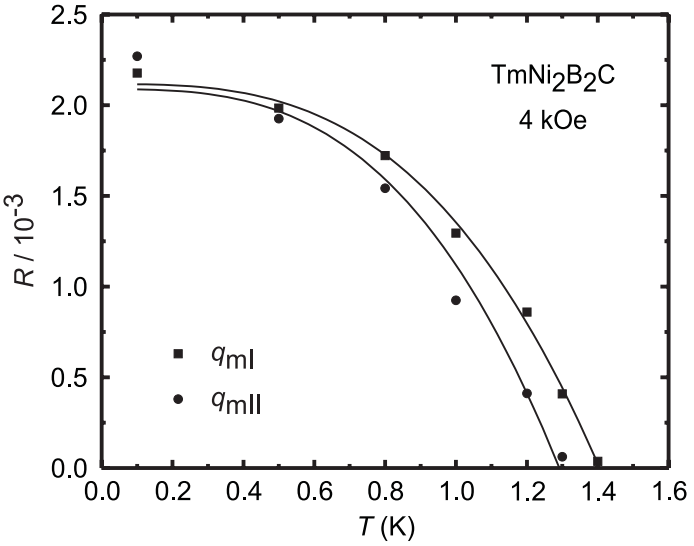

Figure 55. Intensity of magnetic reflections in $TmNi_2B_2C$ versus temperature at $H = 4$ kOe. Lines are a guide to the eye. Squares represent intensity of the zero field magnetic structure, and circles represent the field induced structure. The data are obtained following a field cooling.

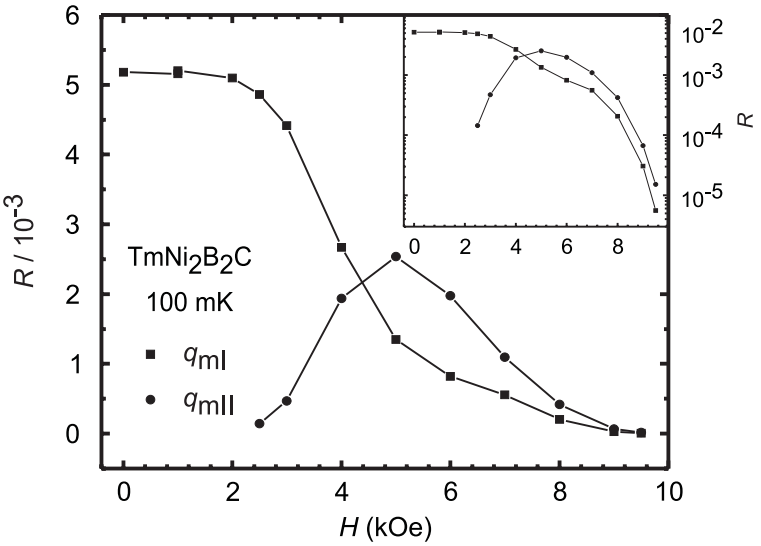

Figure 56. Intensity of magnetic reflections in $TmNi_2B_2C$ versus field at $T = 100$ mK. Squares represent intensity of the zero field magnetic structure, and circles represent the field induced structure. Inset shows data on a logarithmic scale. The data are obtained by changing the field at 100 mK.

there is a second magnetic transition, presumably into a saturated paramagnetic state as significant extra scattering near $q = 0$ is observed for fields above H_{c2}. Unlike the sharp disappearance of the magnetic reflections with temperature, the intensity of the magnetic scattering shows a very slow field dependence indicating critical scaling behavior.

The magnetic diffraction data are summarized by the phase diagram in figure 57. The zero field magnetic phase is identified as I. At 2 kOe, there is a sharp magnetic transition into a complex modulated structure identified as II.

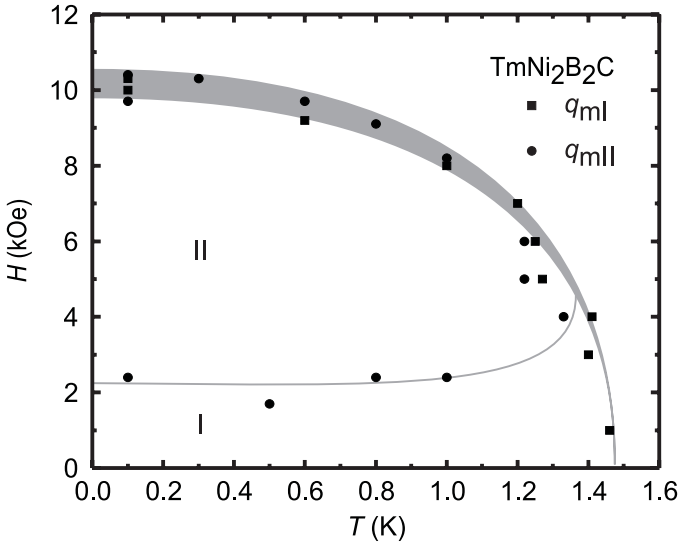

Figure 57. Magnetic phase diagram for $TmNi_2B_2C$. The squares show where the $\boldsymbol{q}_{mI}$ reflections vanish, and the circles show where the $\boldsymbol{q}_{mII}$ reflections vanish. The uncertainty on the upper critical field is due to the slow field dependence.

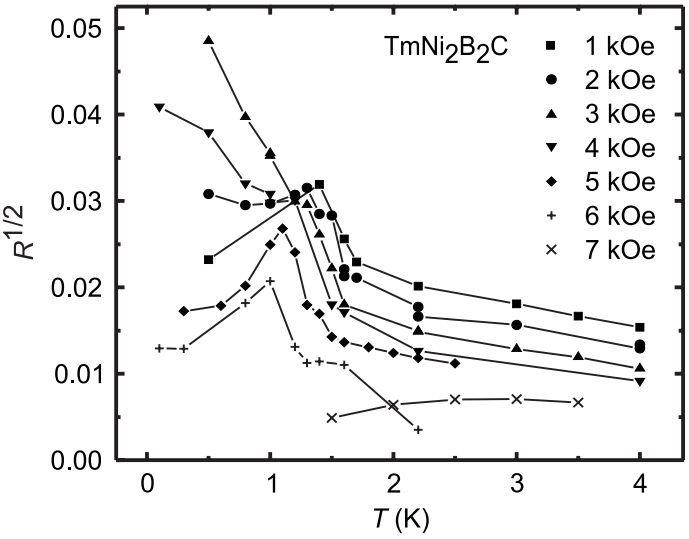

Figure 58. Square root of the FLL reflectivity versus temperature for $TmNi_2B_2C$, for fields between 1 and 7 kOe. The values are corrected for the multiplicity of the (1,0) FLL Bragg reflections, as the symmetry changes.

FLL reflectivity

The temperature dependence of the FLL reflectivity, R, is dominated by the penetration depth. Above T_N, $\sqrt{R}$ is linear in agreement with the Ginzburg-Landau theory, as described in chapter 4. Below T_N the reflectivity increases sharply as shown in figure 58. For all fields but 3 and 4 kOe the reflectivity falls off again inside the magnetic state. Plotting the reflectivity versus field, shown in figure 59, this leads to a peak upon crossing the nearly temperature independent transition between magnetic phases I and II. These results imply a decrease in λ at the magnetic transitions, and it is clearly no longer possible to use the simple Ginzburg-Landau expansions as they predict a monotonic decrease of the reflectivity with both field and temperature.

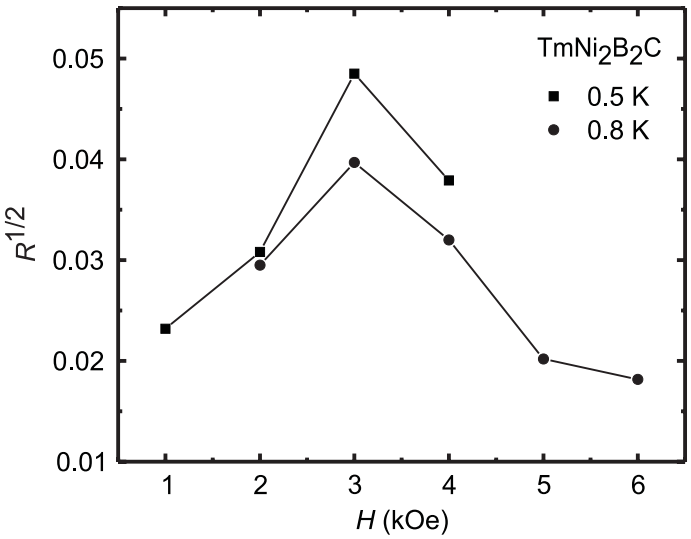

Figure 59. Square root of the FLL reflectivity versus field for $TmNi_2B_2C$ for two different temperatures below T_N.

FLL symmetry

Even more striking are the changes in the FLL symmetry in the vicinity of the magnetic transitions. Depending on field and temperature, three different FLL symmetries are observed. Examples of the diffraction patterns observed and their real space interpretations are shown in figure 60. Several orders of diffraction peaks are visible, suggesting well ordered FLL domains.

The square FLL oriented along [110] shown in the top panel of figure 60 is stable below 2 kOe for all temperatures. In the magnetically ordered state, coincident with the transition at 2 kOe, the FLL undergoes a rhombohdral distortion, as shown in the middle panel of figure 60. The two rhombohedral domains, rotated by 90°, are each distorted by $15^\circ \pm 1^\circ$ around [110]. This is best seen in the (2,0) Bragg peaks. The magnitude of the angular splitting is equal to that of the field induced magnetic peaks. The rhombic symmetry remains stable between 3 and 4 kOe, the split increasing with field. Above 4 kOe, the FLL undergoes a second transition into two hexagonal domains, also rotated by 90°, shown in the bottom panel of figure 60. This cannot be an extension of the rhombohedral distortion, as that would result in hexagonal domains oriented along [100], rather than the observed [110]. Instead, this change in orientation implies a discontinuous transition.

The progression of the FLL symmetry transitions are reflected in the azimuthal intensity distributions, shown in figure 61. Here both the square to rhombic and the rhombic to hexagonal symmetry transitions are clearly observed. In particular the discontinuous nature of the latter transition is evident.

The temperature and field range of the different FLL symmetries are summarized in the composite phase diagram in figure 62, which also contains the magnetic phases and H_{c2}. The FLL undergoes a two-step structural symmetry transition from a square FLL below 3 kOe to a hexagonal FLL above 5 kOe. First, the square FLL oriented by [110] undergoes a rhombohedral distortion along the [100] crystalline direction, followed by a discontinuous transition into a hexagonal symmetry oriented along [110].

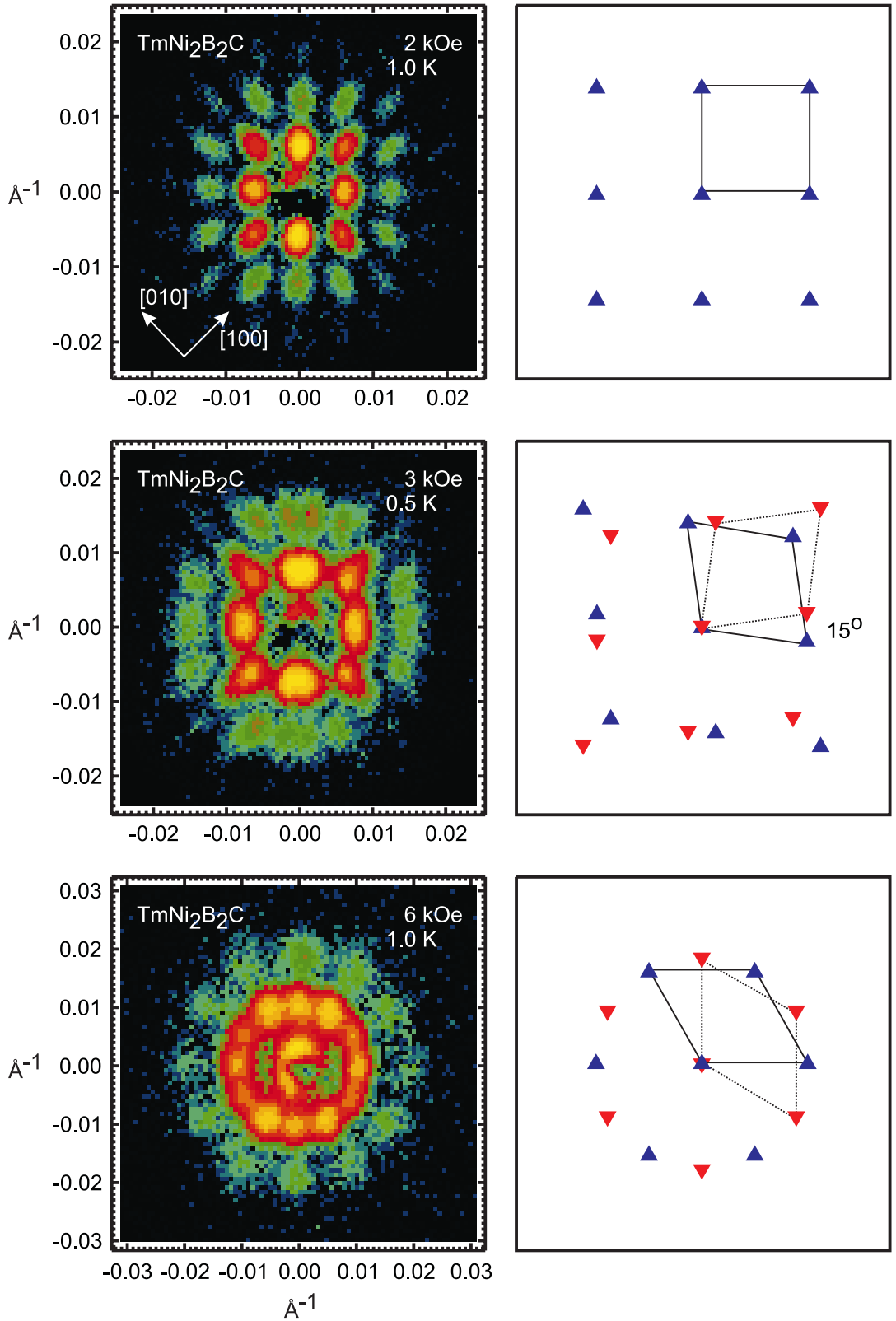

Figure 60. Examples of FLL diffraction patterns for $TmNi_2B_2C$ showing square (top), rhombic (middle) and hexagonal (bottom) symmetries. The right side shows real space interpretations. Where the FLL is composed of two equivalent domains, they are represented by up and down triangles. The crystal orientation is shown in the top panel and is identical for all fields. The diffraction patterns were obtained by summing an entire rocking curve.

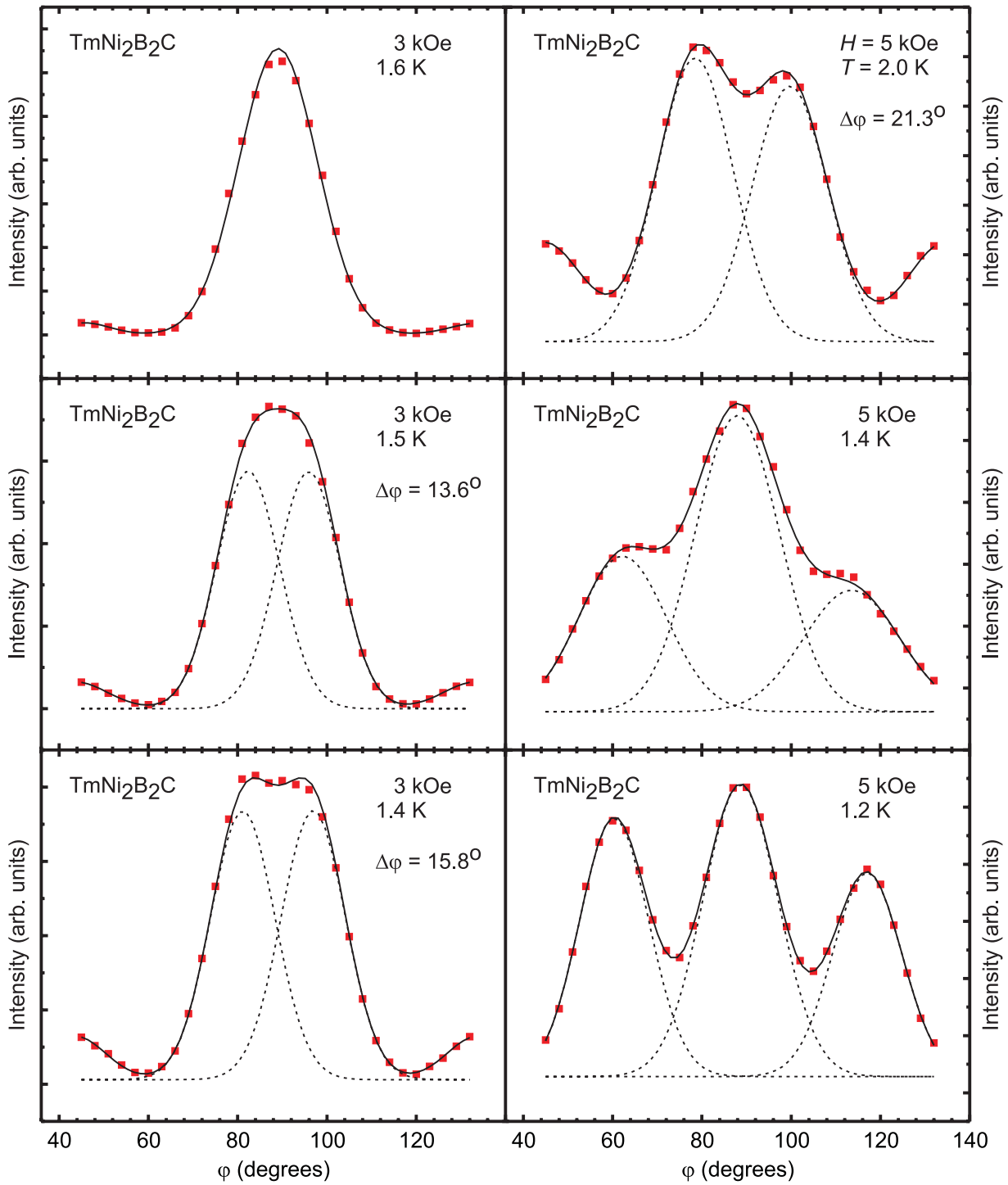

Figure 61. Examples of the FLL azimuthal intensity distributions in $TmNi_2B_2C$ for scattering vectors corresponding to the (1,0) Bragg reflections. Left column shows the square (top) to rhombic (bottom) transition induced by lowering the temperature at $H = 3$ kOe. Right column shows the discontinuous transtion from rhombic (top) to hexagonal (bottom) at $H = 5$ kOe.

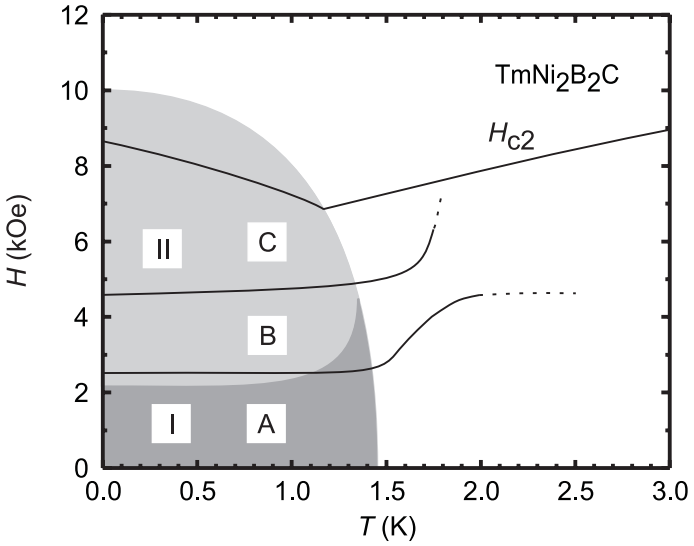

Figure 62. Composite phase diagram for $TmNi_2B_2C$ including bulk superconductivity, FLL symmetry and magnetic phases. The upper critical field H_{c2} is determined from transport. The magnetic phase diagram is from figure 57, and is shown by the shaded regions. The solid lines denote the boundaries between the different FLL symmetries, with dashed extensions where there is no experimental data. The different FLL symmetries are denoted by A (square), B (rhombohedral) and C (hexagonal).

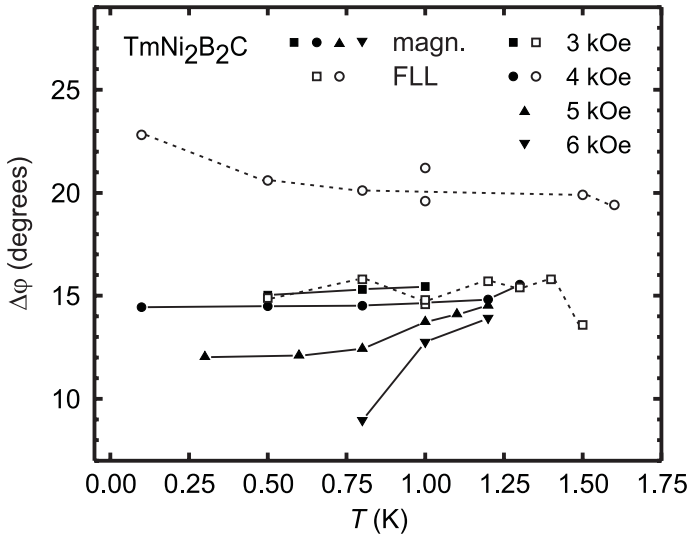

Figure 63. Comparison between magnetic and FLL split in $TmNi_2B_2C$ versus temperature for fields between 3 and 6 kOe.

Hysteresis in split of magnetic reflections

Following a field cooling process the $\boldsymbol{q}_{\mathrm{mII}}$ peaks are always split as described above. A comparison between the FLL and magnetic split is shown in figure 63. In the field range corresponding to a rhombic FLL (3 and 4 kOe), the magnetic split is roughly constant, independent of temperature and field. For fields above 4 kOe, corresponding to a hexagonal FLL, the magnetic split is reduced, and decreasing as the temperature is lowered.

The splitting of the magnetic peaks with wavevector $\boldsymbol{q}_{\mathrm{mII}}$ can be suppressed at high fields, by cooling the sample in the saturated paramagnetic state and then reducing the field into the hexagonal FLL state. This is shown in figure 64. Here the

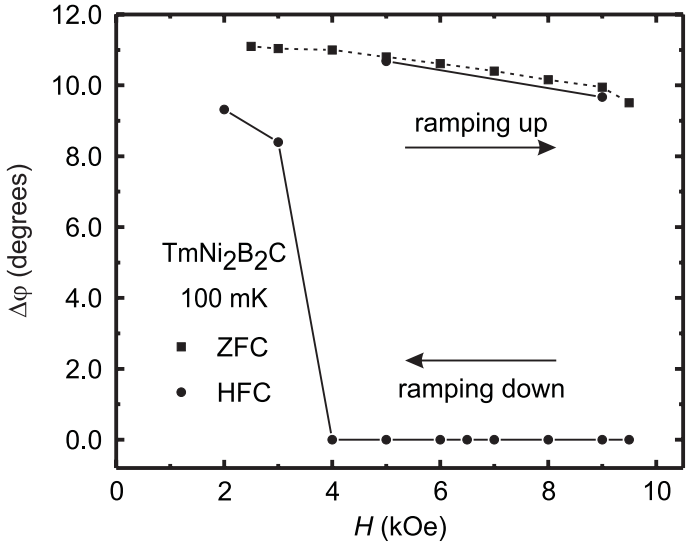

Figure 64. Hysteresis of magnetic split in $TmNi_2B_2C$. The magnetic split is shown for two different field histories: a zero field cooling (ZFC) and a high field cooling (HFC).

magnetic split is shown for two different field histories. Cooling in zero applied field followed by an increase, results in split $\boldsymbol{q}_{\mathrm{mII}}$ peaks in the entire magnetic phase II, allthough with a slightly smaller split ($\sim 11^{\mathrm{o}}$) than for a field cooling. Performing a high field cooling, followed by a reduction of the field, results in unsplit $\boldsymbol{q}_{\mathrm{mII}}$ peaks down to 4 kOe. Below this field the peaks split, and remain so when the field is again increased.

7.4 Discussion

It is interesting to consider the difference in the magnetic properties of $TmNi_2B_2C$ and the previously studied $ErNi_2B_2C$, to gain an understanding of what makes the former special. There are two features that distinguish $TmNi_2B_2C$ from the other magnetic borocarbides. One is the direction of the ordered moment, which in $TmNi_2B_2C$ is along the c-axis, instead of in the ab-plane. The second is the long wavelength modulation (26 Å) of the magnetic structure. Intuitively, it can be understood why both of these features will enhance the interaction between the magnetism and the FLL, since the Tm moments are parallel to the applied field, and the magnetic modulation approaches the superconducting coherence length.

The interaction between the magnetics and the FLL is reflected in virtually all the measured properties. First, the FLL reflectivity is always sharply peaked at the magnetic transitions. This implies either a most surprising increase in the density of superconducting electrons near the magnetic transitions, or, more likely, a reduction in the effective penetration depth due to susceptibility corrections $\lambda_{\mathrm{eff.}} = \lambda/(1+4\pi\chi)^{1/2}$ and hence $(R/R_{\chi=0})^{1/2} = (1+4\pi\chi)^2$ [69, 70]. Additional low temperature magnetization data are needed to verify this picture. Secondly, one notes the strong correlation between the FLL symmetry and the magnetic structure, especially near the 2 kOe transitions. Finally, the hysteresis in the split of the field induced magnetic reflections coincide with the square to rhombic FLL symmetry transition. Such low temperature hysteresis is common in magnetic systems. In $HoNi_2B_2C$, hysteresis in the metamagnetic transitions has been reported [71], and in $DyNi_2B_2C$ the associated residual moment has been seen to suppress superconductivity [72]. However, this hysteresis is not seen in the FLL. If the FLL is the determining factor in this problem, then the hysteresis in the split of the

magnetic peaks could be ascribed to passing through a FLL symmetry transition.

The origin of the FLL symmetry transitions in relation to magnetic transition is still an open question, since we cannot from the present data determine if one drives the other or *vice versa*. The fact that the rhombic and hexagonal FLL symmetries only exist in or close to the magnetically ordered phase indicates that the magnetism, in agreement with conventional wisdom, is the driving property. On the other hand, the hysteresis in the magnetic split appears to be driven by the FLL symmetry.

It is important to point out the difference between the symmetry transitions reported here, and the low field transition described in chapter 5. The latter occurs at much lower fields ($H < 1$ kOe) where the transition proceeds continuously through a rhombic distortion and is understood from anisotropic flux line interactions due to the high in-plane anisotropy of the Fermi surface.

7.5 Summary

Studies with an applied field parallel to the Tm moments, show that the structure of the magnetic modulation and the FLL symmetry are tightly coupled, resulting in a complex and fascinating phase diagram for the interplay between superconductivity and magnetism.

In the phase of coexisting superconductivity and magnetism, the FLL undergoes a two-step field driven symmetry transition, from square over rhombic to hexagonal. In all cases, the FLL is oriented by the [110] crystal lattice directions. The magnetic structure is also modified by an applied field.

Further studies into the details of the symmetries and the transitions between them are needed to identify the driving mechanisms, and to shed more light on the intimate connection between superconductivity and magnetism.

8 Summary and outlook

It is difficult to draw a final and unified conclusion from the results presented in this thesis. Except for the low field hexagonal to square FLL symmetry transition, no detailed understanding exists for the multitude of observed phenomena. The only thing one can safely conclude is that further studies of the FLL, and in particular of the interaction between magnetism and superconductivity, are needed.

Below, the essential results are summarized, and an outline of further experiments is presented.

8.1 Summary

The main results presented in this thesis are the following:

1. Existence of a low field hexagonal to square symmetry transition of the FLL, ubiquitous to the superconducting borocarbides, magnetic and non-magnetic alike. The square FLL is aligned by the [110] crystallographic direction, and the hexagonal FLL is aligned by [100]. The transition proceeds through an area preserving rhombohedral distortion of the FLL along [100]. The symmetry transition is due to a four-fold anisotropy of the Fermi surface in the borocarbides. The superconducting screening currents around each flux line are distorted away from the circular flow pattern of an isotropic system, and towards a square. The square flow patterns manifest themselves by inducing a transition to a square FLL as the field is increased, when the screening currents around a flux line extends so far into the field distribution of the neighbours that the "squarishness" is significant on the range of the non-local electrodynamics. It is possible to shift the transition to higher fields by either rotating the applied field direction away from the c-axis, or by reducing the electronic mean free path by doping, thereby moving towards the dirty limit and suppressing non-local effects.

2. A static disordering of the FLL in YNi_2B_2C and $LuNi_2B_2C$. In these materials one finds a well-ordered FLL, with a longitudinal correlation length exceeding 100 flux line spacings. As the applied field is increased, the longitudinal correlation length, or equivalent the "straightness" of the flux lines, increases with field up to $H/H_{c2} \sim 0.2$. Above this field the FLL correlation length slowly starts to decrease, in contradiction with the theoretical model, which predicts a monotonic increase up to the onset of the peak effect. The origin of the crossover to a less ordered FLL is not resolved, but it is speculated that this behaviour is driven by the shear properties of the FLL. The longitudinal correlation length in $ErNi_2B_2C$ and $TmNi_2B_2C$ is much shorter, of the order 10 lattice constants. The reduction of the correlation length in these materials is believed to be due to interactions with the rare earth magnetic moments.

3. The existence of complex interactions between the magnetic state and the FLL in $TmNi_2B_2C$. The magnetic properties of $TmNi_2B_2C$ differ from those of the other magnetic borocarbides in two ways. The ordered moment is parallel to the c-axis, which also is the direction of the applied field, and the periodicity of the magnetic structure is long, becoming comparable to the superconducting coherence length. The FLL undergoes two symmetry transitions in addition to the low field hexagonal to square transition present in all the borocarbides. As the applied field is raised the square FLL first undergoes a rhombic distortion along [100] and then a discontinuous transition into a hexagonal symmetry aligned by [110]. The FLL symmetry transitions

are closely linked to changes in the magnetic structure. In zero field the magnetic structure is a transverse modulated spin density wave. As the field is increased the magnetic structure is modified, signalled by the appearence of additional peaks in the neutron scattering diffraction patterns. In addition, the FLL reflectivity shows distinct peaks as the thulium ions orders magnetically at T_N and across the field driven magnetic transition. Furthermore, the field induced magnetic structure is dependent on the field- and temperature history in the superconducting phase, giving rise to hysteresis. No explanation for this behaviour exists at the present.

8.2 Further outlook

It has been symptomatic of the experiments conducted on the FLL in the borocarbides so far, that they posed more questions than they answered. Even with respect to the low field symmetry transition, which is the most extensively studied, and believed to be well understood, unresolved questions remain.

Listed below are a number of experiments which are an direct extension of those reported in this thesis.

- Futher studies of the low-field hexagonal to square symmetry transition. The doping studies reported in chapter 5 must be completed and the data thoroughly analyzed. The possibility of a high field hexagonal FLL close to T_N, due to the vanishing of the H_{c2} anisotropy, should be investigated.
- The studies of the FLL symmetries and the magnetism in $TmNi_2B_2C$ have to be completed. The phase diagram for the FLL symmetries is still incomplete, and the details of the field-induced magnetic structure are unknown. Furthermore the nature of the interaction between the FLL and the magnetism is unresolved, since we cannot tell whether the FLL symmetry transition drives the magnetic properties or *vice versa*. Studies of doped samples that will change the superconducting properties while leaving the magnetism unchanged are scheduled to shed more light on this.
- The low-temperature behaviour of the FLL in $ErNi_2B_2C$ has not been studied. There is some speculation that a ferromagnetically modulated state might develop in $ErNi_2B_2C$ at low temperatures, which could give rise to a spontaneous FLL [73, 74]. This is a controversial idea, and has to be further investigated. In that respect, the ideal experimental configuration would be with the field perpendicular to the c-axis. However, due to the low neutron penetration of $ErNi_2B_2C$ and the fact that samples always grow as platelets with the c-axis being the thin dimension, this may not be feasible. The prospects of using isotopically enriched ^{168}Er to reduce neutron absorption are being investigated.
- The "missing" borocarbides. No FLL was ever observed in $HoNi_2B_2C$ despite numerous attempts. The FLL in $DyNi_2B_2C$ was never studied due to the large thermal neutron cross section of Dy. However, it should be possible using either very thin samples ($\sim$ 0.25 mm) or samples grown using isotopically enriched ^{162}Dy and ^{163}Dy.

Acknowledgements

A number of people and organizations deserve acknowledgements for their support during my period as a graduate student.

Above all I want to thank my wife, Katrine, for supporting my choice of career, and especially for tolerating my absence, physically as well as mentally, during experiments and numerous trips around the world. Also my daughter, Alberte, deserves thanks. Unbeknownst to herself, she has put a whole new perspective into my life, which I found especially helpfull during long and sometimes tedious experiments.

I would like to thank Risø National Laboratory and the Danish Research Academy (Forskerakademiet) for providing me with a scholarship, and also Lucent Technologies, Bell Laboratories for their hospitality at numerous visits, and economic support at a number of occasions. Part of the work in this thesis was supported by NATO under grant CRG960550. I would also like to thank the organizers of the 1996 HERCULES course in Grenoble for supporting my participation.

Finally, a number of persons at Risø, Bell Laboratories and several other places deserve thanks for their support and guideance. It is Niels Hessel Andersen, Kell Mortensen, Uri Yaron, Bradley P. Barber, Ken Harada, Peter L. Gammel, David J. Bishop, Paul C. Canfield and all the other people with whom I co-authored. In particular I would like to thank Niels for accomodating all my needs for resources and for taking the night shifts, Peter for support and guideance, acting much as my mentor, during the last three and a half years, and Dave for the occational pep-talk whenever one was needed. Special thanks also goes to Paul Canfield who supplied the beautiful crystals, and who is the only truely indispensible person in the collaboration.

References

[1] G. W. Crabtree, F. Behroozi, S. A. Campbell & D. G. Hinks. Anisotropic Superconducting and Magnetic Properties of a Single Crystal of $ErRh_4B_4$. *Phys. Rev. Lett.* **49**, 1342–1345 (1982).

[2] M. B. Maple & Ø. Fisher. *Superconductivity in Ternary Compounds II; Superconductivity and Magnetism*, chapter 4. Springer Verlag (1982).

[3] R. Nagarajan, Chandan Mazumdar, Zakir Hossain, S. K. Dhar, K. V. Gopalakrishnan, L. C. Gupta, C. Godart, B. D. Padalia & R. Vijayaraghavan. Bulk Superconductivity at an Elevated Temperature ($T_c \approx 12$ K) in a Nickel Containing Alloy System Y-Ni-B-C. *Phys. Rev. Lett.* **72**, 274–277 (1994).

[4] R. J. Cava, H. Takagi, H. W. Zandbergen, J. J. Krajewski, W. F. Peck, Jr., T. Siegrist, B. Batlogg, R. B. van Dover, R. J. Felder, K. Mizuhashi, J. O. Lee, H. Eisaki & S. Uchida. Superconductivity in the quaternary intermetallic compounds $LnNi_2B_2C$. *Nature* **367**, 252–252 (1994).

[5] T. Siegrist, H. W. Zandbergen, R. J. Cava, J. J. Krajewski & W. F. Peck, Jr. The crystal structure of superconducting $LiNi_2B_2C$ and the related phase LuNiBC. *Nature* **367**, 254–256 (1994).

[6] M. Xu, P. C. Canfield, J. E. Ostenson, D. K. Finnemore, B. K. Cho, Z. R. Wang & D. C. Johnston. Superconducting state magnetization and critical fields of single-crystal YNi_2B_2C. *Physica C* **227**, 321–326 (1994).

[7] H. Takagi, R. J. Cava, H. Eisaki, J. O. Lee, K. Mizuhashi, B. Batlogg, S. Uchida, J. J. Krajewski & W. F. Peck, Jr. Superconducting properties of the new boride-carbide superconductors. *Physica C* **228**, 389–392 (1994).

[8] C. V. Tomy, G. Balakrishnan & D. McK. Paul. Observation of superconductivity at 6 K in $DyNi_2B_2C$. *Physica C* **248**, 349–352 (1995).

[9] B. K. Cho, P. C. Canfield & D. C. Johnston. Onset of superconductivity in the antiferromagnetically ordered state of single-crystal $DyNi_2B_2C$. *Phys. Rev. B* **52**, R3844–R3847 (1995).

[10] C. V. Tomy, M. R. Lees, L. Afalfiz, G. Balakrishnan & D. McK. Paul. Superconductivity and magnetism in $DyNi_2B_2C$ single crystals. *Phys. Rev. B* **52**, 9186–9189 (1995).

[11] J. W. Lynn, S. Skanthakumar, Q. Huang, S. K. Sinha, Z. Hossain, L. C. Gupta, R. Nagarajan & C. Godart. Magnetic order and crystal structure in the superconducting RNi_2B_2C materials. *Phys. Rev. B* **55**, 6584–6598 (1997).

[12] A. I. Goldman, C. Stassis, P. C. Canfield, J. Zarestky, P. Dervenagas, B. K. Cho, D. C. Johnston & B. Sternlieb. Magnetic pair breaking in $HoNi_2B_2C$. *Phys. Rev. B* **50**, 9668–9671 (1994).

[13] J. Zarestky, C. Stassis, A. I. Goldman, P. C. Canfield, P. Dervenagas, B. K. Cho & D. C. Johnston. Magnetic structure of $ErNi_2B_2C$. *Phys. Rev. B* **51**, 678–680 (1995).

[14] S. K. Sinha, J. W. Lynn, T. E. Grigeriet, Z. Hossain, L. C. Gupta, R. Nagarajan & C. Godart. Neutron-diffraction study of antiferromagnetic order in the magnetic superconductor $ErNi_2B_2C$. *Phys. Rev. B* **51**, 681–684 (1995).

[15] B. K. Cho, P. C. Canfield, L. L. Miller, D. C. Johnston, W. P. Beyermann & A. Yatskar. Magnetism and superconductivity in single-crystal $ErNi_2B_2C$. *Phys. Rev. B* **52**, 3684–3695 (1995).

[16] B. K. Cho, Ming Xu, P. C. Canfield, L. L. Miller & D. C. Johnston. Magnetic and superconducting properties of single-crystal $TmNi_2B_2C$. *Phys. Rev. B* **52**, 3676–3683 (1995).

[17] B. Sternlieb, C. Stassis, A. I. Goldman, P. Canfield & S. Shapiro. Single crystal neutron diffraction study of the magnetic structure of $TmNi_2B_2C$. *J. Appl. Phys.* **81**, 4937–4939 (1997).

[18] D. Cribier, B. Jacrot, L. Madhav Rao & B. Farnoux. Mise en evidence par diffraction de neutrons d'une structure periodique du champ magnetique dans le niobium supraconducteur. *Phys. Lett.* **9**, 106–107 (1964).

[19] U. Yaron, P. L. Gammel, A. P. Ramirez, D. A. Huse, D. J. Bishop, A. I. Goldman, C. Stassis, P. C. Canfield, K. Mortensen & M. R. Eskildsen. Microscopic coexistence of magnetism and superconductivity in $ErNi_2B_2C$. *Nature* **382**, 236–238 (1996).

[20] V. L. Ginzburg & L. D. Landau. *Zh. Eksperim. i. Teor. Fiz.* **20**, 1064 (1950).

[21] J. Bardeen, L. N. Cooper & J. R. Schrieffer. Theory of Superconductivity. *Phys. Rev.* **108**, 1175–1204 (1957).

[22] E. M. Lifshitz & L. P. Pitaevskii. *Statistical Physics, Part 2 (Course of Theoretical Physics, Vol. 9)*. Pergamon Press (1980).

[23] Michael Tinkham. *Introduction to Superconductivity*. McGraw-Hill, second edition (1996).

[24] A. A. Abrikosov. On the Magnetic Properties of Superconductors of the Second Kind. *Sov. Phys. JETP* **5**, 1174–1182 (1957).

[25] B. Keimer, F. Doğan, I. A. Aksay, R. W. Erwin, J. W. Lynn & M. Sarikaya. Inclined-Field Structure, Morphology, and Pinning of the Vortex Lattice in Microtwinned $YBa_2Cu_3O_7$. *Science* **262**, 83–86 (1993).

[26] D. McK. Paul, C. V. Tomy, C. M. Aegerter, R. Cubitt, S. H. Lloyd, E. M. Forgan, S. L. Lee & M. Yethiraj. Nonlocal Effects and Vortex Lattice Transitions in YNi_2B_2C. *Phys. Rev. Lett.* **80**, 1517–1520 (1998).

[27] M. R. Eskildsen, P. L. Gammel, B. P. Barber, A. P. Ramirez, D. J. Bishop, N. H. Andersen, K. Mortensen & P. C. Canfield. Square to hexagonal symmetry transition of the flux line lattice in YNi_2B_2C for different field orientations. *Physica B* **241-243**, 811–813 (1998).

[28] R. P. Huebner. *Magnetic Flux Structures in Superconductors*. Springer-Verlag (1979).

[29] G. Blatter, M. V. Feigel'man, V. B. Geshkenbein, A. I. Larkin & V. M. Vinokur. Vortices in high-temperature superconductors. *Rev. Mod. Phys.* **66**, 1125–1388 (1994).

[30] Ernst Helmut Brandt. The flux-line lattice in superonductors. *Rep. Prog. Phys.* **58**, 1465–1594 (1995).

[31] D. J. Bishop, P. L. Gammel, L. F. Schneemeyer & J. V. Waszczak. Flux lattice melting in $YBa_2Cu_3O_7$. *Bull. Am. Phys. Soc.* **33**, 606 (1988).

[32] P. L. Gammel, L. F. Schneemeyer, J. V. Waszczak & D. J. Bishop. Evidence from Mechanical Measurements for Flux-Lattice Melting in Single-Crystal $YBa_2Cu_3O_7$ and $Bi_{2.2}Sr_2Ca_{0.8}Cu_2O_8$. *Phys. Rev. Lett.* **61**, 1666–1669 (1988).

[33] Mi-Ock Mun, Sung-Ik Lee, W. C. Lee, P. C. Canfield, B. K. Cho & D. C. Johnston. Vortex Glass and Lattice Melting Transition in a YNi_2B_2C Single Crystal. *Phys. Rev. Lett.* **76**, 2790–2793 (1996).

[34] S. Oxx, D. P. Choudhury, B. A. Willemsen, H. Srikanth, S. Sridhar, B. K. Cho & P. C. Canfield. Vortex response and critical fields observed via RF penetration depth measurements on the superconductor YNi_2B_2C. *Physica C* **264**, 103–108 (1996).

[35] S. Sridhar, S. Oxx, B. A. Willemsen, H. Srikanth & D. P. Choudhury. Comment on "Vortex Glass and Lattice Melting Transitions in a YNi_2B_2C Single Crystal". *Phys. Rev. Lett.* **77**, 2145 (1996).

[36] A. I. Larkin & Yu. N. Ovchinnikov. Pinning in Type II Superconductors. *J. Low Temp. Phys.* **34**, 409–428 (1979).

[37] U. Yaron, P. L. Gammel, D. A. Huse, R. N. Kleiman, C. S. Oglesby, E. Bucher, B. Batlogg, D. J. Bishop, K. Mortensen, K. N. Clausen, C. A. Bolle & F. De La Cruz. Neutron Diffraction Studies of Flowing and Pinned Magnetic Flux Lattices in $2H$-$NbSe_2$. *Phys. Rev. Lett.* **73**, 2748–2751 (1994); *ibid.* **74**, 1700 (1994).

[38] E. H. Brandt. Elastic and plastic properties of the flux-line lattice in type-II superconductors. *Phys. Rev. B* **34**, 6514–6517 (1986).

[39] G. E. Bacon. *Neutron Diffraction.* Oxford University Press, third edition (1975).

[40] K.-U. Neumann, F. Kusmartsev, H.-J. Lauter, O. Schärpf, T. J. Smith & K. R. A. Ziebeck. Experimental observation of lattice distortions due to a flux line lattice in niobium. *Eur. Phys. J. B* **1**, 5–9 (1998).

[41] A. Yaouanc, P. Dalmas de Réotier & E. H. Brandt. Effect of the vortex core on the magnetic field in hard superconductors. *Phys. Rev. B* **55**, 11107–11110 (1997).

[42] R. N. Kleiman, C. Broholm, G. Aeplli, E. Bucher, N. Stücheli, D. J. Bishop, K. N. Clausen, K. Mortensen, J. S. Pedersen & B. Howard. Neutron Diffraction from the Vortex Lattice in the Heavy-Fermion Superconductor UPt_3. *Phys. Rev. Lett.* **69**, 3120–3123 (1992).

[43] P. L. Gammel, D. A. Huse, R. N. Kleiman, B. Batlogg, C. S. Oglesby, E. Bucher, D. J. Bishop, T. E. Mason & K. Mortensen. Small Angle Neutron Scattering Study of the Magnetic Flux-Line Lattice in Single Crystal $2H$-$NbSe_2$. *Phys. Rev. Lett.* **72**, 278–281 (1994).

[44] John R. Clem. Simple Model for the Vortex Core in a Type II Superconductor. *J. Low Temp. Phys.* **18**, 427–434 (1975).

[45] Varley F. Sears. Neutron scattering lengths and cross sections. *Neutron News* **3**, 26–37 (1992).

[46] Pernille Harris. *Neutron and X-ray Diffraction from Modulated Structures.* Ph. D. thesis, University of Copenhagen, Denmark (1994).

[47] M. R. Eskildsen, P. L. Gammel, B. P. Barber, A. P. Ramirez, D. J. Bishop, N. H. Andersen, K. Mortensen, C. A. Bolle, C. M. Lieber & P. C. Canfield. Structural Stability of the Square Flux Line Lattice in YNi_2B_2C and $LuNi_2B_2C$ Studied with Small Angle Neutron Scattering. *Phys. Rev. Lett.* **79**, 487–490 (1997).

[48] M. R. Eskildsen, K. Harada, P. L. Gammel, A. B. Abrahamsen, N. H. Andersen, G. Ernst, A. P. Ramirez, K. Mortensen, D. G. Naugle, K. D. D. Rathnayaka, D. J. Bishop & P. C. Canfield. Intertwined symmetry of the magnetic modulation and the flux-line lattice in the superconducting state of $TmNi_2B_2C$. *Nature* **293**, 242–245 (1998).

[49] B. Mühlschlegel. Die thermodynamischen Funktionen des Supraleiters. *Zeitschrift für Physik* **155**, 313–327 (1959).

[50] M. R. Eskildsen, P. L. Gammel, B. P. Barber, U. Yaron, A. P. Ramirez, D. A. Huse, D. J. Bishop, C. A. Bolle, C. M. Lieber, S. Oxx, S. Sridhar, N. H. Andersen, K. Mortensen & P. C. Canfield. Observation of a Field-Driven Structural Phase Transition in the Flux Line Lattice in $ErNi_2B_2C$. *Phys. Rev. Lett.* **78**, 1968–1971 (1997).

[51] P. L. Gammel, D. J. Bishop, M. R. Eskildsen, K. Mortensen, N. H. Andersen, I. R. Fisher, K. O. Cheon, P. C. Canfield & V. G. Kogan. SANS studies of the Role of Non-Locality on the Flux Line Lattice Square-Hexagonal Symmetry Transition in $Lu(Ni_{1-x}Co_x)_2B_2C$. *Preprint* (1998).

[52] J. Schelten, G. Lippmann & H. Ullmaier. Neutron Diffraction Studies of the Morphology of Flux Line Crystals in Type II Superconductors. *J. Low Temp. Phys.* **14**, 213–227 (1974).

[53] D. K. Christen, H. R. Kerchner, S. T. Sekula & P. Thorel. Equilibrium properties of the fluxoid lattice in single-crystal niobium. II. Small-angle neutron-diffraction meausrements. *Phys. Rev. B* **21**, 102–117 (1980).

[54] U. Yaron, P. L. Gammel, G. S. Boebibger, G. Aeppli, P. Schiffer, E. Bucher, D. J. Bishop, C. Broholm & K. Mortensen. Small Angle Neutron Scattering Studies of the Vortex Lattice in the UPt_3 Mixed State: Direct Structural Evidence for the $B \rightarrow C$ Transition. *Phys. Rev. Lett.* **78**, 3185–3188 (1997).

[55] P. L. Gammel, D. J. Bishop, G. J. Dolan, J. R. Kwo, C. A. Murray, L. F. Schneemeyer & J. V. Waszczak. Observation of Hexagonally Correlated Flux Quanta In $YBa_2Cu_3O_7$. *Phys. Rev. Lett.* **59**, 2592–2595 (1987).

[56] V. G. Kogan, M. Bullock, B. Harmon, P. Miranović, Lj. Dobrosavljević-Grujić, P. L. Gammel & D. J. Bishop. Vortex lattice transitions in borocarbides. *Phys. Rev. B* **55**, R8693–R8696 (1997).

[57] V. G. Kogan, A. Gurevich, J. H. Cho, D. C. Johnston, Ming Xu, J. R. Thompson & A. Martynovich. Nonlocal electrodynamics and low-temperature magnetization of clean high-κ superconductors. *Phys. Rev. B* **54**, 12386–123996 (1996).

[58] A. B. Abrahamsen, M. R. Eskildsen, N. H. Andersen, J. Bilde-Sørensen, P. L. Gammel, D. J. Bishop & P. C. Canfield. Evidence for a Low Field Reorientation of the Flux Line Lattice in the Borocarbide Superconductor $TmNi_2B_2C$. *Preprint* (1998).

[59] Y. De Wilde, M. Iavarone, U. Welp, V. Metlushko, A. E. Koshelev, I. Aranson, G. W. Crabtree & P. C. Canfield. Scanning Tunneling Microscopy Observation of a Square Abrikosov Lattice in $LuNi_2B_2C$. *Phys. Rev. Lett.* **78**, 4273–4276 (1997).

[60] Kyungwha Park & David A. Huse. The Phase Transition to a Square Vortex Lattice in Type-II Superconductors with Fourfold Anisotropy. *Preprint* (1998).

[61] V. Metlushko, U. Welp, A. Koshelev, I. Aronson, G. W. Crabtree & P. C. Canfield. Anisotropic Upper Critical Field of $LuNi_2B_2C$. *Phys. Rev. Lett.* **79**, 1738–1741 (1997).

[62] P. L. Gammel, B. P. Barber, A. P. Ramirez, C. M. Varma, D. J. Bishop, P. C. Canfield, V. G. Kogan, M. R. Eskildsen, N. H. Andersen, K. Mortensen & K. Harada. Effects of Magnetic Order on the Critical Fields in the Superconducting State of $ErNi_2B_2C$. *Preprint* (1998).

[63] K. O. Cheon, I. R. Fisher, V. G. Kogan & P. C. Canfield. Resistivity and Magnetic Susceptibility of Single Crystal $Lu(Ni_{1-x}Co_x)_2B_2C$ ($x = 0.0 - 0.9$). *Phys. Rev. B* **58**, 6463–6467 (1998).

[64] P. L. Gammel, U. Yaron, A. P. Ramirez, D. J. Bishop, A. M. Chang, R. Ruel, L. N. Pfeiffer, E. Bucher, G. D'Anna, D. A. Huse, K. Mortensen & M. R. Eskildsen. Structure and Correlations of the Flux Line Lattice in Crystalline Nb through the Peak Effect. *Phys. Rev. Lett.* **80**, 833–836 (1998).

[65] T. Giamarchi & P. Le Doussal. Translational Order and Neutron Diffraction Studies of Magnetic Flux Line Lattices. *Phys. Rev. Lett.* **75**, 3372 (1995).

[66] U. Yaron, P. L. Gammel, D. A. Huse, R. N. Kleimann, C. S. Oglesby, E. Bucher, B. Batlogg, D. J. Bishop, K. Mortensen, K. N. Clausen, C. A. Bolle & F. De La Cruz. Reply to: Translational Order and Neutron Diffraction Studies of Magnetic Flux Line Lattices. *Phys. Rev. Lett.* **75**, 3373 (1995).

[67] M. R. Eskildsen, K. Harada, P. L. Gammel, N. H. Andersen, G. Ernst, A. P. Ramirez, D. J. Bishop, K. Mortensen & P. C. Canfield. Hysteresis in the field-induced magnetic structure in $TmNi_2B_2C$. *Preprint* (1998).

[68] J. W. Lynn, S. Skanthakumar, Q. Huang, S. K. Sinha, Z. Hossain, L. C. Gupta, R. Nagarajan & C. Godart. Magnetic order and crystal structure in the superconducting RNi_2B_2C materials. *Phys. Rev. B* **55**, 6584–6598 (1996).

[69] K. E. Gray. Ginzburg-Landau equations, interphase surface energy, and the intermediate state of superconductors with a paramagnetic normal state. *Phys. Rev. B* **27**, 4157–4160 (1983).

[70] M. Tachiki, H. Matsumoto & H. Umezawa. Mixed state in magnetic superconductors. *Phys. Rev. B* **20**, 1915–1927 (1979).

[71] P. C. Canfield, S. L. Bud'ko, B. K. Cho, A. Lacerda, D. Farrell, E. Johnston-Halperin, V. A. Kalatsky & V. L. Pokrovsky. Angular dependence of metamagnetic transitions in $HoNi_2B_2C$. *Phys. Rev. B* **55**, 970–976 (1997).

[72] Z. Q. Peng, K. Krug & K. Winzer. Large hysteresis effect and reentrant behaviour in $DyNi_2B_2C$ at temperatures $T < 2$K. *Phys. Rev. B* **57**, R8123–R8126 (1998).

[73] P. C. Canfield, S. L. Bud'ko & B. K. Cho. Possible co-existence of superconductivity and weak ferromagnetism in $ErNi_2B_2C$. *Physica C* **262**, 249–254 (1996).

[74] T. K. Ng & C. M. Varma. Spontaneous vortex phase discovered? *Phys. Rev. Lett.* **78**, 330–333 (1996).

Bibliographic Data Sheet **Risø–R–1084(EN)**

Title and author(s)

Small Angle Neutron Scattering Studies of the Flux Line Lattices in the Borocarbide Superconductors

Morten Ring Eskildsen

ISBN	ISSN
87–550–2472–6; 87–550–2473–4(internet)	0106–2840

Dept. or group	Date
Condensed Matter Physics and Chemistry Department	December 1998

Groups own reg. number(s)	Project/contract No.

Pages	Tables	Illustrations	References
83	4	64	74

Abstract (Max. 2000 char.)

This thesis describes small angle neutron scattering studies of the flux line lattice (FLL) in the following members of the borocarbide superconductors: YNi_2B_2C, $ErNi_2B_2C$, $TmNi_2B_2C$, $LuNi_2B_2C$, $Y_{0.75}Lu_{0.25}Ni_2B_2C$ and $Lu(Ni_{1-x}Co_x)_2B_2C$ with $x = 1.5 - 9\%$. Of these materials $ErNi_2B_2C$ and $TmNi_2B_2C$ exhibits coexisting superconductivity and magnetic ordering. Three main conclusions can be derived from the results in this thesis.

Existence of a low field hexagonal to square symmetry transition of the FLL, ubiquitous to the superconducting borocarbides, magnetic and non-magnetic alike. This symmetry transition is due to the four-fold anisotropy of the Fermi surface, distorting the screening currents towards a square flow pattern. This four-fold anisotropy together with non-local electrodynamics induces a transition to a square FLL, as the field is increased. Changing the non-locality range shifts the square to hexagonal transition onset field.

A static disordering of the FLL in YNi_2B_2C and $LuNi_2B_2C$. In these materials one observes a well ordered FLL, with a longitudinal correlation length exceeding 100 flux line spacings. As the applied field is increased the longitudinal correlation length, increases with field up to $H/H_{c2} \sim 0.2$. Above this field the FLL correlation length slowly starts to fall off, in contradiction to theoretical models.

The existence of complex interactions between the magnetic state and the FLL in $TmNi_2B_2C$. This is signalled by coinciding changes in the FLL symmetry and in the magnetic structure. The FLL show a two-step symmetry transition from square to rhombic and then hexagonal with increased field. In addition, the FLL reflectivity shows distinct peaks as the thulium ions orders magnetically at T_N and across the field driven magnetic transition. No explanation for this behaviour exists at the present.

Descriptors INIS/EDB

Boron carbides; magnetic flux; magnetic properties; neutron diffraction; rare earth compounds; small angle scattering; type II superconductors; vortices.

Available on request from:
Information Service Department, Risø National Laboratory
(Afdelingen for Informationsservice, Forskningscenter Risø)
P.O. Box 49, DK–4000 Roskilde, Denmark
Phone (+45) 46 77 46 77, ext. 4004/4005 · Fax (+45) 46 77 40 13